UNIVERSITA' DEGLI STUDI DI PADOVA

DIPARTIMENTO DI INGEGNERIA INDUSTRIALE
CORSO DI LAUREA IN INGEGNERIA DELL'ENERGIA ELETTRICA

Master Thesis

Application of a new Power Equivalent model in induction hardening of steel AISI-4340

SUPERVISOR: Prof. Ing Michele Forzan

CO-EXAMINERS: Prof. Ing Philippe Bocher (Montréal, ÈTS)
Prof. Ing Frédéric Sirois (Polytechnique Montéal)

GRADUATE: Federico Bellotto

Academic year 2016-2017

In nova fert animus mutates dicere formas
Corpora. Di, coeptis, nam vos mutatis et illas,
Adspirate meis,primaque ab origine mundi
Ad mea perpetuum deducite tempora carmen.
Ovidio, Metamorfosi, Libro I

*"*Science cannot solve the ultimate mystery of nature. And that is because, in the last analysis, we ourselves are part of nature and therefore part of the mystery that we are trying to solve.*"* – *Max Planck, Where is Science going?* (1932)

Contents

List of Figures

List of Tables

Abstract

Nowadays the surface induction hardening process is becoming even more widespread. As a matter of fact, not only it is more environmentally friendly, but also it is very interesting because of its fast time manufacturing and possibility to have a precise control of the full process.
The accurate prediction and control of the depth of the induced phase transformation is the most remarkable step in the whole treatment.

To keep in consideration the non−linear material properties and the coupling between electric and thermal physics the FEM (finite element method) is the more used tool. The best accuracy possible is reached using time transient simulations; although, with magnetic fields in the 10^4-10^5[Hz] range, the difference in time scales between the thermal and electromagnetic problems is very large.
In order to restrain the computational time cost, especially in industrial application, it is required the use of both transient thermal and harmonic domain electromagnetic simulations.

However, linear or even nonlinear frequency simulations cannot represent such complex material behaviour (e.g. the non−linear B−H curve in steel), because frequency truncation occurs over the harmonic spectrum. Any distortion in the excitation signal or magnetic response of the material will therefore be poorly approximated if operating near the saturation point of the steel workpiece. Hence, one must find a strategy to extract the relevant information from the B−H curve, which is valid solely in the time domain, and transform it into some value of permeability for a given amplitude of the magnetic field in the harmonic domain.

The aim of this thesis is to find a complex non−liner magnetic permeability that gives back, in the harmonic domain, the same distribution of the lost power generated in the time domain simulation when it is applied a periodic excitation.
Firstly, it is validated a new approach called "Power Equivalent model" (PE model). The distribution of the losses is measured in one electromagnetic when it has reached the steady state. Then, it will be compared with the losses obtained from the harmonic domain simulations. To do that some basilar geometries will be used. Finally, the temperature distributions in the steel sample, after an induction heating process, will be compared.
This new Power Equivalent model is able, not only to have a very low computational time cost that allows to study more complex geometries but also, to maintain a good accuracy in the results.
Besides, this approach has a great potential that can be used in several applications because it can deal with hysteresis losses thanks to the fact it finds a complex magnetic permeability. Moreover, there are many empirical ways to build such an equivalent model to run simulations, but all of them lack physical justification.

Chapter 1

Induction Hardening

In this chapter, we are going to introduce the theoretical background necessary to understand the hardening process through induction heating.
Hardening is the particular process that makes a material, in the specific case steel, harder. The hardness of a metal is directly proportional to the uniaxial yield stress at the location of the imposed strain. A harder metal will have a higher resistance to plastic deformation than a less one and that is why they are so required for many applications.
The practice developed and improved over the centuries, combined with the increase of the physical laws that explain the process, allowed to get more and more accurate and controlled hardening processes.
Nowadays in induction heating there is a conductive copper coil that is fed by an alternative current which frequency depends on the established thickness of the hardening process. The variation of the magnetic field, generates eddy currents inside the steel pieces that has to be hardened.
The nature of induction heat treatment is a combination of two phenomena, which are tightly interrelated because physical properties depend strongly on both magnetic field intensity and temperature.
The most important principles behind induction hardening are:

- Induction laws from Maxwell's laws and how Focault's current develops inside the workpiece;
- Joule's effect that explains the heat source;
- Phenomena of conduction and thermal convection

Moreover, today's heat treatments should consider the non-constant behaviour of the thermal and electromagnetic properties of the workpiece such as specific heat, thermal conductivity, Curie's transition temperature, magnetic permeability and electric resistivity during the heating cycle (these properties will be discussed in the chapter 3).

1.1 Fe-C Diagram and Hardening Technique

To fully understand of the hardening process is important the get the characteristics of steels, in particular the martensitic transformation.
Steels are alloy of iron [Fe] and Carbon[C] (typically less than two percent of the weight) and other elements in smaller percentage (e.g. Manganese,Chromium, Nickel). In metallurgy metals define certain materials that have some physical properties strictly correlated with the aggregation of atoms. The solid state of a metal

is characterized by crystalline structures, in which it is possible to find particular and repeatable geometries that represent the elementary cells. In steel alloys, the crystal lattice can assume different geometries and symmetries: this phenomenon is called Polymorphism and the various structures are defined *allotropics*. Iron has two main structures, that play a key-role in many thermal treatments, that are stable in some range of temperatures:

- α-iron, body-centered cubic (BCC), stable still 911°C.
- γ-iron, face-centered cubic (FCC), stable still 1392°C.
- δ-iron, body-centered cubic (BCC), stable still 1536°C(fusion point).

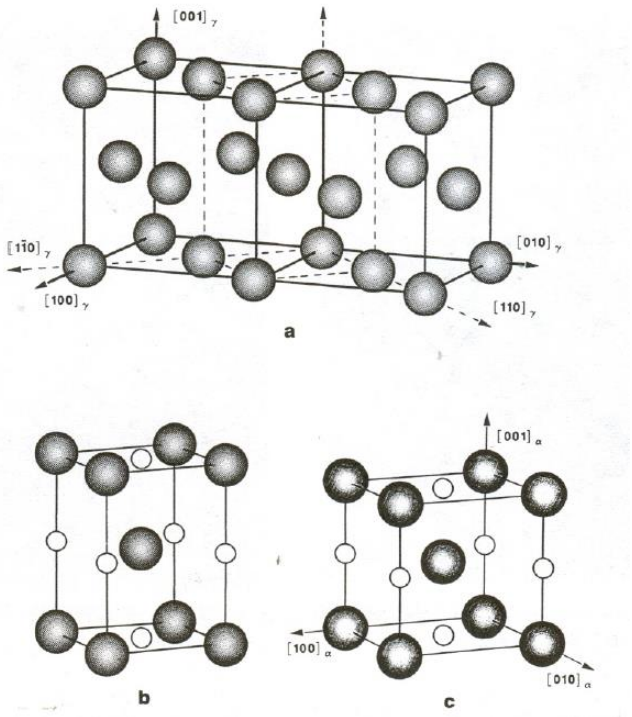

Figure 1.1 Crystal lattices for Fe-C structure. a) Austenite γ (FCC), b) Martensite α' (BCC), c) Ferrite α (BCC). *Olson et Owen "Martensite" (1992, p.245)*

The *Fe-C* diagram shows the transformations that occur in metastable equilibrium for different combinations of carbon concentration and temperature.
These transformations involve energy changes of the closed system. Generally they might be exothermic or endothermic. Considering a general transformation BCC→FCC is important to note that happens a significant variation of the density of the material, in accord with a more compact structure of lattice. The temperature that fixes the change of the characteristics is commonly specified with the letter "A" (anomaly, followed by a numeric index conventionally established). The main temperatures are:

- A_1=723° C - temperature that for the Fe-C steel alloy identifies the equilibrium of the eutectoid transformation between perlite α ⇒austenite γ .
- A_3 =911° C - this temperature identifies the allotropic transformation between α-ferrite and stable austenite γ. This temperature changes according to the percentage of carbon.

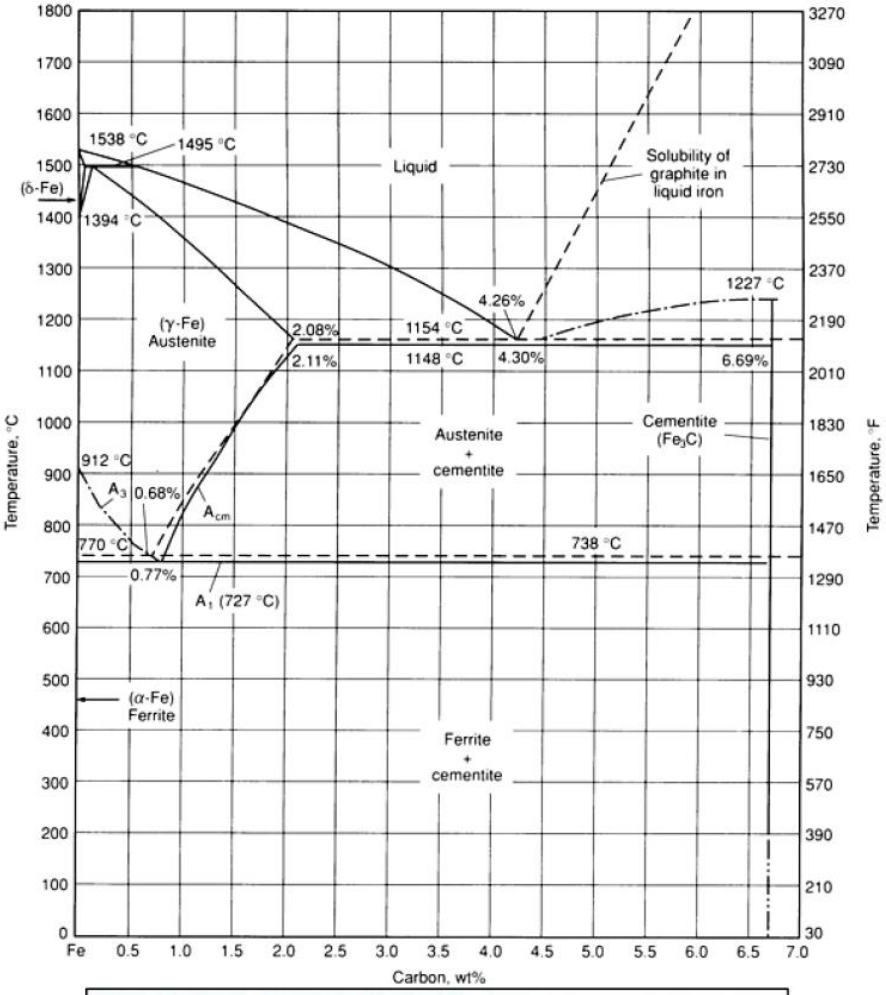

Figure 1.2 The Fe–C diagram up to 6.67%C. Solid lines indicate Fe–Fe_3C diagram; dashed lines indicate iron–graphite diagram. *A.S.M. International,ASM "Handbook Volume4: Heat Treating" , 1991*

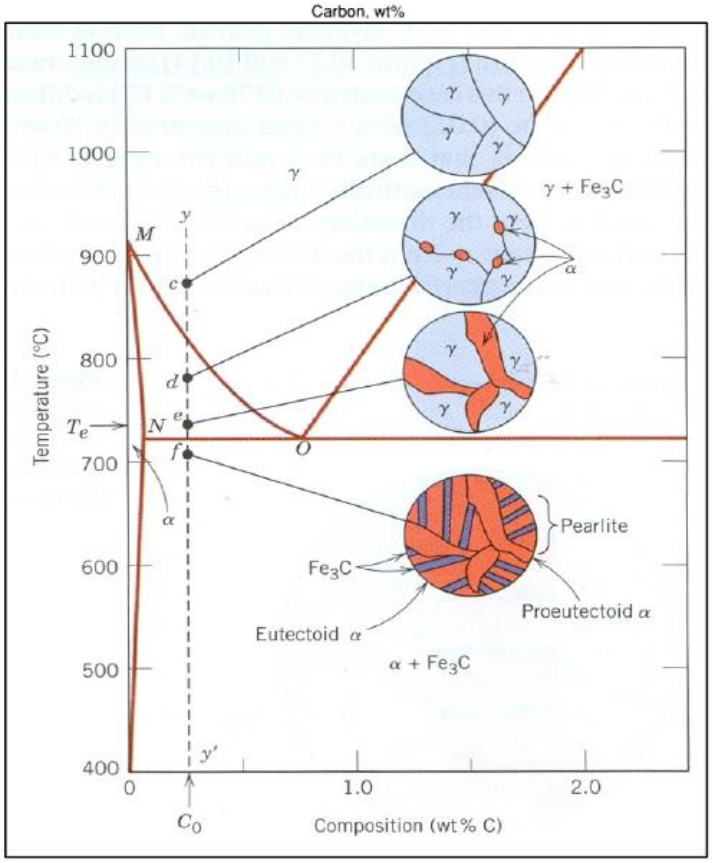

Figure 1.3 The Fe–C phases diagram with the stable microstructures associated for a fixed hypoeutectic alloy. *Callister W.,Rethwisch D." Fundamentals of materials science and engineering" (2008, pag 386)*

Fe–C alloys are characterized by the fact that carbon may exist in different forms: solid solutions, graphite and cementite. Because the development of graphite occurs in conditions of extremely slow cooling, it is easy to understand that graphite represents the stable form of carbon in the Fe–C diagram, whereas cementite is the meta–stable form. The main mixture of two solid phases we can find are:

- Ferrite + cementite (called pearlite)
- Cementite + austenite
- Ferrite + austenite

Heating process and transformation diagrams

The heating in the hardening process consists in bringing the piece to a temperature greater than A_3, so as to complete the transformation into austenitic steel. Fe–C diagram and transformation lines have experimental origin. Some semi–empirical formulation were introduced for steel AISI (*American Iron steel Institute*)–4340 by Andrews (1965) and Semiatin et Stutz (1986). However, A_3 temperature is not simple to calculate, because it depends not only on the carbon content, but also on the presence of other elements which can rise or lower the eutectoid temperature. The austenite–stabilizing elements manganese and nickel decrease A_1, while the ferrite stabilizing elements chromium, silicon, molybdenum and tungsten increase A_1.

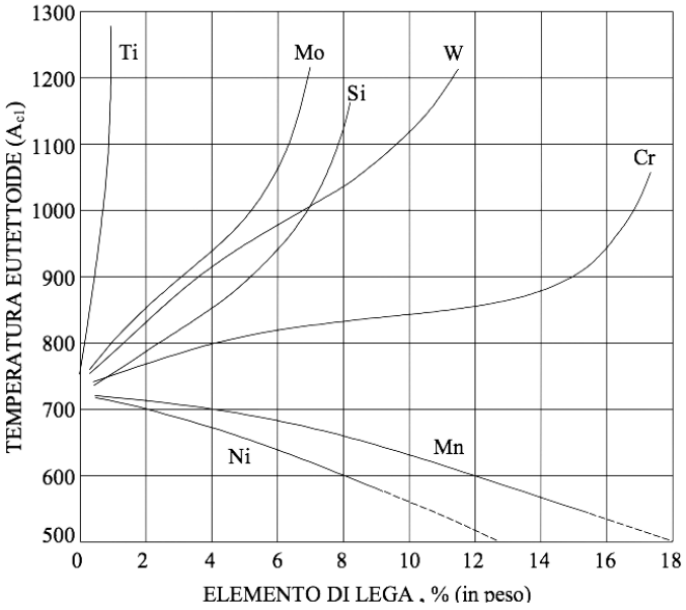

Figure 1.4 Influence of alloying element additions on eutectoid temperature A_1 .
Semiatin,Stutz– "Induction Heat treatment of Steel", 1986

Furthermore, the Fe–C diagram is valid in "thermodynamic equilibrium", which means that the temperature variations are infinitesimal. The transformation temperature A_1 and A_3 are determined both by composition of steel and by heating speed. Two different kind of diagrams help to describe the kinetic aspects of phase transformation processes are:

- IT. *Isothermal transformation diagrams*. They show what happens when steel, with a specific content of carbon, is maintained to a constant temperature for period.
- CT. *Continuous transformation diagrams*. They gather the transformations made with a continuous change of temperature thanks to a constant cooling or heating rate.

Isothermal transformation during heating

This IT diagram describes the process of the formation of austenite from a pre-existent micro structure of ferrite and pearlite or tempered martensite. Abscissa usually defines two different points: the start and finish time as 1% and 99% formation of austenite. In the diagram it are noticeable A_1 and A_3. Below A_1 austenite cannot exist; between A_1 and A_3 there is a mixture of ferrite and austenite. During the formation of austenite from an original microstructure of ferrite and pearlite or tempered martensite, the volume decreases with the formation of the dense austenite phase. The time scale, to plot the starting and final transformation time, is logarithmic. To complete the transformation in a very short time a remarkable overheat is required. The need of a very high heating rate is needed if we want to obtain an accurate isothermal diagram.

Isothermal transformation during cooling

These curves are named in literature as Bain's curves or TTT(Temperature-Time-Transformation) curves. This diagram shows how, starting from austenite at elevate temperature, we arrive to the martensite, the hard structure of steel phases, through a cooling treatment.

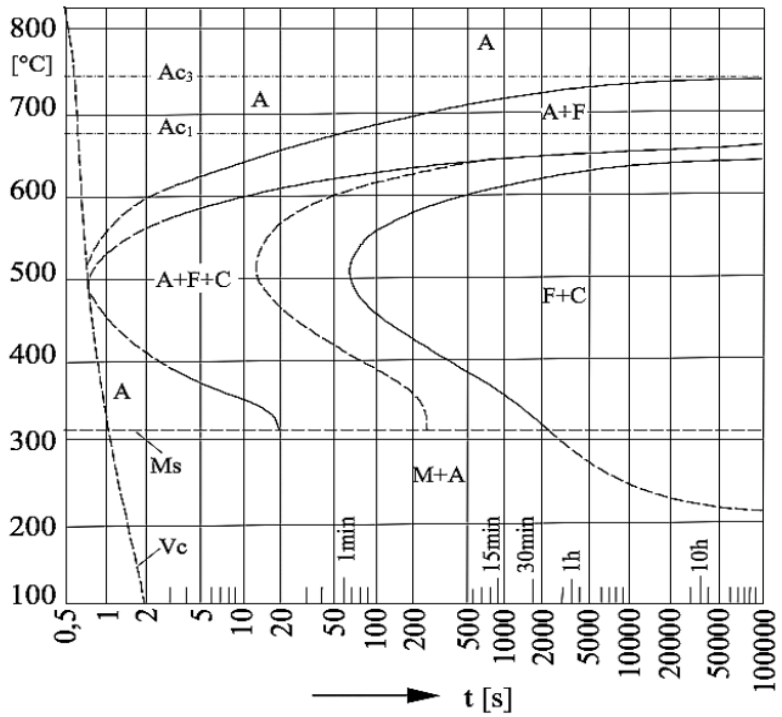

Figure 1.5 Bain's diagram (TTT diagram).
A=austenite,B=bainite,C=cementite,F=ferrite,M=martensite,P=perlite,M_s=martensite start

In case of hardening processes, the martensitic structure and how obtain it are the targets of the whole treatment. It is relevant to underline that above A_3 neither a transformation can occur, while the M_s line denotes the transformation from austenite to martensite.

Continuous cooling transformation diagram

Using a constant cooling rate is very common in experimental practice even if this regime rarely occurs in practice. M_s line is not constant because martensite formation is preceded by bainite formation. Moreover, A_1 and A_3 are neither constant because they are in function of the heating rate.

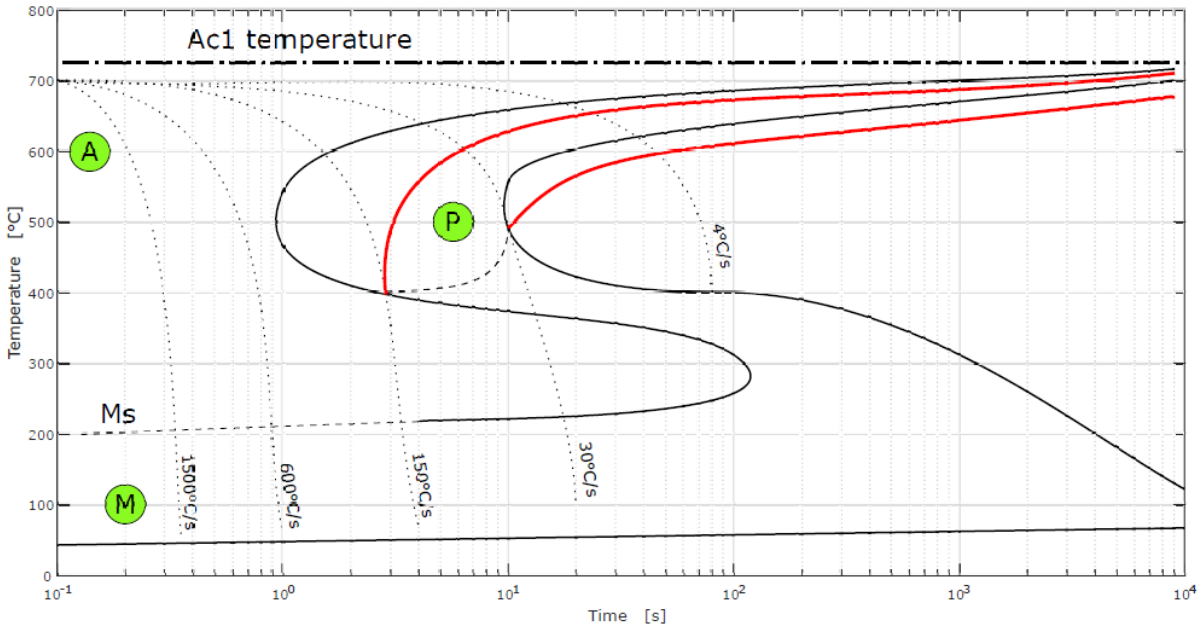

Figure 1.6 Continuous Cooling Transformation diagram for steel AISI−4340
A=austenite,B=bainite,C=cementite,F=ferrite,M=martensite,P=perlite,M_s=martensite start
Lupi," Appunti di elettrotermia" (2005,pag 305)

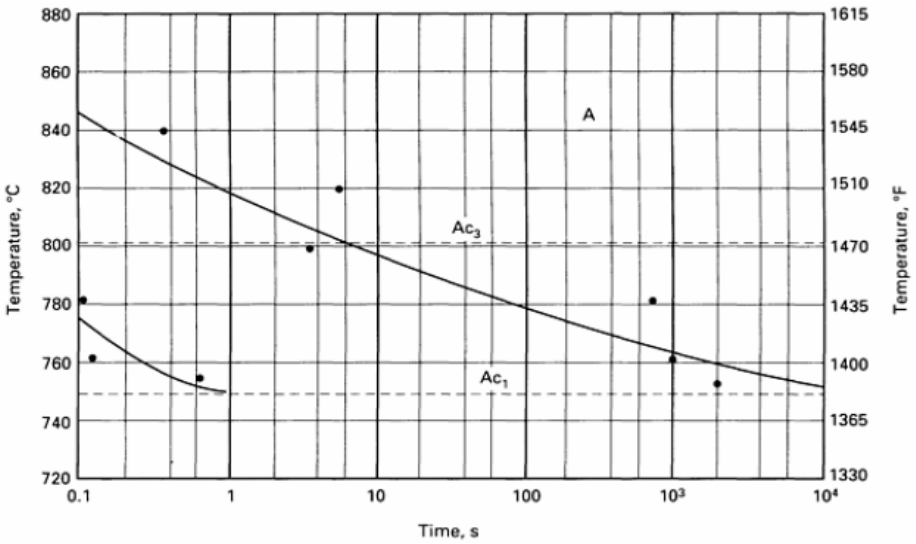

Figure 1.7 Behaviour of A_1 and A_3 with the heating rate in a steel alloy.
Krauss" Steels, processing, structure and performance" (ASM International,2005)

Hardening

The desired value of hardness for a steel workpiece is reached heating a specific zone over the austenization temperature and then quickly cooling it down. In this last part of the treatment, we want to avoid the transformation of austenite in perlite and bainite.
The minimum quenching velocity that allows the full transformation of austenite in martensite is called critic velocity of hardening and is represented in *Figure 1.5* by the dashed line. The transformation into martensite starts with M_s and ends with M_f; as already mentioned the temperature value changes according to the presence of other alloy elements. The variation of the cooling rate with the distance from surface is particularly important and causes distortions inside the piece. Surface hardening process takes the most from this property obtaining hardening thickness extremely thin. Therefore, the main aspects to take into account to obtain the desired hardening profile are: the hardenability (presence of alloy elements), the mass of the workpiece and the hardening depth.

Quenching

The depth of hardness at a given workpiece dimension is determined by the chemical composition of the steel, the austenite grain size as established during the austenitizing treatment and the cooling rate. The steel is normally chosen on the basis of hardenability. The choice of cooling medium, is less exact and crude rules are normally applied (unalloyed steel is quenched in water, alloy steels in oil, high alloy steels in air) Molten salt bath is often used for bainitic hardening of medium-carbon steels. Judicious selection of cooling medium is critical for obtaining optimum mechanical properties, avoiding quench cracks, minimizing distortions and improving reproducibility in hardening. As a matter of facts every media has a different cooling rate. We would like to have the fastest cooling until M_s and then a slow cooling until M_f , because the change of the crystal lattice brings volume transformation that generate cracks if they are too fast. During quenching, the most important thing is to avoid the perlite knee in the Bain's diagram.

Tempering

Previous normalized or hardened steels are tempered to obtain specific values of mechanical properties, to relieve quenching stresses, and to ensure dimensional stability. They usually are reheated below the lower critical temperature and cooled at a suitable rate, primarily to increase ductility and toughness, but also to increase the grain size of the matrix. Steels are tempered to relief quenching stresses and to ensure dimensional stability. As a matter of facts, hardness is directly related to tensile strength, steel composed of 100% martensite s as its strongest possible condition. However, the condition of highest strength is also the condition at which steel is most subject to brittle fracture due to lack of ductility.

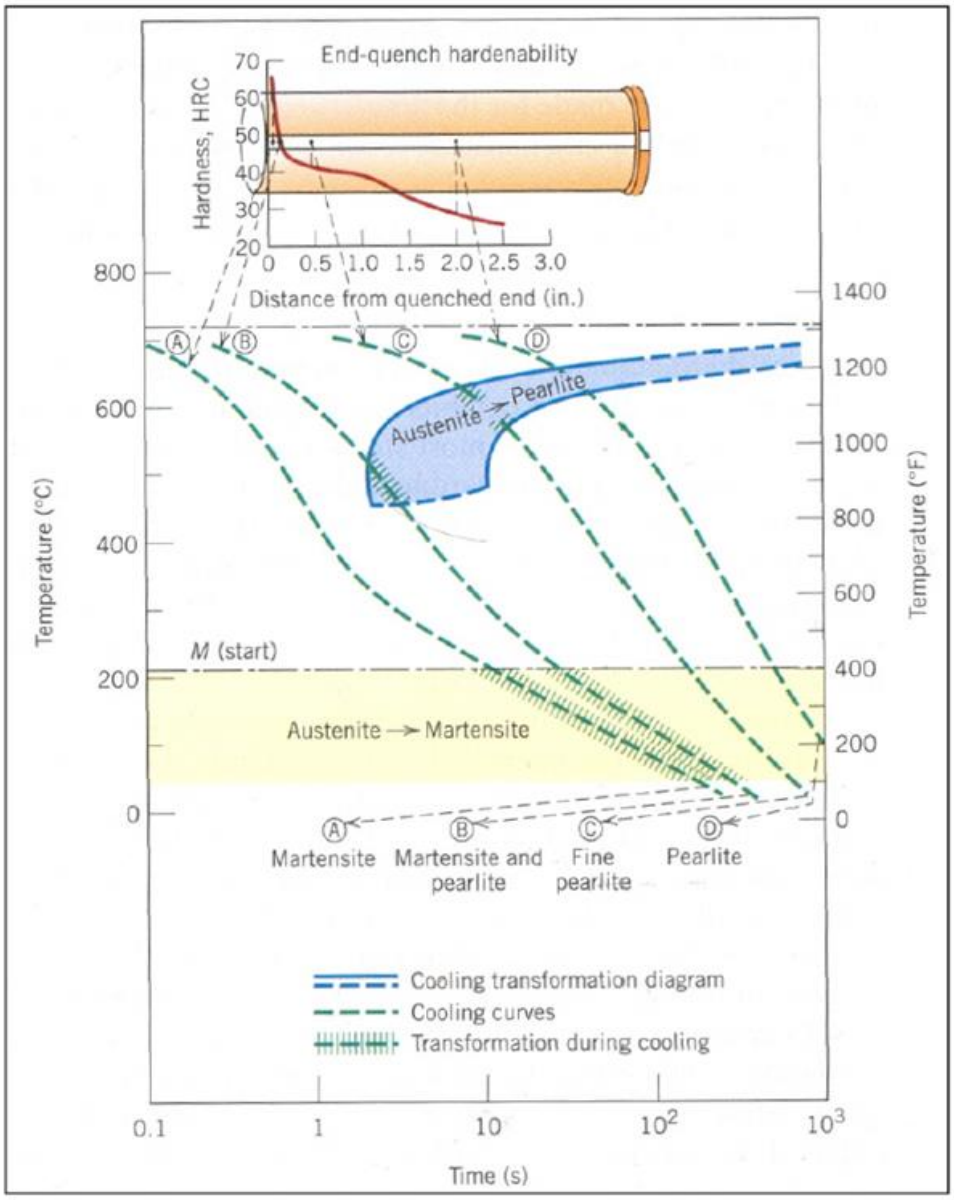

Figure 1.8 Correlation between hardness and cooling rate in a steel alloy.
Callister W.,Rethwisch D." Fundamentals of materials science and engineering" (2008, pag 580)

Surface Hardening

The surface hardening is one of the most interesting application for induction heat treatments. The target is to hard a specific layer, which thickness depends on the application of the workpiece. The hardening is obtained with the use of a high frequency source, that allows to heat up a surface layer above the critical temperature A_3 which corresponds to the transformation temperature of austenite. Successively we cool quickly it to bring the layer to a temperature lower than the martensitic formation one. The main problem of this treatment is that it does not exist a general law to establish the distribution of the heat sources, related with the distribution of the currents induced inside the piece. The same problem presents itself for the times of heating and the value of power and frequency.

That is the reason why the applications of numerical simulation are expanding and becoming even more widespread. This is particularly true for gears and toothed wheels.

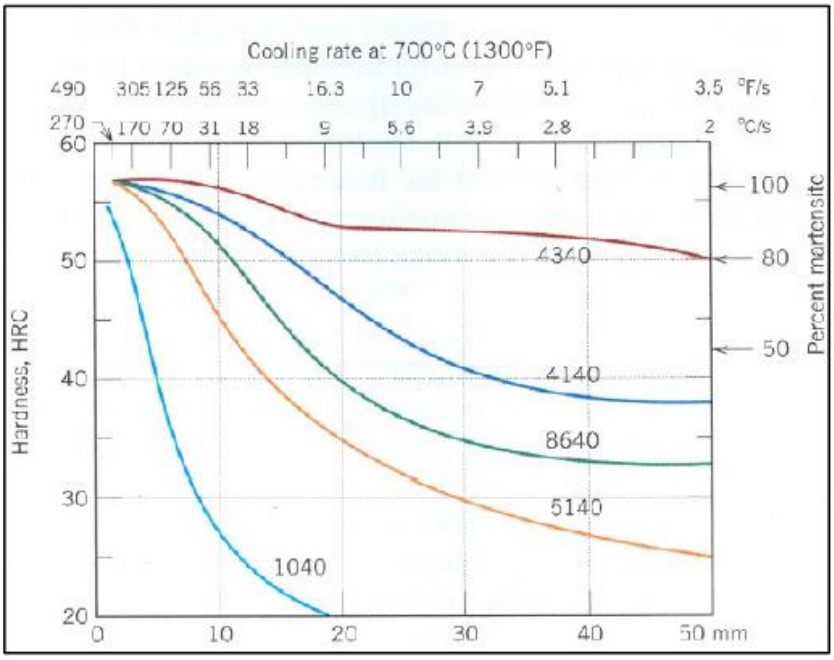

Figure 1.9 Hardness curve of steel AISI–4340 and other alloys.
Callister W. ,Rethwisch D." Fundamentals of materials science and engineering" (2008, pag 580)

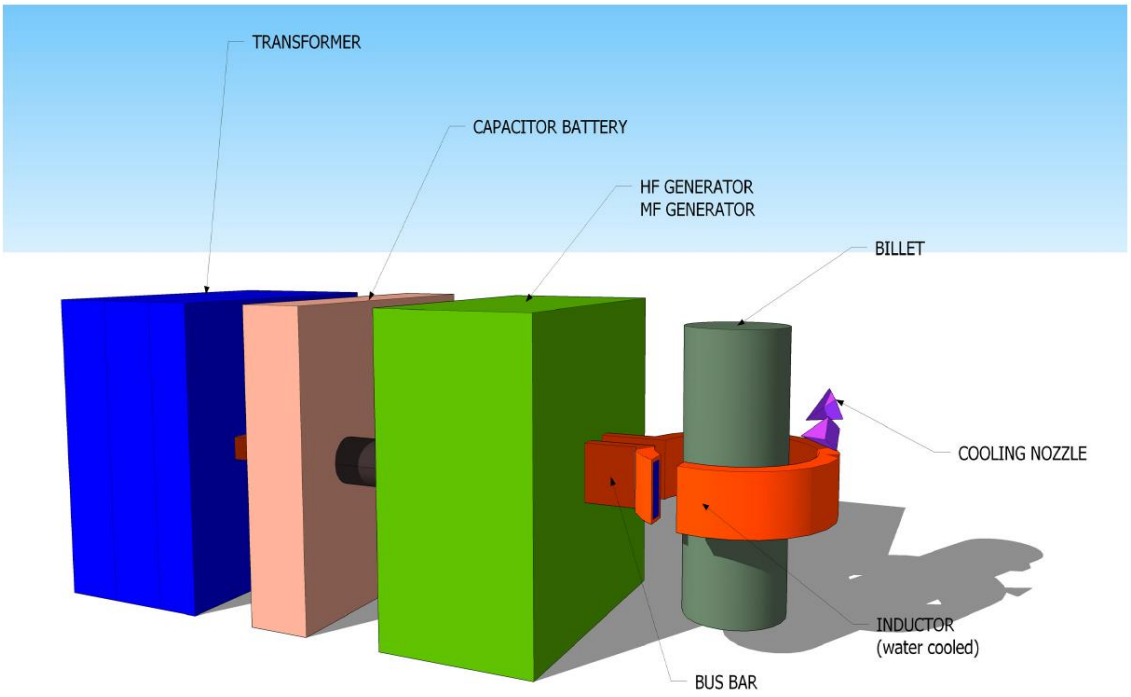

Figure 1.10 Configuration of a SDF induction heater system.

As a matter of fact, in cases of complex geometry we have not uniform heating and quenching profiles with time invariant power distribution. Changing the frequency, we see that the surface of the tooth receives greater power than the surface of the root. With a uniform distribution of power along the surface at high frequency hence, the tips get overheated. The opposite phenomenon occurs in the case of medium frequency, which causes the penetration of induced currents towards the heart of the tooth and causes overheating of the base of the tooth. For this reason, the concept of SDF (simultaneous double frequency) might help to obtain an inhomogeneous distribution of eddy currents but a uniform hardening profile along the surface of the wheel.

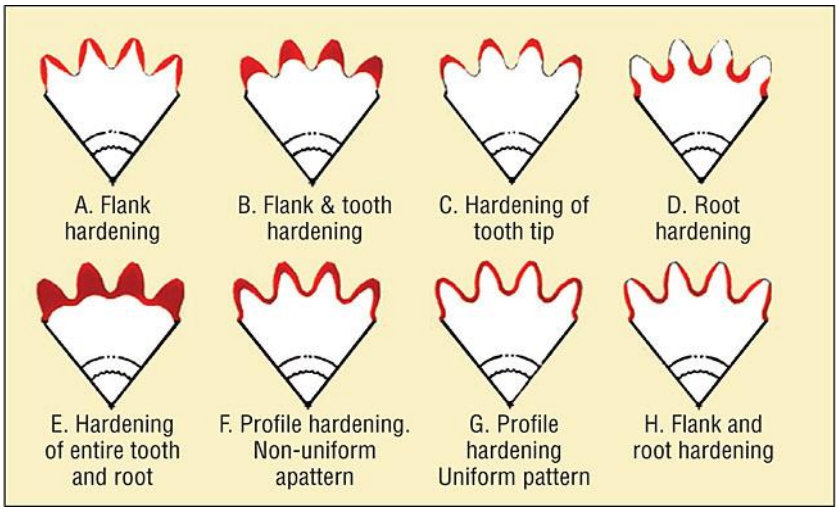

Figure 1.11 different hardening profiles in gear wheels geometry.
Rudnev V.– Loveless G. "Handbook of Induction Heating", (2003)

1.2 Fields Theory

Maxwell's equations are a set of partial differential equations that describe electromagnetic interactions.
They express the time evolution and the boundaries that the electromagnetic field has in relation to the charge density $\boldsymbol{\delta}$ and electrical current J $[\mathrm{A/m^2}]$ by whom it is generated. The equations show how, both the magnetic and the electric field are two manifestations for the same entity, i.e. the electromagnetic field. As a matter of fact, the equations link each other the Magnetic field H [A/m], the Induction Magnetic field B $[\mathrm{Vs/m^2}]$, the Electric field E [V/m] and the Electric Displacement field D $[\mathrm{As/m^2}]$ that have all time and space dependence.
The Maxwell's equations are the following:

$$\boldsymbol{\nabla}\times\bar{\mathrm{E}} = -\frac{\partial \bar{B}}{\partial \mathrm{t}} \qquad (Faraday's\ law) \tag{1.1}$$

$$\boldsymbol{\nabla}\times\bar{\mathrm{H}} = \bar{J} + \frac{\partial \bar{D}}{\partial \mathrm{t}} \qquad (Ampere's\ law) \tag{1.2}$$

$$\boldsymbol{\nabla}\cdot\bar{B} = 0 \qquad (Gauss's\ law) \tag{1.3}$$

$$\boldsymbol{\nabla}\cdot\bar{D} = \delta \qquad (Gauss's\ law) \tag{1.4}$$

In addition to these equations, we can easily add another one that expresses the charge conservation and it is obtained applying one of the vectorial identities.

$$\boldsymbol{\nabla}\cdot\bar{J} = -\frac{\partial \delta}{\partial \mathrm{t}} \tag{1.5}$$

However, to solve the system of Maxwell's equations it is necessary to add to the model the Constitutive Laws that connect different fields each other and represent the coefficient of the partial differential equations.

$$\bar{B} = \mu\bar{\mathrm{H}} \tag{1.6}$$

$$\bar{D} = \varepsilon\bar{E} \tag{1.7}$$

$$\bar{J} = \sigma\bar{\mathrm{E}} \tag{1.8}$$

Where $\mu = \mu_0\mu_r$ expresses the magnetic permeability [H/m] product of the vacuum magnetic permeability μ_0 and the relative magnetic permeability. In case hysteresis losses are considered, the relative magnetic permeability becomes a complex number

with a real component and an imaginary one. The imaginary part is negative due to the delay of the magnetic flux (macroscopic effect of the orientation of the magnetic dipoles), that tries to align with the external magnetic field.

$$\mu_0 = 4\pi * 10^{-7} \left[\frac{H}{m}\right] \tag{1.9}$$

The electric conductivity σ [S/m] can be seen as the inverse of electric resistivity $[\Omega/m]$. As concerning the electric constitutive law, we find that $\varepsilon = \varepsilon_0\varepsilon$ [F/m] is the electrical permittivity where ε_0 is the vacuum electric permittivity.

$$\varepsilon_0 = 8.85 * 10^{-12} \left[\frac{F}{m}\right] \tag{1.10}$$

It is possible to express Maxwell's equations in their integral form with the help of Stokes and Green's theorems that describe the statement of integration of differential formulation and the integration by parts in several dimensions.

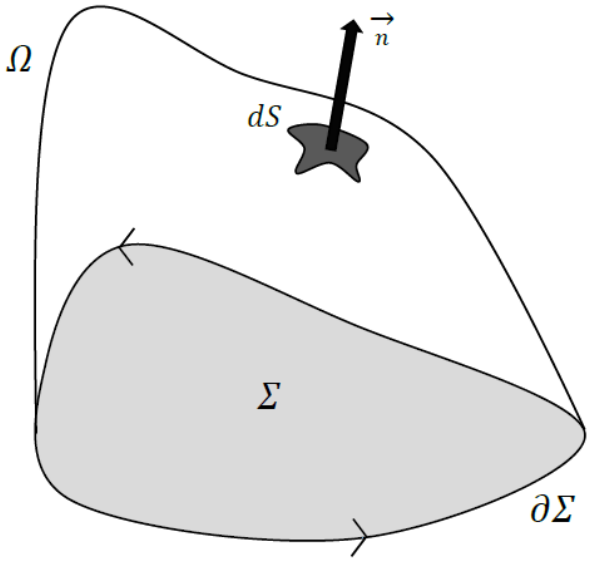

Figure 1.12 Domain **Ω**, surface **Σ** and closed loop **∂Σ**

After that we have defined an arbitrary surface Σ whose support is a closed path ∂Σ, the surface integral of the curl of the electric field (i.e. Maxwell's Induction law (1.1)) becomes:

$$\int_{\Sigma} \nabla\times\bar{\mathrm{E}}\, dS = \oint_{\partial\Sigma} \bar{\mathrm{E}} \cdot d\boldsymbol{l} = -\frac{\partial}{\partial t}\int_{\Sigma} \bar{B} \cdot \boldsymbol{n}\, dS$$

That is usually written in literature with the Magnetic Flux $\Phi\,[T\,m^2]$ troughout the surface Σ as:

$$f.e.m. = -\frac{\partial \Phi}{\partial t} \tag{1.11}$$

Proceeding with the same integration method, we can implement the Ampere–Maxwell's law (1.2) and achieve the integral expression:

$$\oint_{\partial\Sigma} \overline{\mathrm{H}} \cdot d\boldsymbol{l} = \int_{\Sigma} \bar{\mathrm{J}} \cdot \boldsymbol{n}\, dS + \frac{\partial}{\partial t}\int_{\Sigma} \overline{\mathrm{D}} \cdot \boldsymbol{n}\, dS \tag{1.12}$$

Applying the Green's integral formulation to the magnetic Gauss law (1.3) we demonstrate that $\bar{B}$ is a solenoidal so, sources and shafts do not exist for the magnetic flux. Therefore, this last equation says that the Magnetic Flux through a closed surface $\partial\Omega$, that includes the volume region Ω, must be null.

$$\int_{\Omega} \boldsymbol{\nabla} \cdot \bar{B}\, dV = \int_{\partial\Omega} \overline{\mathrm{B}} \cdot \boldsymbol{n}\, dS = 0 \tag{1.13}$$

The last integral form that must be defined is the Conservation of the electric charge. The integration of the divergence of the electric current, implementing Green's law, admits obtaining the following relation between the total current and the total electric charge.

$$\int_{\partial\Omega} \bar{\mathrm{J}}\, dS = -\frac{\partial}{\partial t}\int_{\Omega} \delta\, dV \tag{1.14}$$

Boundary conditions

In order to solve the electromagnetic problem and find a unique solution, I need boundary conditions for every instant and initial condition for every point (in addition to Maxwell equations and material's equations). As a matter of fact in mathematics, in the field of differential equations, a boundary value problem is a differential equation together with a set of additional constraints, called the boundary conditions. I can have different types of conditions but the most common are the Dirichlet and the Neumann conditions that define different behaviour if they are related to an electrical or a magnetic field.

Dirichlet boundary condition

A Dirichlet boundary condition is a type of condition that imposes on an ordinary or a partial differential equation the values that a solution needs to take along the boundary of the domain.

$$U = U_0\,(x, y, z) \tag{1.15}$$

A Dirichlet condition on a boundary for the electric potential V says that the electric field E has not tangential component because E is perpendicular to an iso−line of electric potential. Otherwise the same condition imposed for the magnetic vector potential A means that the normal component of B is zero.

Neumann boundary condition

A Neumann condition specifies the values that the derivate of a solution, of an ordinary or partial different equation, takes on the boundary of the domain.

$$\frac{\partial U}{\partial n} = \nabla \mathbf{U} \cdot \boldsymbol{n} = f(x, y, z) \tag{1.16}$$

For every point of the boundary, $\boldsymbol{n}$ is the normal to the boundary and *f(x,y,z)* is a given scalar function. Homogeneous Neumann conditions imposes that the scalar function is null.

A Neumann condition for the electric potential V says that E has not normal component because $\nabla \mathbf{V} \cdot \boldsymbol{n} = 0$. Consequently, due to the fact that $\mathrm{E} = -\nabla \mathbf{V}$ we deduce the same conclusion mentioned before: the normal component is equal to zero. As concerning the magnetic vector potential A, the Neumann condition means that the tangent component of B is zero.

Interface conditions

Usually when there are different materials we also need interface conditions, because it is possible that these materials are characterized by a various behaviour of the fields. In literature, is commonly defined as normal or tangential component conservation of fields and it depends from the kind of the field that we want study. It is seen that the normal conservation is related to the fields associated to the divergence theorem while the conservation of the tangential component is related to the fields associated with the curl theorem.

Conservation of the normal component

Let us consider a coin shape volume that corresponds to an infinitesimal cylinder which height dimension is much smaller than its radius.

This flattered cylinder can be built in the interface between two different regions, characterized by two materials with different magnetic permeabilities.

Let us start taking in consideration the induction magnetic field B to prove the conservation of the normal component.

The total magnetic flux in the volume is:

$$\Phi_{tot} = \Phi_{\text{top}} + \Phi_{\text{bottom}} + \Phi_{\text{side}} \tag{1.17}$$

Then, assuming that the magnetic flux is constant in a small coin surface, and neglecting the flux outgoing from the side of the volume we have:

$$\oint_{\Sigma} \bar{B} dS = \bar{B}_1 \, \bar{n}_1 \, S_1 + \bar{B}_2 \, \bar{n}_2 \, S_2 = 0 \tag{1.18}$$

The equivalence of the left−hand side of the equation (1.18) to zero is a direct consequence of the divergence law (1.3).

Considering that the normal of the top surface is equal to the one of the bottom with opposite sign we can rewrite:

$$\bar{B}_1 \, \bar{n}_1 = \bar{B}_2 \, \bar{n}_2 \tag{1.19}$$

Which implies that I do not have variation of the normal component of B across the interface.

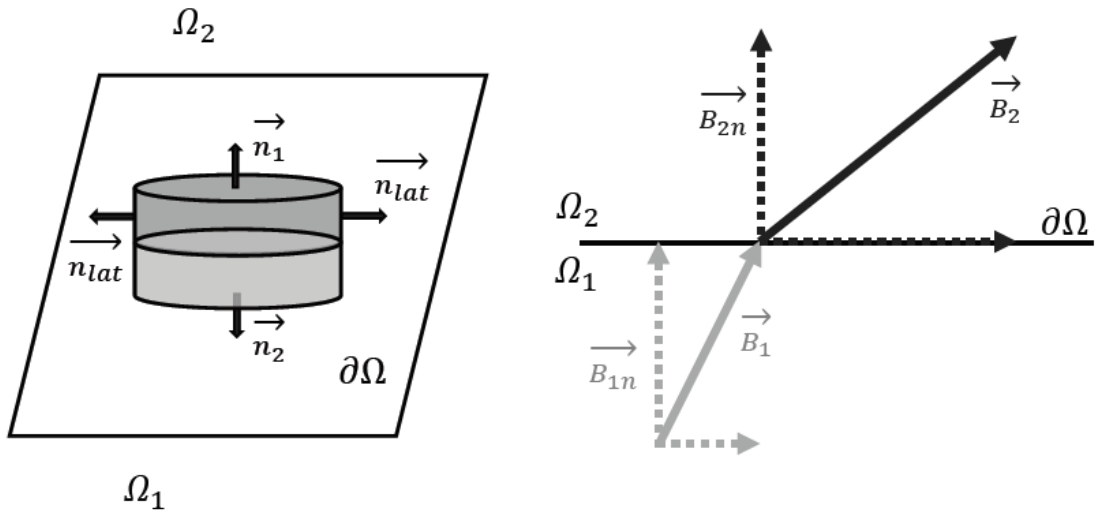

Figure 1.13 Infinitesimal cylinder with the interface **$\partial\Omega$** that separates two regions with different material parameters. Conservation of the normal component

In the case of the electric displacement vector, it is possible to proceed in the same way, calculating the integral of the divergence.

$$\oint_{\Sigma} \bar{D} dS = \bar{D}_1 \, \bar{n}_1 \, S_1 + \bar{D}_2 \, \bar{n}_2 \, S_2 = 0 \tag{1.20}$$

That implicates the conservation of the normal component of D.

$$\bar{D}_1 \, \bar{n}_1 = D_2 \, \bar{n}_2 \tag{1.21}$$

These two last equations are valid under the hypothesis of superficial charge density $\delta = 0$, in the case it is not valid we obtain a total surface charge Qs and we do not have the conservation of the normal component.

$$\bar{D}_1 \, \bar{n}_1 S_1 + \bar{D}_2 \, \bar{n}_2 S_2 = \delta S = Qs \tag{1.21}$$

Conservation of the tangential component

Now let us analyse the conservation of the tangential component in the electric and magnetic fields E and H, starting from the curl theorem.
However, we take into account a different geometry: there is rectangle Σ, whose height is much smaller than its width. For this reason, when the circulation along a closed loop is calculated, the contribution along the heights is neglected because it belongs to a superior order therm. The rectangle structure passes through the boundary between two different regions.
If there is the presence of a current density J from the equation (1.2) it is possible to understand that the curl of the magnetic vector is not zero. Therefore, it is possible to integrate along the rectangle Σ and obtain the conservation of the tangent component of the magnetic field, below the hypothesis that the time derivate of the Electric Displacement field must be negligible.

$$\bar{H}_1\,\bar{t}_1 = \bar{H}_2\,\bar{t}_2 + \int_{\Sigma} \bar{J}\cdot\boldsymbol{n}\,dS \tag{1.22}$$

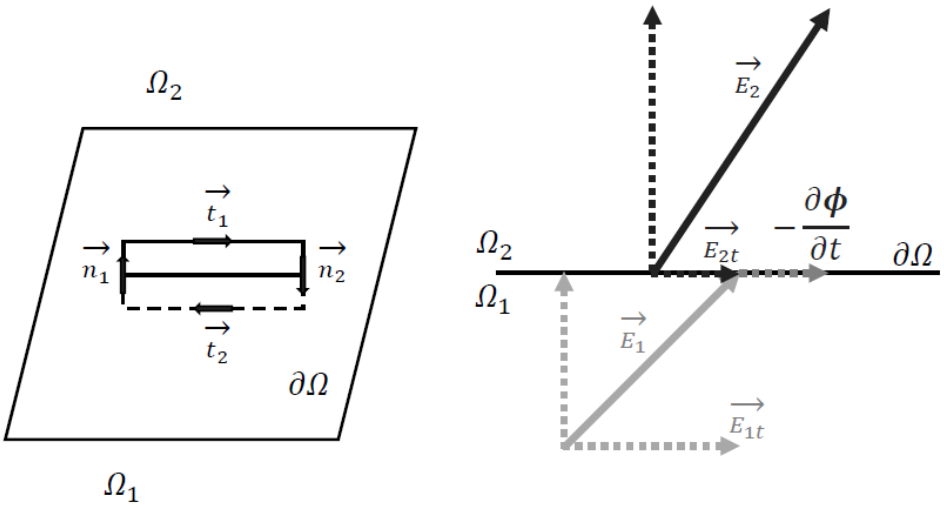

Figure 1.14 Infinitesimal rectangle with the interface $\partial\Omega$ that separates two regions with different material parameters. Conservation of the tangential component

Making a similar line of reasoning with the electric field, we obtain:

$$\int_{\Sigma} \nabla\times\bar{E}\,dS = \oint_{\partial\Sigma=l} \bar{E}\cdot d\boldsymbol{l} = -\frac{\partial\Phi}{\partial t} \tag{1.23}$$

In this case, however the integral is different from zero because of the jump due to the variation of the magnetic inductor vector.

$$\bar{E}_1\,\bar{t}_1 = \bar{E}_2\,\bar{t}_2 - \frac{\partial\Phi}{\partial t} \tag{1.24}$$

1.3 Magneto Quasi static formulation

Starting from Maxwell's equation it is possible to introduce some simplifications for the application of induction heating that we are going to study in this paper. As the name might suggest in the Magneto Quasi static formulation the magnetic field is dominant compared to the electric one. As a matter of fact, not only the electric polarization vector is negligible for conductive materials but also, we can neglect the time derivative of the electric displacement field. It is easily demonstrable for a model in which the sources are sinusoidal and in which it is possible to assume average values for the material parameters. Using the Steinmetz transformation, in the range of frequencies adopted in the induction heating process (that reaches the magnitude of $\sim 10^5$[Hz]), we have:

$$\nabla \times \bar{H} = \bar{J} + \frac{\partial \bar{D}}{\partial t} = \sigma_{el}\bar{E} + j\omega\varepsilon_0\bar{E} \tag{1.25}$$

Considering that the electric conductivity of the steel is $\sim 10^5 [S/m]$, we can see that the displacement current is several orders of magnitude smaller than the conductive one. An additional proof can be provided from constitutive laws : the permeability is greater than the permittivity, in sinusoidal regime and in the considered frequency range:

$$\left|\frac{\partial \bar{D}}{\partial t}\right| = \varepsilon\omega E cos(\omega t) \ll \mu\omega H cos(\omega t) = \left|\frac{\partial \bar{B}}{\partial t}\right| \tag{1.26}$$

Hence, we can write the Magneto Quasi static equations.

$$\begin{cases} \nabla \times \bar{H} = \bar{J} \\ \nabla \times \bar{E} = -\frac{\partial \bar{B}}{\partial t} \\ \nabla \cdot \bar{B} = 0 \\ \nabla \cdot \bar{D} = \delta \end{cases} \tag{1.27}$$

Due to the fact, the B field is sinusoidal, under the hypothesis of a domain simply connected for surfaces, I can define a magnetic vector potential as:

$$\nabla \times \bar{A} = \bar{B} \tag{1.28}$$

Because B is the curl of a vector then it is irrotational because of the *div(curl)* vectorial identity. However, it is important to understand that a whole infinite family of vector potential solve the previous equation.

$$\bar{A} = \bar{A}' + \nabla\Lambda \tag{1.29}$$

Where Λ is a scalar field because the curl of the gradient is zero. The consequence is that to fix the vector potential it is not enough to fix a point but it is required a function. This operation is called gauging and a way to do that is to express the

divergence of the magnetic potential. The most common decision is the Coulomb gauge that fixes the divergence equal to zero.

Moreover, the electric field is irrotational so, under the hypothesis of a domain simply connected by lines, it is possible to introduce an electric scalar potential:

$$\bar{\mathrm{E}} = -\boldsymbol{\nabla}\bar{\mathrm{V}} \tag{1.30}$$

Now it is possible to find a new formulation that describes the electromagnetic problem with two different unknowns: the magnetic vector potential and the electric scalar potential.
Starting from equation (1.27) and introducing (1.29) and (1.30) a new expression for the electric field is obtained:

$$\bar{E} = -\boldsymbol{\nabla}\bar{\mathrm{V}} - \frac{\partial \bar{A}}{\partial \mathrm{t}} \tag{1.31}$$

Where the time derivative of the vector potential is the induced electric field.
Combining both the formulation for electric and magnetic fields with their constitutive laws:

$$\boldsymbol{\nabla}\times\bar{\mathrm{H}} = \bar{J} = \sigma\bar{E} \tag{1.32}$$

$$\boldsymbol{\nabla}\times\frac{1}{\mu}\boldsymbol{\nabla}\times\bar{\mathrm{A}} = \sigma\left(-\frac{\partial \bar{A}}{\partial \mathrm{t}} - \boldsymbol{\nabla}\bar{\mathrm{V}}\right) \tag{1.32}$$

In conclusion I have four unknowns (A_x,A_y,A_z,V) in vectorial and a scalar equation.

$$\begin{cases} \boldsymbol{\nabla}\times\nu\boldsymbol{\nabla}\times\bar{\mathrm{A}} + \sigma\dfrac{\partial \bar{A}}{\partial \mathrm{t}} + \sigma\boldsymbol{\nabla}\bar{\mathrm{V}} = 0 \\ \boldsymbol{\nabla}\cdot\sigma\left(-\boldsymbol{\nabla}\bar{\mathrm{V}} - \dfrac{\partial \bar{A}}{\partial \mathrm{t}}\right) = 0 \end{cases} \tag{1.33}$$

Where ν, named magnetic reluctivity is the inverse of the magnetic permeability.

2D Axial symmetric formulation

It is particularly interesting to deal with 2D axial symmetric problems because they introduce additional simplifications to the electromagnetic problems remaining in accord with a great number of real cases of induction heating.
Geometrical and physical symmetries allow us indeed to describe the components in the $[\mathbf{r},\mathbf{z}]$ plane of a r,z,φ coordinate system.

Thinking of supplying the inductor coil with a current density normal to the [r,z] plane, we can rewrite the magneto quasi static equations in an axial symmetrical formulation because the magnetic field has only z−components.

$$\begin{aligned} \bar{H} &= [H_r, H_\varphi, H_z] = [H_r, 0, H_z] \\ \bar{J} &= [J_r, J_\varphi, J_z] = [0, J_\varphi, 0] \end{aligned} \tag{1.34}$$

The induction magnetic field has the same component of H while the electric field has the same components of J. This is obtained because the constitutive laws are analysed with isotropic materials. Now let us explicit the curl, divergence and rotor in cylindrical coordinates for a generic field W.

$$\nabla \times \bar{W} = det \begin{vmatrix} \bar{r} & \bar{z} & \bar{\varphi} \\ \frac{\partial}{\partial r} & \frac{\partial}{\partial z} & \frac{\partial}{\partial \varphi} \\ W_r & W_z & W_\varphi \end{vmatrix} = \left(\frac{1}{r}\frac{\partial W_z}{\partial \varphi} - \frac{\partial W_\varphi}{\partial z}, \frac{1}{r}\frac{\partial r W_\varphi}{\partial r} - \frac{\partial W_r}{\partial \varphi}, \frac{\partial W_\varphi}{\partial z} - \frac{\partial W_z}{\partial r} \right)$$

$$\nabla \cdot \bar{W} = \frac{1}{r}\frac{\partial r W_r}{\partial r} + \frac{1}{r}\frac{\partial W_\varphi}{\partial \varphi} + \frac{\partial W_z}{\partial z}$$

$$\nabla \bar{W} = \frac{\partial W}{\partial r}\boldsymbol{u_r} + \frac{1}{r}\frac{\partial W}{\partial \varphi}\boldsymbol{u_\varphi} + \frac{\partial W}{\partial z}\boldsymbol{u_z}$$

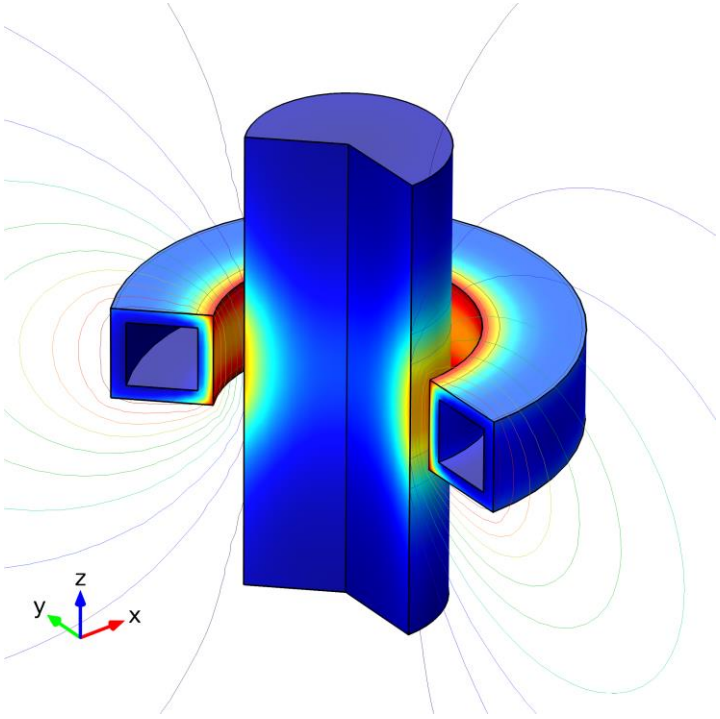

Figure 1.15 Geometrical and physical axial symmetric geometry. Steel billet coupled with an inductor coil in copper.

Because of the curl of a vector must be normal to the vector, we can deduce that the magnetic vector potential has only $\varphi-$component. Therefore, the curl of the magnetic potential becomes:

$$\boldsymbol{\nabla}\times\bar{A} = \left(-\frac{\partial A_\varphi}{\partial z}, 0, \frac{1}{r}\frac{\partial r A_\varphi}{\partial r}\right) \tag{1.35}$$

Consequently, the Ampere−Maxwell law is:

$$\boldsymbol{\nabla}\times\nu\boldsymbol{\nabla}\times\bar{A} = \left(0, \frac{\partial}{\partial z}\left(-\nu\frac{\partial A_\varphi}{\partial z}\right) - \frac{\partial}{\partial z}\left(\nu\frac{1}{r}\frac{\partial r A_\varphi}{\partial r}\right), 0\right) = (0, J_\varphi, 0) \tag{1.36}$$

Then by multiplying the first term for *r/r* and by defining $\boldsymbol{\nu'} = \frac{\boldsymbol{\nu}}{\boldsymbol{r}}$ *and* $\mathbf{rA} = \boldsymbol{\Phi}$ I get:

$$\frac{\partial}{\partial z}\boldsymbol{\nu}'\frac{\partial \Phi}{\partial z} + \frac{\partial}{\partial r}\boldsymbol{\nu}'\frac{\partial \Phi}{\partial r} = -J_\varphi \tag{1.37}$$

That is a formulation of the div(grad) kind

$$\boldsymbol{\nabla}_\mathbf{a}\cdot\nu'\,\boldsymbol{\nabla}_\mathbf{a}\Phi = -J_\varphi \tag{1.38}$$

1.4 Fourier's Equation

In the heating process of isotropic solids, temperature of each element is a function of spatial coordinates and time $T = T(x, y, z, t)$.

Dealing with a heating treatment, it is possible to define the isotherms inside the body instant by instant. The evolution of these lines describes how temperature distribution changes inside the body. The heat equation is a parabolic partial differential equation that describes the distribution of heat and the variation with the temperature in a given region over the time.

The heat equation, derived from Fourier's law describes the rate of flow of heat energy per unit area through a surface. It is proportional to the negative temperature gradient across the surface: the Fourier's equation defines the relation for each point P of the domain, between the specific thermal flux $\boldsymbol{p}$ [W/m^2] and the temperature gradient.

$$\boldsymbol{p} = -\lambda\frac{\partial \mathrm{T}}{\partial \mathrm{n}} = -\lambda\,\boldsymbol{\nabla}\mathrm{T} \tag{1.39}$$

Where n is the normal vector of the surface, oriented to the direction of increasing temperatures, and λ [W/m^2] the thermal conductivity.

Explicating the three−dimensional coordinate, we can rewrite the thermal flux as:

$$\boldsymbol{p} = -\lambda\frac{\partial \mathrm{T}}{\partial \mathrm{x}}\boldsymbol{u_x} - \lambda\frac{\partial \mathrm{T}}{\partial \mathrm{y}}\boldsymbol{u_y} - \lambda\frac{\partial \mathrm{T}}{\partial \mathrm{z}}\boldsymbol{u_z} \tag{1.40}$$

The general equation of conduction expresses the energy balance of an infinitesimal element of the body dV. This means that the sum of thermal fluxes throughout the lateral surface can be written as:

$$dP_s = \sum_{i \epsilon N} dP_i = \sum_i P_i dA_i = -\boldsymbol{\nabla} \cdot \boldsymbol{p} dV$$

Energy that is transformed in heat inside the solid piece is:

$$dP_w = w(P,t)dV$$

Where w [W/m^3] is the specific power inside the piece. The internal increase of internal energy in the sample is:

$$dP_c = c\gamma \frac{\partial T}{\partial t} dV$$

When the parameter $\boldsymbol{c}$ that compares in the expression is the specific heat capacity [J/kgK] and $\boldsymbol{\gamma}$ [kg/m^3] is the mass density. At this point it is possible to impose the conservation of energy and power for the whole system:

$$dP_c = dP_s + dP_w.$$

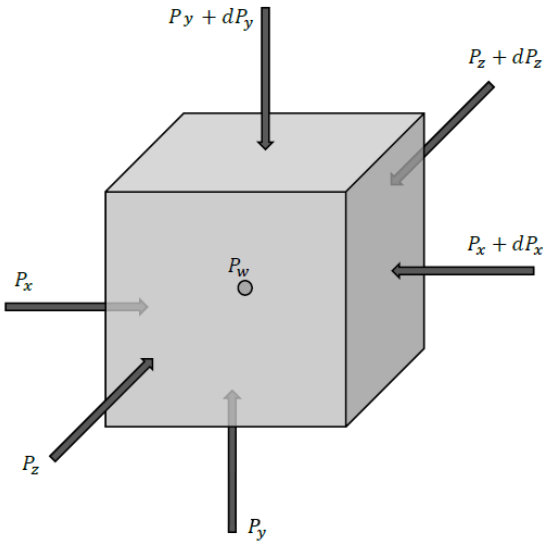

Figure 1.16 Conservation of thermal energy in an infinitesimal volume dV.

Consequently, we arrive to the more known Fourier's second order differential equation for thermal transients:

$$c\gamma \frac{\partial T}{\partial t} = -\nabla \cdot \lambda \nabla \mathrm{T} + w(P,t) \qquad (1.41)$$

As already done with Maxwell's equation we can write the PDE in an axial symmetric coordinate system:

$$c\gamma \frac{\partial T}{\partial t} = \frac{1}{r}\frac{\partial}{\partial r}\left(\mathrm{r}\lambda \frac{\partial T}{\partial t}\right) + \frac{1}{\mathrm{r}}\frac{\partial}{\partial \varphi}\left(\frac{1}{\mathrm{r}}\lambda \frac{\partial T}{\partial \varphi}\right) + \frac{\partial}{\partial \mathrm{z}}\left(\lambda \frac{\partial T}{\partial \mathrm{z}}\right) + \mathrm{w}(\mathrm{r}, \varphi, \mathrm{z}, \mathrm{t}) \qquad (1.42)$$

If the material presents isotropic and homogeneous parameters we can rewrite again the equation putting in evidence the thermal diffusivity $\boldsymbol{k} = \frac{\boldsymbol{\lambda}}{\boldsymbol{c\gamma}}$ [m²/s]

$$\frac{\partial T}{\partial t} = \frac{\lambda}{c\gamma}\left[\frac{\partial^2 T}{\partial r^2} + \frac{1}{r}\frac{\partial T}{\partial r} + \frac{1}{r^2}\frac{\partial^2 T}{\partial \varphi^2} + \frac{\partial^2 T}{\partial z^2}\right] + \frac{\mathrm{w}}{c\gamma}(\mathrm{r}, \varphi, \mathrm{z}, \mathrm{t}) \tag{1.43}$$

Boundary conditions

To establish the solution of Fourier's equation is required the knowledge of the boundary conditions. As a matter of fact, the boundary conditions in thermal problems describes the heat exchange between the external ambient and the workpiece.
In induction hardening problems, even if the process is considerably fast, we have to consider the thermal interaction of the body. The main heat flows outward of the problem are convection and radiation.

$$P_{conv} = \lambda \nabla T = \alpha(T - T_{ext}) \tag{1.44}$$

$$P_{rad} = \frac{5{,}67 * 10^{-8}}{\frac{1}{\varepsilon} + \frac{S}{S_a}\left(\frac{1}{\varepsilon_a} - 1\right)}(T^4 - T_{ext}^4) \tag{1.45}$$

Where ε and ε_a are respectively the emissivity of the surface of the material, and the absorption coefficient. S and S_a are the radiating surface and the absorbing surface. The Boltzman's constant has been explicated and it is recognizable the term with the difference of the temperatures to the magnitude of four. Typically, we can approximate this formulation neglecting the radiating surface than the absorbent one.

$$P_{rad} = \sigma\varepsilon(T^4 - T_{ext}^4) \tag{1.46}$$

Chapter 2

Finite Elements Method

The finite element method is the most flexible method to solve partial differential equations problems (PDEs), transforming them in linear systems $Ax=b$ where A is a sparse matrix, x is the unknown vector and b is the column of the known terms.
FEM can be seen from two different approaches, one is called Variational approach and the other is the Weighted Residual approach. By applying them to a PDE system, they give the same set of equations to solve but, while in the Variational it is needed a Functional to be minimized, in the second one it is needed only the differential equation that describes our problem.

The residual approach wants to find a potential U, generally expressed by polynomial functions, that satisfies simultaneously the boundary conditions (applied to the domain omega where the problem is defined) and the PDEs. The kernel of the FEM is that it splits the domain in a finite number of elements.
The geometry of these elements depends on the space dimension of interest. Because the number of degrees of freedom increases exponentially with the number of dimension, from an engineering point of view, there is the necessity to restrain the "weight of the simulation". Using all the possible symmetries, we limit the number of elements decreasing drastically the amount of time required.
The next paragraphs will introduce the main points of a finite element method.

2.1 Structure of a FEM

Mesh

The finite element method takes its name by the fact that is based on elements, which fill finite regions of the space. A finite element is a geometric entity suited to fill a portion of the spatial domain of the problem. In 1D the elements are segments, in 2D the elements are usually triangles and quadrilaterals and in 3D the elements are hexahedra, tetrahedral, square based pyramids and prisms.
The mesh composed by these elements must have some characteristics:

- it must be conformed to interfaces; that means that no element can fill portions of different regions with different material properties.
- the region Ω must be completely covered and there cannot be intersections between elements.
- two elements can have in common a node, an entire edge, a face or any geometry entity.

It is clear that, if we consider triangular elements in 2D dimension, it is possible to define for everyone its vertices that correspond to Lagrange points. Therefore, if we consider a region settled of a certain number of elements, it is possible to find a certain Lagrange point that is surrounded by different elements. This set that has the $i-$point as vertex is called support area of the node i(Ω_i). This compact support (closed and bounded) is very important to define an interpolant function to solve the problem numerically.

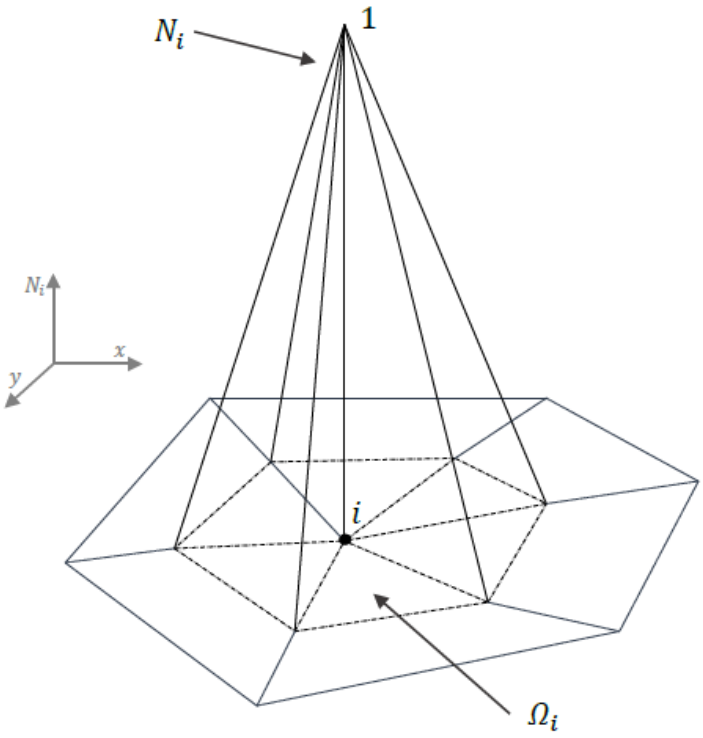

Figure 2.1 Support area for the node i in the 2D case. The interpolant function is linear: k=1.

Interpolant function of elements

The interpolating function of the node i, is a piecewise polynomial function and it can be of first degree, second or a generic k degree, but it is always continuous in Ω. The degree of the shape function can be chosen arbitrarily; it is important to underline that increasing the degree requires more middle points and more time to the solver to compute the linear system.
Considering the interpolant function of the node i restricted to each element e_i

$$N_i^j = N_i(x \in e_j)$$

the interpolant of the node i can be written as the sum of the N_i^j

$$N_i = \sum_{j=1}^{n_e} N_i^j = \begin{cases} \sum_{j=1}^{n_{\Omega i}} N_i^j & x \in \Omega_i \\ 0 & x \in \left(\frac{\Omega}{\Omega_i}\right) \end{cases} \tag{2.1}$$

Where n_e is the total number of elements and $n_{\Omega i}$ is the number of elements which compose the support area of *i*. Multiplying each interpolant for a constant and then summing them all together we get the polynomial function of the same degree of the original ones. Therefore, we can obtain the interpolation of the nodal potential in a generic element by doing the sum of the interpolant weighted with the potentials of the corresponding nodes. In this way it is defined a function which extends to the whole domain and that is continuous and locally polynomial, of the degree of the interpolants.

$$U_h = \sum_{i=1}^{n_n} U_i\, N_i = \sum_{i=1}^{n_n} U_i \sum_{e=1}^{n_e} N_i^e \tag{2.2}$$

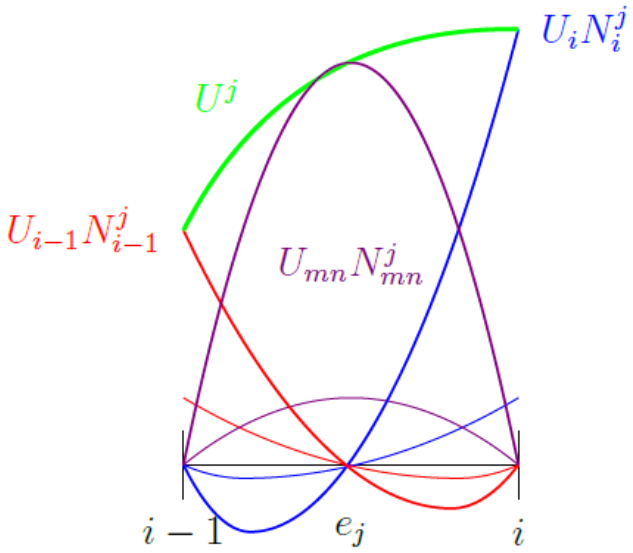

Figure 2.2 Interpolation of the nodal potential in a 1D case for a 2nd degree. We can notice that the number of the interpolants to be considered to do the weighted sum is equal to the number of nodes on the element.

2.2 Weighted Residual Approach

In the Weighted residual approach, is defined an equivalence between the PDEs problem and another problem that is easier to solve. The problem is reconducted to the solution of:

$$\int_{\Omega} w * L(U) dV = 0 \tag{2.3}$$

For all the test functions $\boldsymbol{w}$ that can be defined in the domain $\boldsymbol{\Omega}$. This means that the same funtion U is solution both of the integral problem than the PDEs equation (usually in the electromagnetic problems the function is the magnetic potential). This correlation could be demonstrable in both the sense. To solve the weighted residual, the exact resolution of the weighted residual is no longer looked for but it is introduced a residual to be minimized. Therefore, to cover the entire space of functions i should try every kind of function and verify if the results is null and this requires an infinite time. Hence, I restrict the solution to an approximate solution of the kind:

$$U_h = \sum_{j=1}^{n_n} U_j N_j$$

This is a piecewise (linear or quadratic) function. This means that the domain, containing the solution of the problem, will be smaller than the one containing the exact solution of the more general problem. At this point, to solve the problem and obtain a unique solution it is necessary to introduce a choice: the Galerkin Choice.

$$w_i = N_i \ , i\epsilon[1, n_n] \tag{2.4}$$

This is a clever choice because i obtain a quadratic and symmetric set of equations. Finally, the problem becomes:

$$\int_\Omega N_i * L(U_h) dV = 0 \ \forall\, 1 = 1,2, \dots, n_n \tag{2.5}$$

If we characterize this formulation for the 2D axial symmetric magneto quasi static problem, the residual is:

$$L(U_h) = L(A_{\varphi h}) = \nabla \cdot \nu \nabla \sum_{j=1}^{n_n} A_{\varphi j} N_j - \sigma \frac{\partial}{\partial t} \sum_{j=1}^{n_n} A_{\varphi j} - J_{s\varphi} = 0 \tag{2.6}$$

The integral form becomes:

$$\int_\Omega N_i \left(\nabla \cdot \nu \nabla \sum_{j=1}^{n_n} A_{\varphi j} N_j - \sigma \frac{\partial}{\partial t} \sum_{j=1}^{n_n} A_{\varphi j} - J_{s\varphi} \right) dV = 0 \tag{2.7}$$

Observing that the function that might be integrated, can't be a continuous function, it is necessary to apply the multidimensional form of integration by parts, known as Grenn's law:

$$\int_a^b f * g' dx = f * g(b) - f * g(a) - \int_a^b g * f' dx$$

In our particular case f=N_i and $g' = \nabla \cdot \nu \nabla \sum_{j=1}^{n_n} A_{\varphi j} N_j - \sigma \frac{\partial}{\partial t} \sum_{j=1}^{n_n} A_{\varphi j} - J_{s\varphi}$

This means that the previous integration (defined as I) can be split in two different terms:

$$I = -\int_\Omega N_i \left(\nu \frac{\partial A_{\varphi h}}{\partial t} - J_{s\varphi} \right) dV - \int_\Omega \nabla N_i \cdot \nu \nabla A_{\varphi h} \, dV + \oint_{\partial\Omega} N_i \, \nu \nabla A_{\varphi h} \, n \, dS = 0 \tag{2.8}$$

Green's law helps to solve this extremely complex integration and obtain a simpler form. The last term of the equation is the Hard form of the magneto quasi static problem and it is computed on the boundary of the domain. The second term of the

equation is called Weak Form and it must be a continuous function and derivable one time, while the other terms is required a regularity of class C^2 (that is the origin of the attribute "weak").

To analyze better this equation and understand properly the meaning of each term let us rewrite the equation underlining the sources of the model and the time dependent term.

$$-\int_{\Omega} \nabla N_i \cdot \nu \nabla A_{\varphi h}\, dV + \oint_{\partial\Omega} N_i\, \nu \nabla A_{\varphi h}\, n\, dS = \int_{\Omega} N_i\, \nu \frac{\partial A_{\varphi h}}{\partial t} - \int_{\Omega} N_i\, J_{s\varphi}\, dV \qquad (2.9)$$

Developing the integral, we obtain at the first term.

$$\int_{\Omega} \nabla N_i \cdot \nu \nabla A_{\varphi h}\, dV = \int_{\Omega} \nabla N_i \cdot \nu \nabla \left(\sum_{j=1}^{n_n} A_{\varphi j} N_j \right) dV = \sum_{j=1}^{n_n} \left(\int_{\Omega} \nabla N_i \cdot \nu \nabla N_j\, dV \right) A_{\varphi j} = \sum_{j=1}^{n_n} k_{ij} A_{\varphi j} \qquad (2.10)$$

Where the coefficient k_{ij} the stiffness matrix.

$$k_{ij} = \int_{\Omega} \nabla N_i \cdot \nu \nabla N_j\, dV = \sum_{e=1}^{n_e} \int_{\Delta e} \nabla N_i \cdot \nu \nabla N_j\, dV \qquad (2.11)$$

With Δe the general element of the mesh (triangular or quadrilateral in an axial symmetric geometry). The second term of the equation is:

$$\oint_{\partial\Omega} N_i\, \nu \nabla A_{\varphi h}\, n\, dS \qquad (2.12)$$

It represents the B−normal conservation condition. It is possible to view that internal nodes don't give contribution to the integral. Assuming we can isolate each element of the mesh, then the integral computed on the line, that divides two elements, becomes:

$$\int_A^B N_i^1\ \nu^1 \frac{\partial A_{\varphi h}^1}{\partial n^1} dP + \int_A^B N_i^2\, \nu^2 \frac{\partial A_{\varphi h}^2}{\partial n^2} dP \qquad (2.13)$$

Because on the boundary of each element, the shape function must be equal than $N_i^1 = N_i^2$ on the boundary $\overrightarrow{AB}$ as consequence of the conservation of the normal component of the induction magnetic field. Instead, when the element is on the boundary it can apply only a boundary condition. Therefore, with Dirichlet is imposed the value of the node, the homogeneous Neumann condition forces the derivate along the normal component to be null; if it is imposed a non homogeneous Neumann condition the value of the derivate is not zero but it is equal to a value set into the known term.

Fourier's Equation

If we apply the Weighted residual approach to solve Fourier's thermal equation:

$$-\nabla \cdot \lambda \nabla T + \rho C_p \frac{\partial T}{\partial t} = q \qquad (2.14)$$

where ρC_p is the thermal capacity and q is the heating source of the model; remembering that the stiffness matrix and the know term matrix are:

$$k_{ij} = \int_\Omega \boldsymbol{\lambda}\boldsymbol{\nabla}N_i \cdot \boldsymbol{\nabla}N_j dV$$
$$b_i = \int_\Omega N_i p dV \tag{2.15}$$

integrating by parts, applying Galerkin's method, as done for the electromagnetic method in the previous paragraph, the system to solve becomes:

$$\int_\Omega N_i\, \rho C_p \frac{\partial T}{\partial t} dV = \int_\Omega N_i\, \rho C_p \frac{\partial \sum_{j=1}^{n_n} N_j T_j}{\partial t} dV = \sum_{j=1}^{n_n} \left(\int_\Omega N_i N_j\, \rho C_p\, dV \right) \frac{\partial T_j}{\partial t} \tag{2.16}$$

where is notable the mass matrix

$$M_{ij} = \int_\Omega N_i N_j\, \rho C_p\, dV$$

rewriting the equation with a matrix formulation:

$$[K] * [T] + [B] * [T] + [M] \frac{\partial}{\partial t}[T] = [M_s] * [q] + [B] * [T^0] \tag{2.17}$$

This is a differential algebraic equation that can be solved using the general theta–method, in order to evaluate the time solution for the next time step.

$$([M] + \Delta t\theta[K_{n+1}] + [B_{n+1}]) \cdot [X_{n+1}] = ([M] + \Delta t(\theta - 1)[K_n + B_n]) \cdot [X_n] + \Delta t(\theta[S_{n+1} + (1 - \theta)[S_n]) \tag{2.18}$$

2.5 Newton-Raphson

To solve a general non–linear equation, the iterative method of Newton–Raphson is utilized. This iterative scheme, that when converges do it quadratically, allows to obtain a solution of the problem $f(x) = 0$ by making a linearization of the nonlinear function. This means that, instead of the initial function *f,* we want to find the intersection with the x–axis of an equivalent linearized function $L(x)=0$.
This method starts from an initial point, supposed reasonably close to the true root, then the function is approximated by its tangent line and it is found its x–intercept. This second point will be a better approximation to the function's root than the original one. Typically the Newton–Raphson scheme is synthesized with this formulation: if $f:[a,b] \Rightarrow \mathbb{R}$ is a differentiable function defined in the interval and supposing we have an initial point x_n, then the better approximation is given by

$$x_{n+1} = x_n - \frac{f(x_n)}{f'(x_n)} \tag{2.19}$$

Where *f'* denotes the derivate of the function *f.*
Now let us apply this iterative scheme to the Fourier's thermal equation supposed non–linear.
T^k is the estimate of the initial temperature and T^{k+1} is the new estimate temperature. It is possible to define the gap between the two temperatures as:

$$T^{k+1} = T^k + \delta T$$

$$\lambda(T^{k+1}) = \lambda(T^k) + \lambda'(T^k)\delta T$$

Finally, the partial differential equation is:

$$-\boldsymbol{\nabla} \cdot \lambda(T)\boldsymbol{\nabla}\mathrm{T} = 0 \tag{2.20}$$

The PDE at the following step is:

$$-\boldsymbol{\nabla} \cdot \lambda(T^{k+1})\boldsymbol{\nabla}\mathrm{T^{k+1}} = -\boldsymbol{\nabla} \cdot (\lambda(T^k) + \mathrm{k'(T^k)}\delta T)\,\boldsymbol{\nabla}(\mathrm{T^k} + \delta\mathrm{T}) = 0 \tag{2.21}$$

Then, it is possible to neglect higher order terms and get the PDE that is again solvable with a finite elements approach.

$$-\boldsymbol{\nabla} \cdot \lambda(T^k)\boldsymbol{\nabla}\delta T - \boldsymbol{\nabla} \cdot \lambda'(T^k)\delta T\boldsymbol{\nabla}\mathrm{T^k} = \boldsymbol{\nabla} \cdot \lambda(T^k)\boldsymbol{\nabla}\,\mathrm{T^k} \tag{2.22}$$

Successively we use Green's method to integrate and after imposing the boundary condition we obtain the following matrix writing:

$$[\lambda + N + B] * [\,\delta T] = -[\lambda] * [T^k] - [B] * [T^k] + [b] \tag{2.23}$$

where [B] is the boundary condition matrix, instead [N] is a not symmetric matrix defined by elements n_{ij}.

The same approach can be used for magnetic fields, even if the non−linear behavior of magnetic fields is more complex than the thermal one.
It is possible to write the induction magnetic field as a function of the magnetic field $|\boldsymbol{B}| = function(|\boldsymbol{H}|)$. This means that is possible to define a magnetic permeability for each value of the magnetic field.

$$\frac{1}{\mu} = \nu(|B|) = \nu\left(\boldsymbol{\nabla}\times A_\varphi\right) \tag{2.24}$$

It is possible to define the partial derivate with induction field as: $\frac{\partial \nu}{\partial B} \approx \frac{\Delta \nu}{\Delta B}$ but typically, for an electromagnetic problem, the unknown is not B but the magnetic potential. Therefore

$$\frac{\partial \nu}{\partial A_\varphi} = \frac{\partial \nu}{\partial B} * \frac{\partial B}{\partial A_\varphi} \tag{2.25}$$

and this problem is resolvable because the first term $\frac{\partial \nu}{\partial B}$ is usually known through the magnetization curve, instead the second term $\frac{\partial B}{\partial A_\varphi}$ can be computed through shape functions.

Chapter 3

Material Properties of steel AISI-4340

In this chapter, the material parameters of steel AISI−4340 are introduced. This is particularly important, not only because the material parameters are the relative coefficients for the PDEs equation explicated in the previous chapters, but also because the material parameters have all non−linear properties.
Due to the fact that induction heating treatment is based on electromagnetic and thermal approach, the parameters concerning these two aspects are going to be underlined.

AISI−4340 is a heat treatable alloy steel, containing little quantities of nickel, chromium and molybdenum. It is known for its toughness and capability of developing high strength in the heat−treated condition while retaining good fatigue strength. Typical applications are for structural use, such as aircraft landing gear, power transmission gears and shafts and other structural parts.

Element	%
Carbon	0.38-0.43
Chromium	0.7-0.9
Manganese	0.6-0.8
Molybdenum	1.65-2
Nickel	1.62-2
Phosphorus	0.035 max
Silicon	0.15-0.3
Sulphur	0.04 max
Iron	Balance

Table 3.1 Composition of steel alloy AISI−4340

3.1 Thermal properties

The physical properties of steel are first of all a function of its chemical composition: although carbon content and alloying elements are responsible for mechanical properties, in some case they could affect its thermal behaviour. Moreover, prior metallurgical structure is found to have big influence on material' s response to heat treatment. In the particular case of induction heating there is the necessity of suitable formulation for material properties, because they drastically change in function of temperature T. The coefficients that are necessary to describe and solve the thermal properties are:

Property	Unit of measure	Symbol
Thermal Conductivity	$\left[\frac{W}{mK}\right]$	$\boldsymbol{\lambda}$
Volumetric Heat Capacity	$\left[\frac{J}{m^3K}\right]$	$\mathbf{c_p}$
Density	$\left[\frac{kg}{m^3}\right]$	$\boldsymbol{\gamma}$

Table 3.2 Main thermal parameters for induction heating process

Thermal Conductivity

Thermal conductivity is a thermo−physical property, which expresses the quantity of heat that a specific material can transfer through a unit surface area in a unit of time when exists a gradient of temperature between two different point. In other words, it defines the heat flow transmitted by conduction in the material in function of time. Steel has rather high thermal conductivity, so heat generated in a thin region in the surface, by induction heating, is rapidly transferred to the cold hearth of the piece. In literature, it is possible to find a suitable formulation for thermal conductivity, that expresses it as a function of temperature T.

$$\lambda(T) = C + (\lambda_b - \lambda_a) * \left(1 - e^{\frac{T-T_b}{\tau}}\right) \tag{3.1}$$

Where T_b [° C] is the reference temperature, λ_a is the asymptotic steady state conductivity value (i.e. the limit value that thermal conductivity assumes when the temperature gradient becomes extremely big). λ_b is the residual conductivity value at the reference temperature (i.e. it is the value that a material shows if does not exist a temperature gradient). The last parameter is τ [°C] that is a temperature constant.

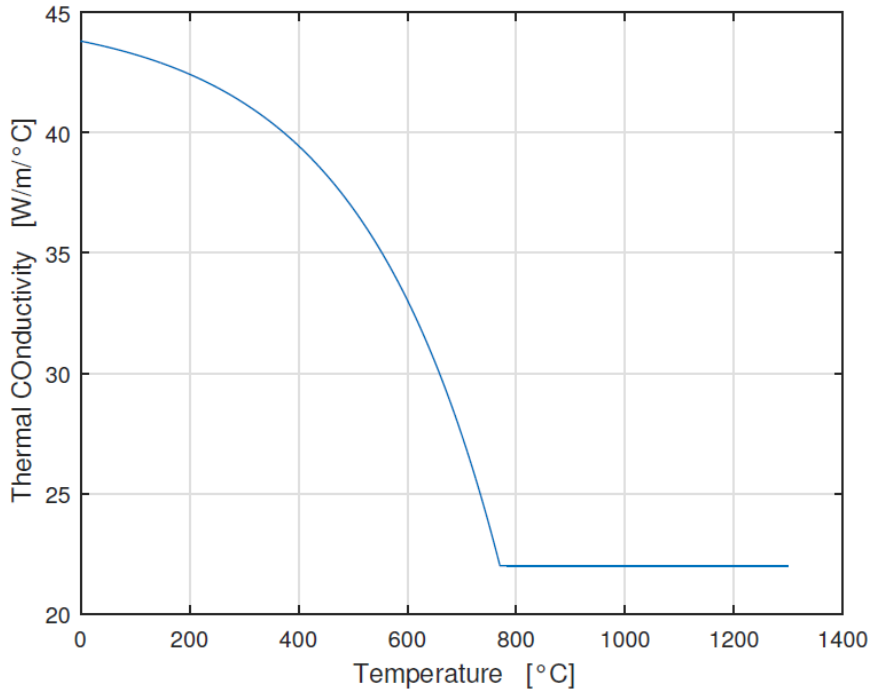

Figure 3.1 Thermal Conductivity in function of temperature $\boldsymbol{\lambda(T)}$.

Symbol	Value	Unit
$\boldsymbol{\lambda_a}$	22	$\frac{W}{mK}$
$\boldsymbol{\lambda_b}$	45	$\frac{W}{mK}$
$\mathbf{T_b}$	770	°C
$\boldsymbol{\tau}$	260	°C

Table 3.3 Parameters of thermal conductivity's exponential formulation.

Heat Capacity

The heat capacity of a material is the heat quantity necessary to raise its temperature by one Kelvin degree. It makes possible to evaluate the amount of energy exchanged by a body during a process characterized by a temperature variation in time. The specific heat capacity per unit volume is particularly important as it allows to take into account the changes of energy characterizing the phase transition. It is expressed by the superimposition of an exponential and a Gaussian function (centred in the transformation point), that are both function of temperature.

$$\gamma C_p(T) = \gamma C_{Pi} + (\gamma C_{P0} - \gamma C_{Pi}) * e^{-\frac{T}{\tau}} + E * G(T) \tag{3.2}$$

$$G(T) = \frac{1}{\sigma_{dev}\sqrt{2\pi}} * e^{-\frac{1}{2}\left(\frac{T-T_{ph}}{\sigma_{dev}}\right)^2} \tag{3.3}$$

Where the first term γ [kg/m^3] is the material density, γC_{Pi} is the heat "asymptotic" capacity of the material, γC_{P0} is the initial heat capacity. E[J/m^3] is the energy necessary to obtain the phase transition. σ_{dev} [°C] is the experimentally obtained Gaussian standard deviation, T_{ph} [°C] is the phase transition temperature. It is relevant to subline that this value is function of heating rate and might vary for different heat treatment that use the same material. Finally, τ [°C] is the temperature constant of the exponential function that fixes the temperature interval of the Gaussian spike.

Symbol	Value	Unit
γ	7800	$\left[\frac{kg}{m^3}\right]$
γC_{P0}	$3*10^6$	$\left[\frac{J}{m^3K}\right]$
γC_{Pi}	$6*10^6$	$\left[\frac{J}{m^3K}\right]$
E	$125*10^7$	$\left[\frac{J}{m^3}\right]$
σ_{dev}	50	[°C]
τ	300	[°C]
T_{ph}	870	[°C]

Table 3.4 Parameters of heat capacity's exponential–Gaussian formulation of steel AISI–4340.

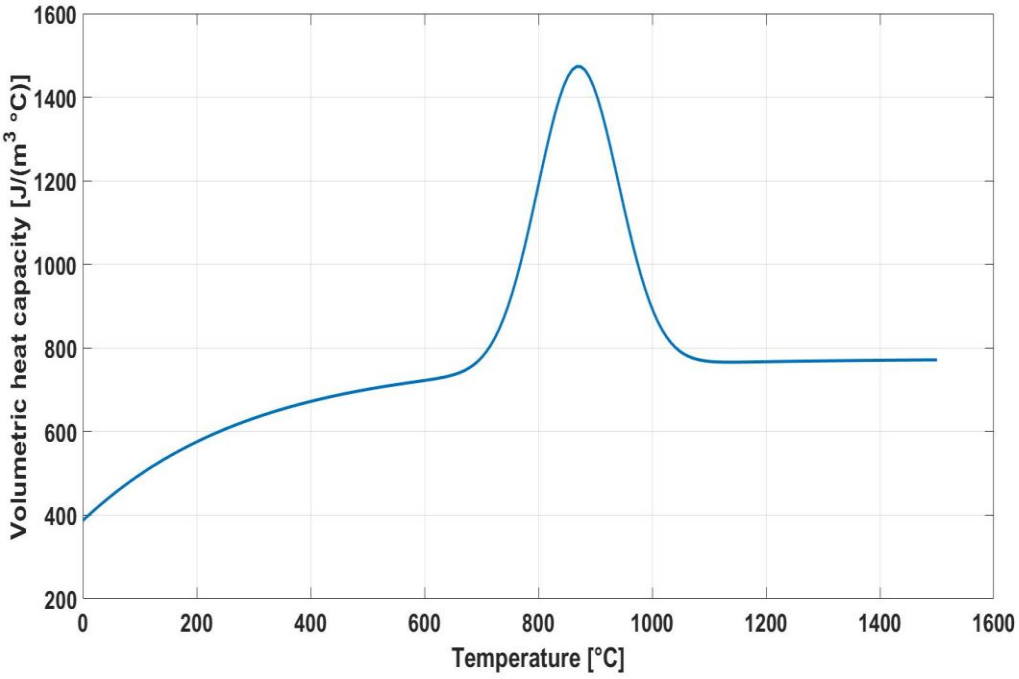

Figure 3.2 Heat Capacity in function of temperature $\gamma C_p(T)$.

3.2 Electrical properties

Electrical Resistivity

Common feature of all metals, the resistivity increases linearly in function of temperature. There is a flexion in proximity of A_1 temperature, where the slope decreases and consequently the growing rate decreases too. Generally, it could be described by an analytic linear relation which does not take into account the saturation in proximity of A_1. In the simulations, the resistivity had been interpolated by a first order piecewise line.

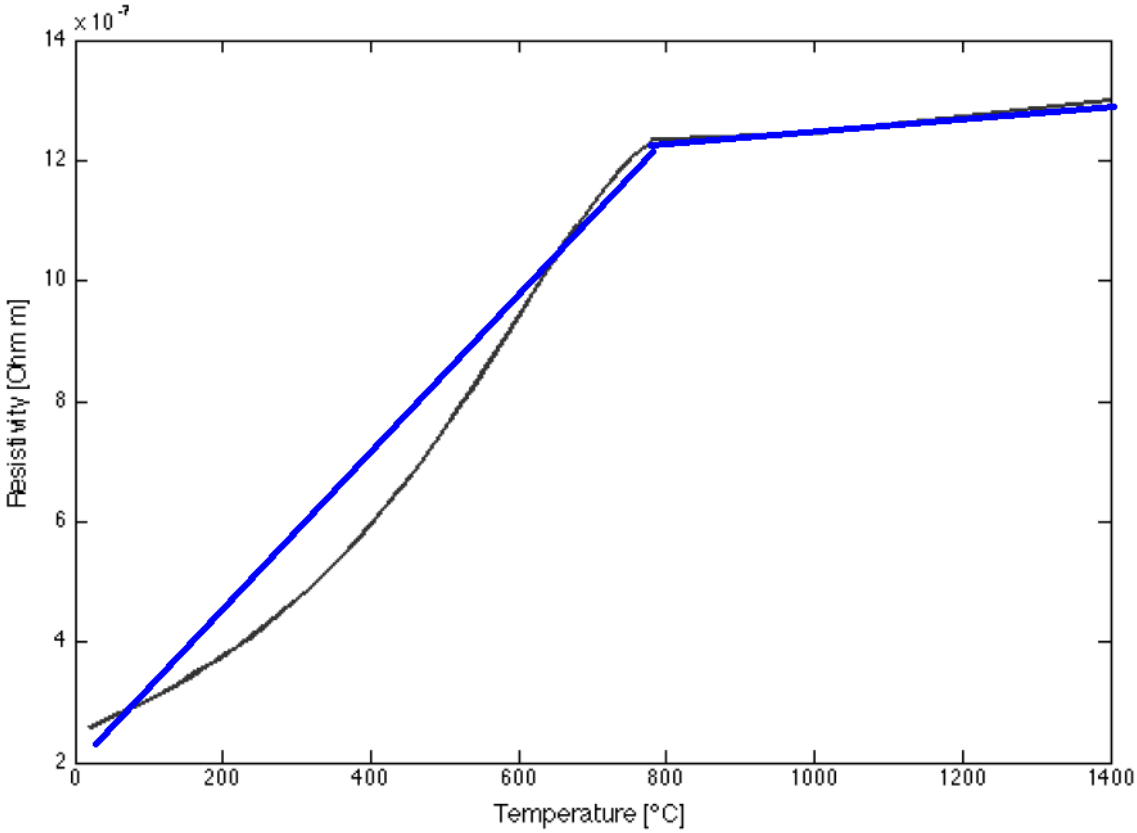

Figure 3.3 Electric resistivity in function of temperature $\boldsymbol{\rho(T)}$. The black line is the experimental one while the blue one is the linear interpolant.

Magnetic Permeability

Between all the material parameters the most challenging is the magnetic permeability. As a matter of facts, it describes the complex behaviour that the magnetic induction field B manifests with the increasing of magnetic field H. However, **μ** not only changes in function of the magnetic field, but also in function of

temperature T: after Curie's temperature, the material loses its ferromagnetic behaviour and becomes a paramagnetic material.
An accurate simulation must consider saturation: a strong non−linear behaviour is characteristic for ferromagnetic materials, such as iron, nickel, cobalt and their alloys. Saturation is most clearly seen in the normalized magnetization curve, usually named *BHcurve* . It underlines that induction magnetic fields increases according to magnetic field but reaches a maximum value asymptotically. This behaviour can be explained physically with magnetic polarization: when all the magnetic dipoles of the atoms are aligned with the external magnetic field we reach the asymptotic level (i.e. the saturation level) that is indicated with B_s [T]. the relation between the magnetizing field H and the induction field B is expressed as a function product of the magnetic permeability:

$$\boldsymbol{B} = \mu(|\boldsymbol{H}|) * \boldsymbol{H} \tag{3.4}$$

Where the magnetic permeability is the product of relative permeability μ_r and the constant vacuum permeability μ_0 . Due to saturation, it is easy to understand that the magnetic permeability is not constant: for small magnetic field, it is constant because BHcurve has a linear plot, then there is a second part where there is the knee and the saturation. In literature exists an analytical function that describes with a good accuracy that behaviour:

$$\boldsymbol{B}(\boldsymbol{H}) = \mu_0 \boldsymbol{H} + \frac{2B_s}{\pi} \arctan\left(\frac{\pi(\mu_{r0} - 1)|\boldsymbol{H}|}{2B_s}\right) \tag{3.5}$$

In this expression μ_{r0} is the initial relative permeability.

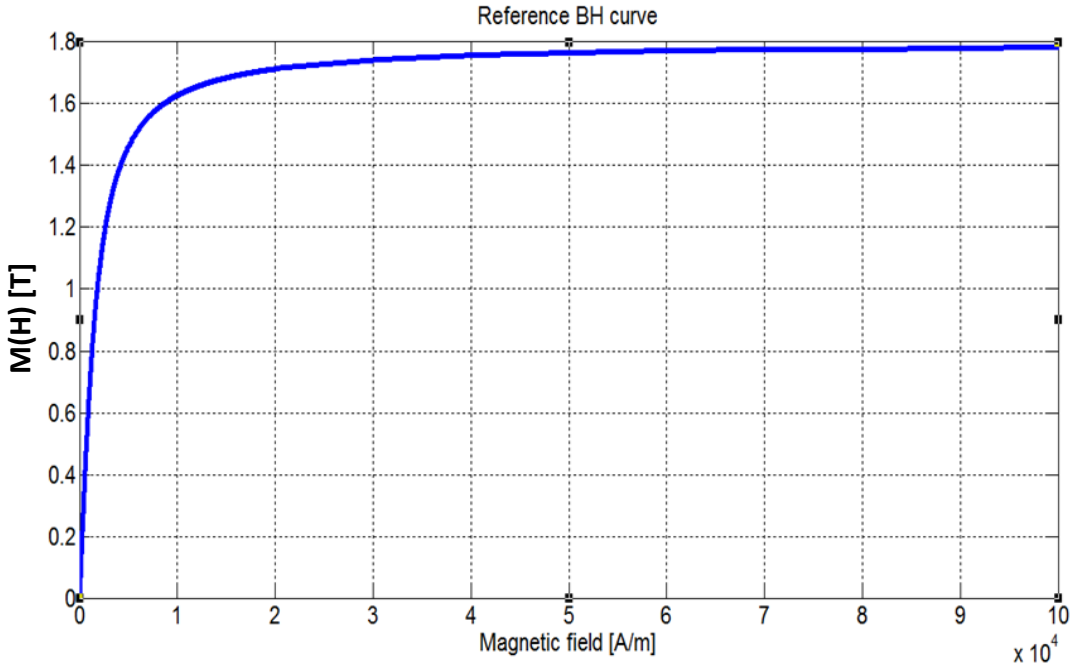

Figure 3.4 Behaviour of magnetization field [T] in function of the magnetic field [A/m]. It is possible to notice the saturation knee and the asymptotic saturation level

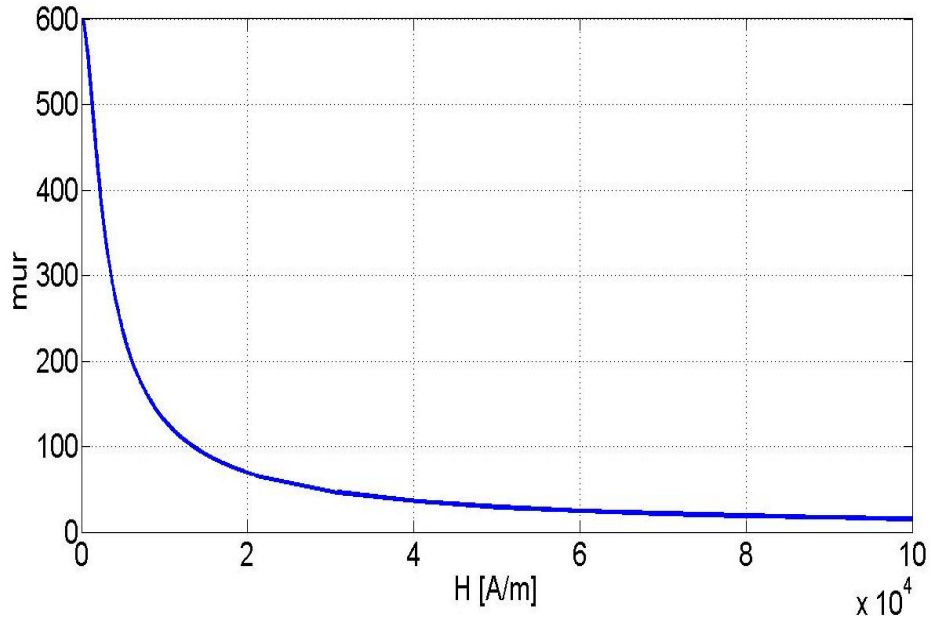

Figure 3.5 Relative magnetic permeability in function of the magnetic field H.

As previously mentioned, the other phenomena that must be considered for the nonlinear behaviour of magnetic permeability is the transition phase that occurs in steels at the Curie Temperature. Therefore, it is possible to modify the analytic expression to describe the full behaviour of the material. Operating in this way we can plot a three−dimensional curve that summarize the magnetic saturation and the phase transition.

$$\boldsymbol{B}(\boldsymbol{H},\boldsymbol{T}) = \mu_0 \boldsymbol{H} + \frac{2B_s}{\pi}\arctan\left(\frac{\pi(\mu_{r0}-1)|\boldsymbol{H}|}{2B_s}\right) * \left(1 - e^{\frac{T-T_c}{C}}\right) \tag{3.6}$$

Symbol	Value	Unit
$\boldsymbol{\mu_0}$	$4\pi*10^{-7}$	$\left[\frac{H}{m}\right]$
$\boldsymbol{B_s}$	1.8	$[T]$
$\boldsymbol{\mu_{r0}}$	600	$[-]$
$\mathbf{T_c}$	780	$[°C]$
$\boldsymbol{C}$	40	[°C]

Table 3.6 Parameters of magnetic induction field in function of temperature and magnetic field

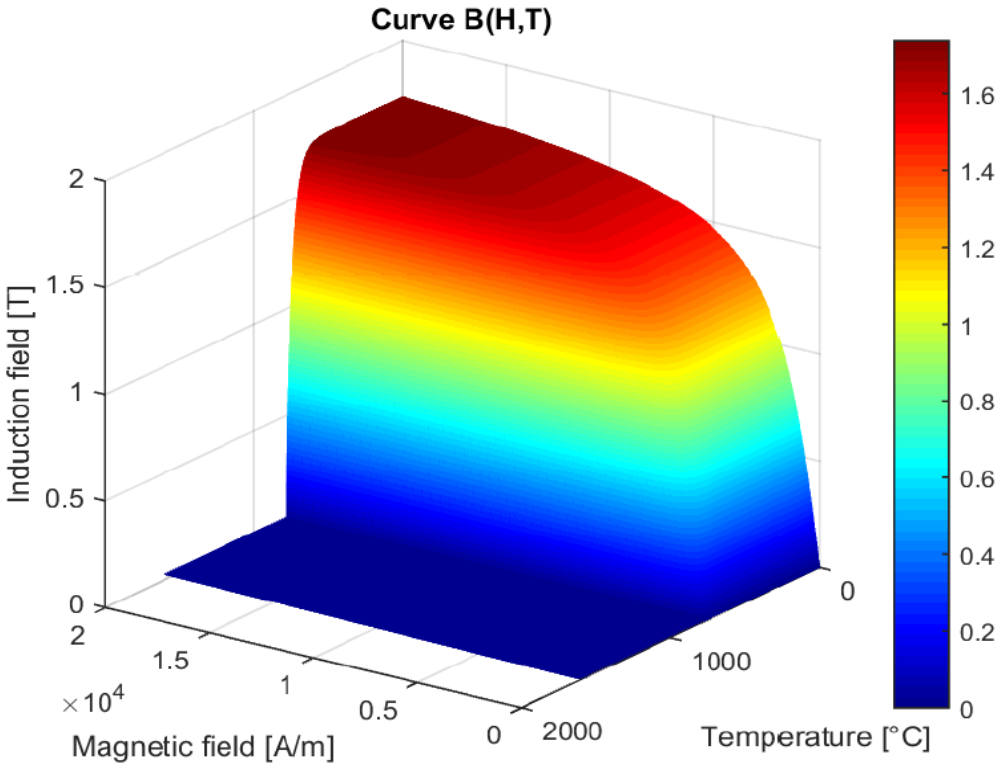

Figure 3.7 3D magnetic flux plotted in function of temperature and magnetic field .

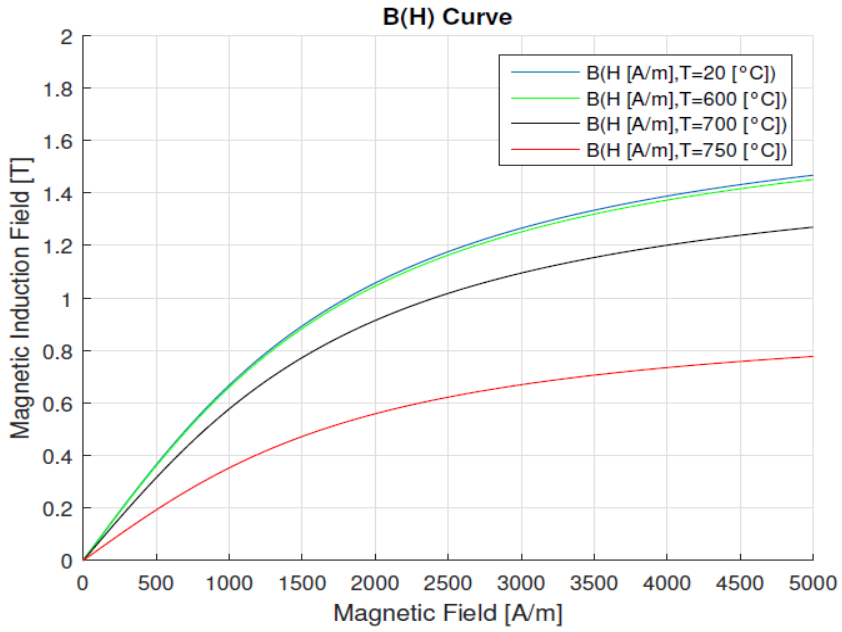

Figure 3.6 Magnetic flux plotted in function of temperature and magnetic field for a particular steel alloy. With different BHcurves at several temperatures we want to underline the progressive transition from a ferromagnetic into a paramagnetic medium.

Penetration Depth

As one may know from the basis of electricity, when a direct current (DC) flows through a conductor that stands alone, the current distribution within the conductor's cross section is uniform. However, when an AC flows through the same conductor, the current distribution is not uniform. The maximum value of the current density will always be located in the surface of the conductor; current density will decrease from the surface of the conductor toward its centre. This phenomenon on non-uniform current distribution within the conductor's cross section is called skin effect. This is one of the major factors that cause the concentration of eddy current in the surface layer (skin) of the workpiece and it is used in surface induction hardening. As a matter of facts, due to the circumferential nature of eddy current induced in the workpiece, there is no current flow in the centre.
Because of the skin effect, approximately 86,5% of the power will be concentrated in a surface layer of the conductor. This layer is called penetration depth $\boldsymbol{\delta}$ [m].
The degree of skin effect depends on the frequency and electromagnetic material properties of the material, introduced in the previous paragraphs (i.e. electrical resistivity and relative magnetic permeability).
There will be a pronounced skin effect when a high frequency is applied or when the radius of the workpiece is relatively large.
From Bessel's functions, an analytic formulation for the penetration depth and for the current density along the radius of the sample is obtained.

$$\delta = \sqrt{\frac{\rho}{\pi\, \mu_0\, \mu_r\, f}} \tag{3.7}$$

$$I_R = I_0 e^{-\frac{y}{\delta}} \tag{3.8}$$

In these expressions, different parameters appear: ρ is the electrical resistivity of steel [Ω m], μ_r is the relative magnetic permeability, and f is the frequency [Hz]. In the second expression I_R is the current density [A/m^2]at distance R from the surface, I_0 is the current density at the workpiece surface and lastly y is the distance from the surface toward the core.

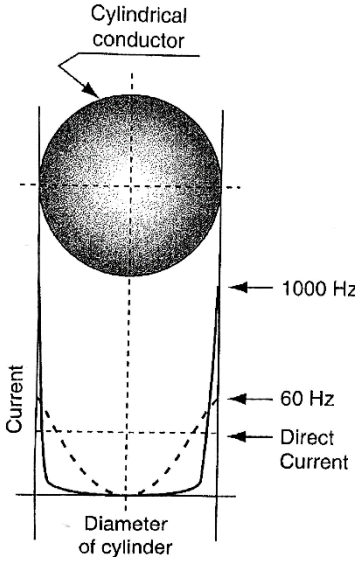

Figure 3.8 Qualitative current distribution in function of frequency.
Totten G., Steel Heat Treatment, metallurgy and technologies" (2006, pag.308)

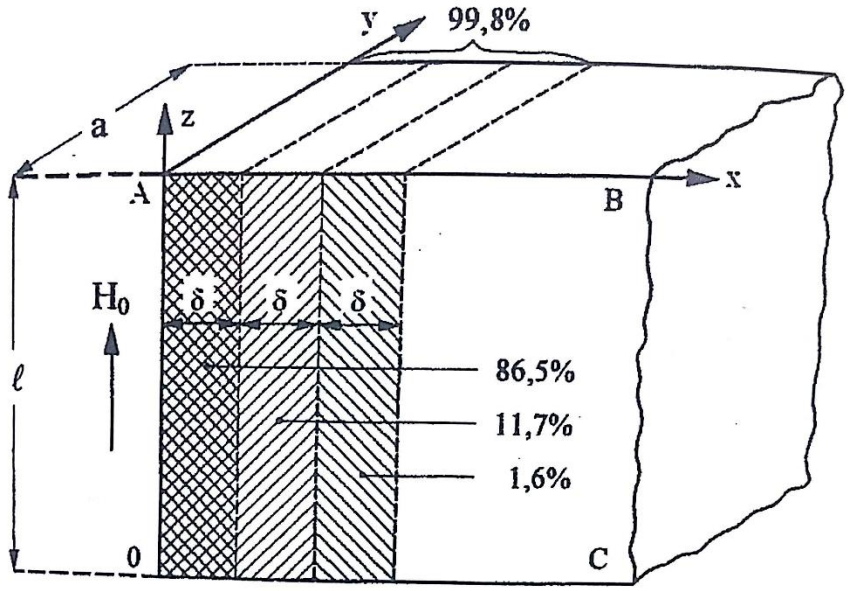

Figure 3.9 Distribution of current densities in an infinite semi−plane. In the figure is underlined that almost the 99% percent of the total current and consecutively power induced is concentrated in the first three penetration depths.
S. Lupi, "Appunti di Elettrotermia," (2006, pag. 249)

3.3 Characterization of the magnetic hysteresis

The parameters introduced in the previous paragraphs neglect a phenomenon characterizing ferromagnetic materials: the hysteresis loop (in Greek *υστέρεσις* =delay). Ferromagnetic materials are characterized by a shift between the magnetic field intensity H and the magnetic induction field B. Physically we can explain this delay due to the time that magnetic domain inside the medium need to align with the magnetic field.
Therefore, when the source of the magnetic field is removed, the whole domains do not come back in a random position but some still stand unchanged so they turn the material in a permanent magnet with a saturation remanence.
If we want to neutralize this magnetism we must apply a magnetic field in the opposite direction. Progressing in this process, it can observed that the working point describes a closed pattern that is named hysteresis loop.
If an alternating magnetic field is applied, we will find the same number of hysteresis loops as the frequency with whom we modify the magnetic field. Physically the area included between the branches is energy lost in heat: it can be imagined that, at atomic level, the orbitals of the magnetic dipole generate a "friction" with orbitals of other dipole while they are changing orientation direction.

Due to the phase shift in mediums with hysteresis, we can describe the relation between the magnetization field and the magnetic field only with a complex parameter: the complex magnetic permeability.

$$\boldsymbol{B}(t) = \bar{\boldsymbol{\mu}}\,\boldsymbol{H}(t) \;\rightarrow\; \boldsymbol{B}(t) = \mu_0 H(t) + \bar{\boldsymbol{\mu}}_{rel}\boldsymbol{H}(t) \;\rightarrow\; \boldsymbol{B}(t) = \mu_0\boldsymbol{H}(t) + \boldsymbol{M}(t) \qquad (3.9)$$

In this last expression, the relation between the magnetization field ($\boldsymbol{M}$ [T]) and the induction magnetic field is highlighted. They differentiate only by the contribution of the vacuum permeability multiply for the magnetic field. Moreover, we can notice that the complex behaviour that describes, not only the saturation, but also the hysteresis, is comprehended in the relative magnetic permeability.

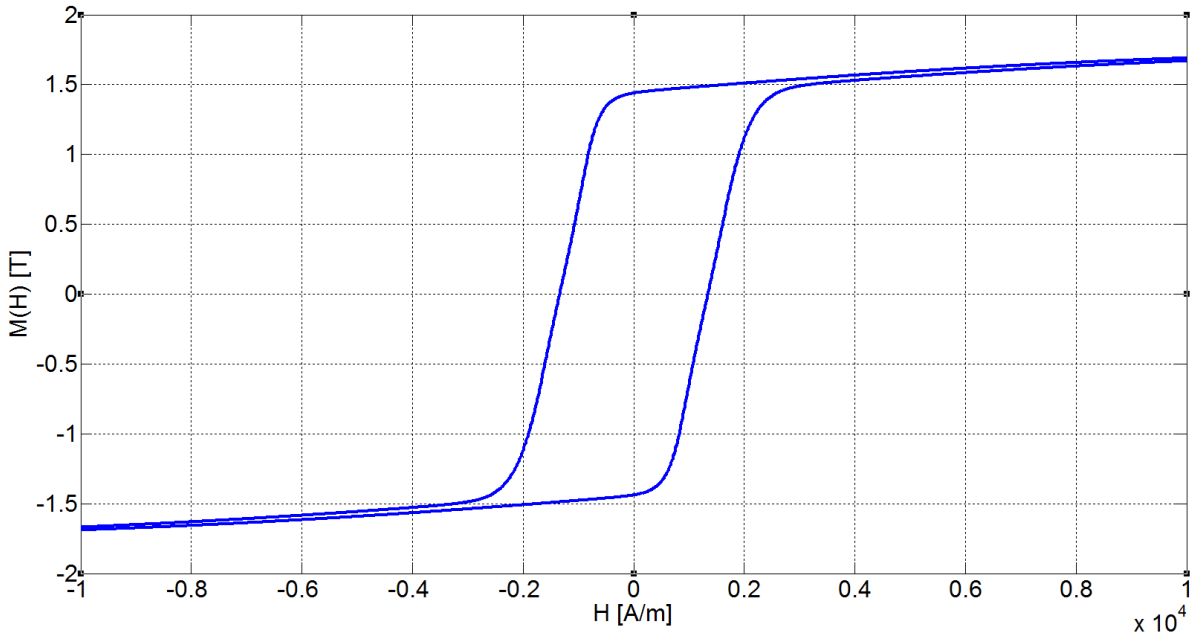

Figure 3.10 Hysteresis loop of AISI−4340, collected by *Polytechnique de Montréal*.

The magnetic parameters are the ones that mostly influence the hardening process because they determine the distribution of currents. Consequently, the smallest variation on these parameters can generate a remarkable variation in the final hardening process. In order to obtain the best expression possible for hysteresis and consequently for the normalized BHcurve, a characterization of steel AISI−4340 was made in collaboration with *Polytechnique de Montréal*.
Hysteresis loops were measured with a dynamic approach, in which the driving magnetic field is constantly changing. A low frequency (e.g. 0.1 to 5 [Hz]) is selected to obtain quasi−static conditions. The importance of static or quasi−static measurements is clearly stated in the literature. This allows for good magnetic measurements, as this range of frequency is immune to the screening effect of eddy currents (at the macroscopic level). In other words, at low enough frequencies, the magnetic field penetrates deeply inside the sample, so the measured quantities are representative of the whole volume.

The measurements were sampled in a toroidal shape of normalized steel AISI−4340 with external diameter of 50 [*mm*] and internal diameter of 40 [*mm*]. The experimental setup is based on the two−winding approach and adapted for high temperature measurements. In this approach, an excitation winding creates the magnetic field while a search coil measures variations in the resulting magnetic flux. In our case, it was essential to speed up the process because changes in steel microstructure become important when the sample is maintained above 400 [°C] for an hour or more. A primary winding was made to collect the measurements and a second one to heat the steel. Between every layer was placed a ceramic insulating (the only one able to insulate above temperature of 700 [°C]).

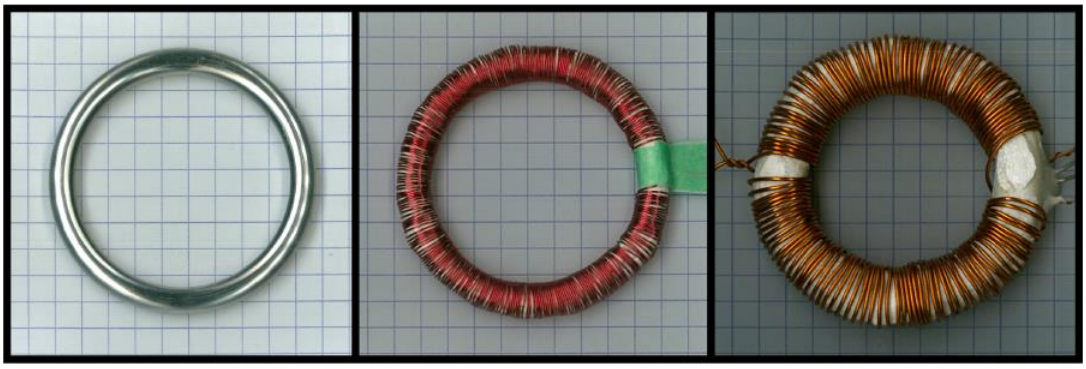

Figure 3.11 Sample of steel AISI−4340 used for the characterization of magnetic properties. a) steel toroid; b) sample with the first layer of ceramic insulating and the measurement winding; c) sample with the second ceramic layer and the induction heating winding.

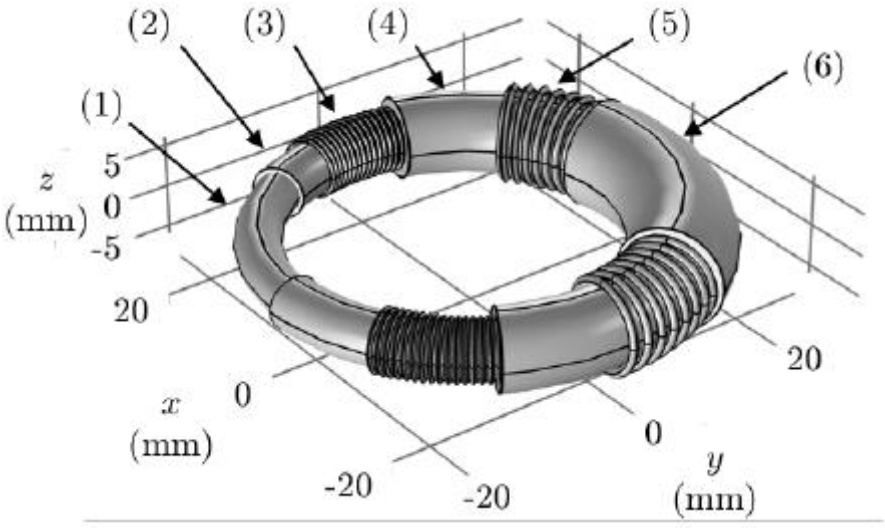

Figure 3.12 Section of the steel sample where are visible all the layers. 1) sample; 3) measurement coil; 5) excitation coil; 2),4),6) insulating ceramic.

In the excitation coil is applied a differential of potential of 60 [V] that makes flow 30 [A] of current at a frequency of 3[kHz]. In this way, the sample is heated and it is possible to characterize the magnetic parameters in function of the temperature.

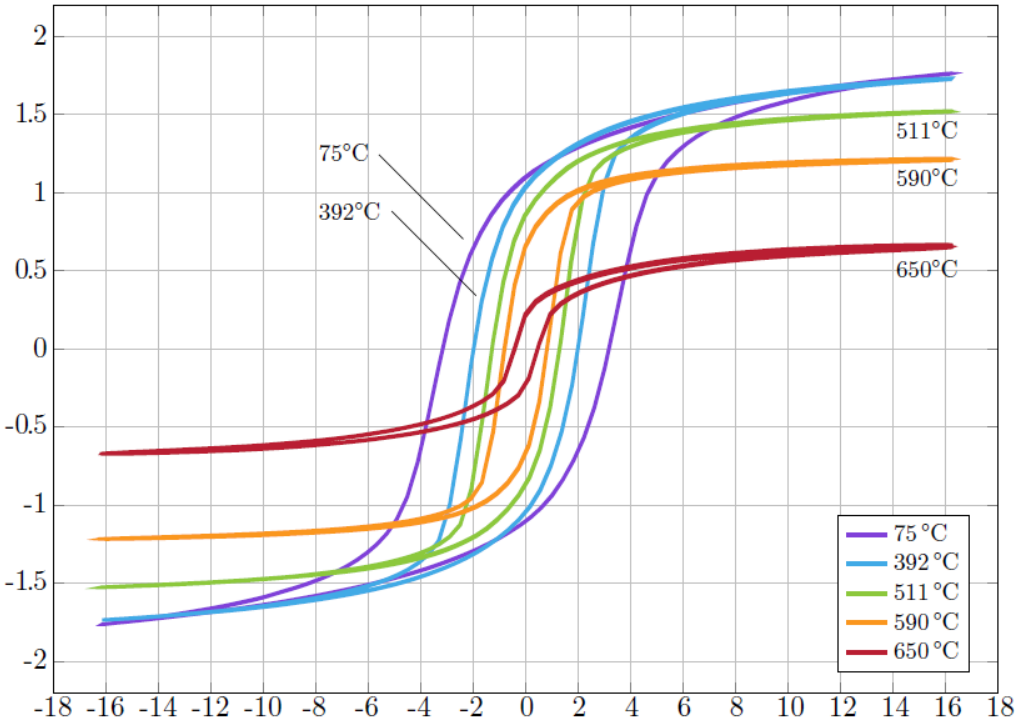

Figure 3.13 hysteresis loops in function of temperature. In the abscissa, there is the magnetic field H [kA/m] while in the ordinate axis there is the induction magnetic field B[T]. When the temperature raises the hysteresis loop decreases, in particular the maximal saturation point.

When all the measurements are collected, it is possible to build the normalized BH curve to describe the behaviour of the steel alloy AISI−4340.
The empirical interpolation of the data gives this expression:

$$B(t) = \mu_0|\boldsymbol{H}(t)| + \left(a_1 * tanh\left(\frac{|\boldsymbol{H}(t)|}{b_1}\right) + a_2 * tanh\left(\frac{|\boldsymbol{H}(t)|}{b_2}\right) + a_3 * tanh\left(\frac{|\boldsymbol{H}(t)|}{b_3}\right)\right) \quad (3.10)$$

Coefficient	Value	Unit	Coefficient	Value	Unit
$\boldsymbol{a_1}$	0,354	$[T]$	$\boldsymbol{b_1}$	$1{,}101e^4$	$[A/m]$
$\boldsymbol{a_2}$	0,970	$[T]$	$\boldsymbol{b_2}$	$5{,}405e^2$	$[A/m]$
$\boldsymbol{a_3}$	0,455	$[T]$	$\boldsymbol{b_3}$	$3{,}072e^2$	$[A/m]$

Table 3.6 Coefficients of BHcurve's experimental formulation.

Even if we managed to obtain an experimental curve, with a complex relative magnetic permeability, the analytic expression (3.6) will be preferred for the future simulations and test cases. The two BHcurves present the same saturation level, but the experimental data has a major slope near the origin and a more sharp–cornered knee. However, since the first objective of this thesis is to validate a new simulation model, is not relevant which BHcurve is used as benchmark. Moreover, the more smooth–shaped curve of the analytic expression will allow to have a smaller computational cost. The utilization of the experimental curve and the complete curve with hysteresis losses will be discussed in the last chapter of this paper.
However, we can already imply that the contribution due to hysteresis losses can be neglected compared to the losses due to eddy currents.

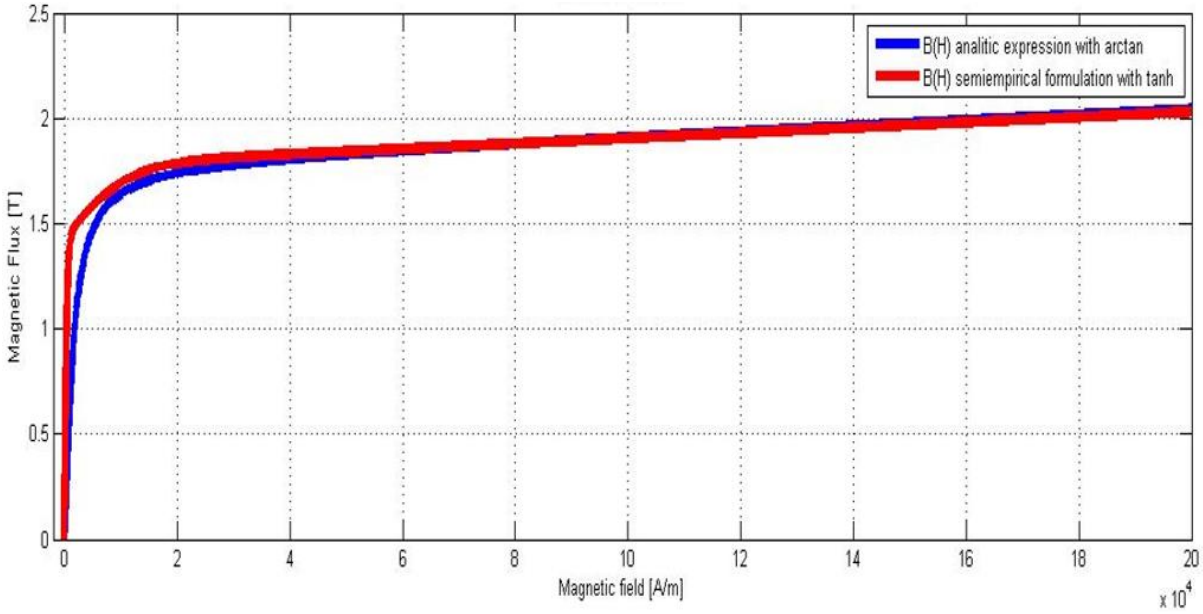

Figure 3.14 Analytic expression (blue) and experimental expression (red) of magnetic induction field B in function of magnetic field H.

Finally, it is important to mention that hysteresis loop change in function of frequency too. However, because of skin effect, it is extremely difficult to measure the real pattern of the branches. From literature, it is known that with increasing frequencies the area included between the branches uses to become smaller, because the magnetic dipole cannot follow properly the changes of the external magnetic field. Therefore, in this thesis the variation of hysteresis loop in function of frequency will not be considered.
Considering this increase of hysteresis losses indeed it is possible to neglect them in surface induction hardening processes.

Chapter 4

Power Equivalent Model

The New Power Equivalent model has been developed by Professor *Frédéric Sirois* and PhD *Maxime Tousignant* at *Polytechnique de Montréal*. In this chapter, it is briefly described how it has been realized, but the paper that deals with this new model is yet unpublished.

4.1 Definition of the Power Equivalent Model

The objective of this new equivalent model is to find a complex magnetic permeability $\bar{\boldsymbol{\mu}}(\mathrm{H})$ at the frequency w that gives back the best distribution possible for the power losses of an electromagnetic wave that goes through the ferromagnetic material.
The complex magnetic permeability is defined as:

$$\bar{\mu}(H) = \mu'(H) + j\mu''(H) \tag{4.1}$$

Where $\mu''(H)$ assumes negative values, because the imaginary part represents the delay of the magnetic flux on the magnetic field.
Consequently, to obtain the desired results, we propose the following procedure:

1. Build a function for the magnetic permeability $\bar{\boldsymbol{\mu}}(H(t))$ in the time domain, using the Presiach model to describe better the magnetic properties of the material.
2. Simulate the problem of eddy currents in the time domain on a mono dimensional space x when it is applied a sinusoidal transversal magnetic field on one edge of the sample.
3. Starting from the results of the time domain simulation, we export two distributions of losses along the sample's depth. The first distribution contains the Joule losses while a second one contains the hysteresis losses.
4. Determinate the function $\bar{\mu}(x)$ in the harmonic domain that reproduces the same losses that were previously calculated.
5. Link $\bar{\mu}(x)$ with $\bar{\mu}(H)$ using the results of the eddy current problem solved in the frequency domain, with the space variable x as parameter.

The procedure described in the first point was introduced in the chapter {3.3}. At the end of the characterization, we obtained the formulation of the complex permeability: the expression (3.10) derives from that function.
The second point will be exhaustively treated in the next chapter. In the following pages, we will talk about the last three points of the list.

4.2 Calculation of the losses in the time domain

Starting from the Maxwell's equations, we can write the diffusion equation for eddy currents in 1D dimension along x. Considering the magnetic field changing only along the y direction let us write:

$$\rho \frac{\partial^2 H(x,t)}{\partial x^2} = \frac{\partial B(x,t)}{\partial t} \tag{4.2}$$

Then we find the expression for the power in the time domain, using the divergence of the Poynting vector.

$$P(x,t) = \frac{\partial}{\partial x}\left[E(x,t)H(x,t)\right] \tag{4.3}$$

Must be noticed that the electric field had been defined positive in the direction - z. At the same time, we want to cancel the dependence of this expression by the electric field so let us apply the Ampere's law and the Faraday's law.

$$E(x,t) = \rho \frac{\partial H(x,t)}{\partial x} \tag{4.4}$$

$$\frac{\partial E(x,t)}{\partial x} = \frac{\partial B(x,t)}{\partial t} \tag{4.5}$$

Consequently, the power in the equation (1.3) becomes:

$$P(x,t) = \rho\left(\frac{\partial H(x,t)}{\partial x}\right)^2 + H(x,t)\frac{\partial B(x,t)}{\partial t} \tag{4.6}$$

In this expression, the first term represents the Joule losses while the second one corresponds to the energy lost for hysteresis.
Let us calculate the average of these losses in one electromagnetic period when the steady state is reached.

$$P(x) = \frac{1}{T}\int_0^T \left(\rho\left(\frac{\partial H(x,t)}{\partial x}\right)^2 + H(x,t)\frac{\partial B(x,t)}{\partial t} \right) dt \tag{4.7}$$

Where T is one electromagnetic period, associated to the fundamental frequency ω of the electromagnetic field. Then the expression can be split to regroup the Joule losses and the hysteresis losses.

$$P_{joule}(x) = \frac{1}{T}\int_0^T \rho\left(\frac{\partial H(x,t)}{\partial x}\right)^2 dt \tag{4.8}$$

$$P_{hyst}(x) = \frac{1}{T}\int_0^T H(x,t)\frac{\partial B(x,t)}{\partial t} dt \tag{4.9}$$

4.3 Calculation of the losses in the harmonic domain

At this point, the same losses in the harmonic domain are analysed. Using the Steinmetz transformation:

$$H(x,t) = \bar{H}(x)e^{j\omega t} \tag{4.10}$$

$$B(x,t) = \bar{\mu}(x)\bar{H}(x)e^{j\omega t} \tag{4.11}$$

Writing down the diffusion equation:

$$\rho\frac{\partial^2\bar{H}(x)}{\partial x^2} = jw\bar{\mu}(x)\bar{H}(x) \tag{4.12}$$

we can do an equivalent development to find the terms of the losses that represent the equation (3.3) in the harmonic domain.

$$P(x,t) = \frac{d}{dx}\left[Re\left(\bar{E}(x)e^{j\omega t}\right)Re\left(\bar{H}(x)e^{j\omega t}\right)\right] \tag{4.13}$$

Rewriting the terms, substituting $\bar{E}(x)$ with $\rho\, d\bar{H}(x)/dx$,

$$P(x,t) = \frac{dy}{dx}\left[Re\left(\frac{\rho}{2}\frac{d\bar{H}(x)}{dx}\,\overline{H}^{*}\right) + Re\left(\frac{\rho}{2}\frac{d\bar{H}(x)}{dx}\,\bar{H}(x)e^{2j\omega t}\right)\right] \tag{4.14}$$

Computing the mean to avoid the contribute of the second term we obtain:

$$P(x) = \frac{1}{T}\int_0^T\left[Re\left(\frac{\rho}{2}\frac{d\bar{H}(x)}{dx}\,\overline{H}^{*}\right) + Re\left(\frac{\rho}{2}\frac{d\bar{H}(x)}{dx}\,\bar{H}(x)e^{2j\omega t}\right)\right]dt \tag{4.15}$$

$$P(x) = \frac{d}{dx}\left[Re\left(\frac{\rho}{2}\frac{d\bar{H}(x)}{dx}\,\overline{H}^{*}\right)\right] \tag{4.16}$$

Finally, using the diffusion equation (1.12), we can express the previous expression in a different way in order to put in evidence the magnetic permeability.

$$P(x) = \frac{\rho}{2}\left|\frac{d\bar{H}(x)}{dx}\right|^2 + Re\left(\frac{-j\omega\bar{\mu}(x)}{2}\bar{H}(x)\overline{H}^{*}(x)\right) \tag{4.17}$$

$$P(x) = \frac{\rho}{2}\left|\frac{d\bar{H}(x)}{dx}\right|^2 - \frac{\omega}{2}\mu''(x)|\bar{H}(x)|^2 \tag{4.18}$$

Then, we can do again the separation between the losses due to Joule effect and the ones due to hysteresis.

$$P_{joule}(x) = \frac{\rho}{2}\left|\frac{d\bar{H}(x)}{dx}\right|^2 \tag{4.19}$$

$$P_{hyst}(x) = -\frac{\omega}{2}\mu''(x)|\bar{H}(x)|^2 \tag{4.20}$$

The equation (3.20) shows that the imaginary component of the magnetic permeability id directly associated with the hysteresis losses. As a matter of facts, when the imaginary component of $\bar{\mu}(x)$ is null, the dissipated power corresponds univocally to the Joule losses.

4.4 Determination of the complex magnetic permeability

Let us start defining the equations and the unknowns. In addition to equations (1.19) and (1.20), we can express two supplementary equations starting by the differential equation that describes the eddy currents in the harmonic domain (1.12). Moreover, the equivalence must be imposed both on the real and imaginary components.

$$\mu'(x) = Re\left(j\frac{\rho}{\omega}\frac{1}{\bar{H}(x)}\frac{d^2\bar{H}(x)}{dx^2}\right) \tag{4.21}$$

$$\mu''(x) = Im\left(j\frac{\rho}{\omega}\frac{1}{\bar{H}(x)}\frac{d^2\bar{H}(x)}{dx^2}\right)$$

There are four unknowns and four equations: μ', μ'', $Re\,(\bar{H})$ and $Im\,(\bar{H})$.
To have a lighter notation let us stop to explicit the dependence of space for the magnetic field.
Moreover, we decide to use the norm H and the phase ϕ of the magnetic field $\bar{H}$ as unknowns, instead of the real and imaginary component. Consequently, we have that:

$$\begin{aligned} Re(\bar{H}) &= H\cos ø \\ Im(\bar{H}) &= H\,sin\,ø \end{aligned} \tag{4.22}$$

After these modifications, the system becomes the following:

$$P_{joule} = \frac{\rho}{2}\left[\left(\frac{dH}{dx}\right)^2 + H^2\left(\frac{dø}{dx}\right)^2\right] \tag{4.23}$$

$$P_{hyst} = -\frac{\omega}{2}\mu'' H^2 \tag{4.24}$$

$$\mu' = \frac{\rho}{\omega}\left[\frac{2}{H}\frac{dH}{dx}\frac{dø}{dx} + \frac{d^2ø}{dx^2}\right] \tag{4.25}$$

$$\mu'' = \frac{\rho}{\omega}\left[\left(\frac{dø}{dx}\right)^2 - \frac{1}{H}\frac{d^2H}{dx^2}\right] \tag{4.26}$$

Substituting the magnetic permeability in (4.24) with the right−hand side of (4.26) and summing the modified equation to the Joule losses of the (4.23), we obtain an ordinary differential equation based on the norm H.

$$P_{tot} = \frac{\rho}{2}\left[H\frac{d^2H}{dx^2} + \left(\frac{dH}{dx}\right)^2\right] \tag{4.27}$$

The expression (4.27) is particularly interesting because it can be solved numerically leading back to the shooting method. This method consists in solving the differential equation with Runge−Kutta with an approximation of the initial values on the slope of the final function in the origin (element that explains the origins of the method' s name).

After the iteration with a non−linear algorithm, we obtain the slope that respects the boundary conditions.

Now, due to the fact the distribution of H in function of the space is known, we can calculate directly μ'' from the equation (4.24) and then we obtain the phase of the magnetic field from the equation (4.23).

To conclude this last passage, we have to choose the sign of the phase's slope.

Thanks to the fact we mentioned that the phase is in delay compared to the magnetic field penetrates in the material, we can find:

$$\frac{d\emptyset}{dx} = -\frac{1}{H}\sqrt{\frac{2}{\rho}P_{joule} - \left(\frac{dH}{dx}\right)^2} \tag{4.28}$$

Also, this last equation is solved with Rounge−Kutta. After that, the second derivate of the phase can be calculated as:

$$\frac{d^2\emptyset}{dx^2} = \frac{\Delta\frac{d\emptyset}{dx}}{\Delta x} \tag{4.29}$$

Therefore, the norm and the phase of the magnetic field are determined; now, finally, are calculated the real and imaginary components of the permeability.

In the end, the magnetic non−linear complex permeability is obtained, adopting the variable x as parameter to write down the bijective relation:

$$\bar{\mu}(H) = \bar{\mu}(H(x)) = \mu'(H(x)) + j\mu''(H(x)) \tag{4.30}$$

Chapter 5

Calibration Problem

In this chapter, the second point of the introductive list of the Power equivalent model is exhaustively explained. The problem of eddy currents will be simulated in the time domain, on a mono dimensional geometry, when it is applied a sinusoidal transversal magnetic field on one edge of the sample.

A separated chapter was dedicated to this procedure because it is going to be completed with the calibration study. After the losses are collected along a semi-infinite slab in the time domain, the new equivalent permeability is built. Then, the losses in the harmonic domain are collected too and eventually they are going to be compared and validated.

It is important to clarify that in this section and in the following chapters we will consider only the real component of magnetic permeability. This decision was made considering two aspects: firstly, we can neglect the contribution of hysteresis losses (as already mentioned). Then, for a methodological reason, we want to verify the validity of this new power equivalent model indeed, increasing progressively the complexity of our problem.

5.1 Characteristic problem in induction heating

The rate of energy transfer (i.e. heating power) and its spatial distribution within the workpiece is the true metric of comparison in this work. The simplest problem that models relatively well the diffusion of a magnetic field at the surface of a steel part is the 1D semi-infinite slab problem.
However, the choose of this problem is not due only by its simplicity but also because it is the extreme modelling of the electromagnetic problem of an induction heating problem. Applying a sinusoidal wave to an edge of the semi-infinite slab corresponds to the induced field in a workpiece produced by the copper coil. Moreover, the boundary condition that forces the applied field to a nihil value at the edge of the length of the sample, is similar to real case. In surface hardening, because of skill

effect, the penetration depth of the magnetic field and currents is remarkably shorter than the physical dimension of the workpiece.

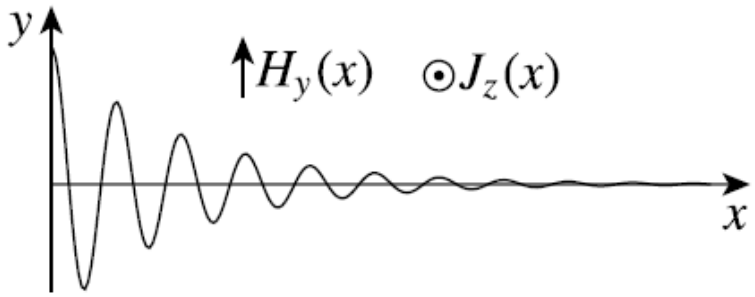

Figure 5.1 Semi−infinite slab for the calibration problem.

As visible in the *Figure 5.1*, in the calibration problem it is applied a sinusoidal magnetic field that is perpendicular to the slab. The slab starts in the origin and goes on along the x−axis, while the magnetic field applied on the extremity is the same as the one produced by a sinusoidal current flowing into a conductor outgoing from the plane. The problem was solved with the finite element method (implemented in *COMSOL4.3 ®)* through a PDE physic formulation.

$$\begin{cases} \rho \dfrac{\partial^2 H(x,t)}{\partial x^2} + \dfrac{\partial B(x,t)}{\partial t} = 0, & x \in]0, L[\\ H(0,t) = H_0 \sin(\omega t)\,;\; H(L,t) = 0, & L \gg \delta \end{cases} \tag{5.1}$$

It is interesting to notice that in the formulation used in the calibration problem appears a length parameter L. As a matter of fact, to bound and bring to a finite number of element the calibration problem we use a segment of a fixed dimension, but thanks to the boundary condition and the dimension that must be chosen several times bigger than the penetration depth, that does not affect the validity of our problem.

Parameter	Symbol	Expression	Value	Unit
rho_steel	ρ_{steel}	$1/\sigma_{steel}$	$25e^{-8}$	$[\Omega * m]$
Maximal magnetic permeability	μ_{r0}	–	600	-
frequency	f	–	1000	$[Hz]$
period	T	$1/frequency$	$1e^{-3}$	$[s]$
Final time	t_{max}	$10 * T$	$10e^{-3}$	$[s]$
Lenght	L	-	$5e^{-2}$	$[m]$
Penetration depth	δ	$\sqrt{\frac{2\,\rho_{steel}}{\omega\,\mu_0\,\mu_{r0}}}$	$3{,}2487e^{-4}$	$[m]$
Amplitude	H_0	-	$1e^{5}$	[A/m]

Table 5.1 Calibration problem's parameters.

In the *Table 5.1* are presented the parameters and the values adopted to run the calibration problem. They underline some peculiar aspects of our study. For the steel resistivity, we use the value extracted by the experimental data of *Figure3.3* at room temperature. The value of the maximal relative magnetic permeability confirms that the analytic expression (3.5) is being used as reference saturation curve. The frequency is arbitrarily chosen equal to 1 [kHz]: in this particular stage of the project is not yet taken into account the real range of frequencies for induction heating. Moreover, the mesh size for the FEM model is customized because every element is one tenth of the penetration depth, so using a smaller frequency reduces the total number of elements and consecutively the computational time. The final time for the simulation is decided in order to achieve, without a doubt, the steady state. As a matter of facts, the Power Equivalent model is built calculating the losses in one electromagnetic period.

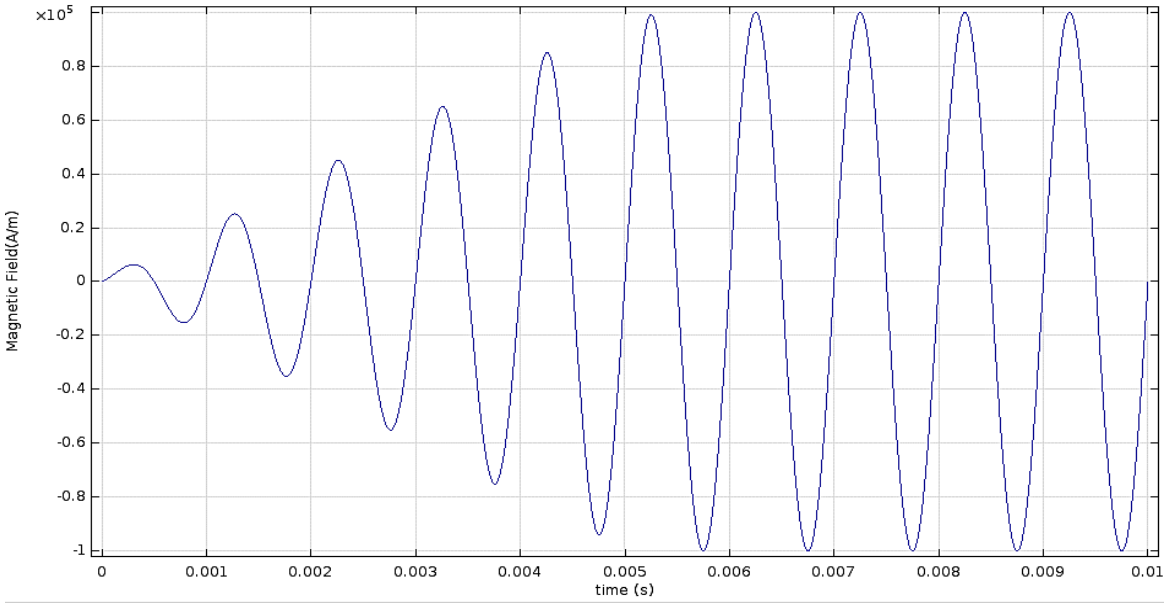

Figure 5.2 Time evolution of the applied magnetic field. It is possible to see how it raises through a transient situation and reaches the steady state.

The penetration depth is calculated with the expression (3.7) according with the material parameters introduced in the chapter {3}. After that, it is stablished the length of the slab approximating the total length over one hundred times bigger than the penetration depth. Finally, it is chosen the amplitude of the sinusoidal magnetic field equals to $1*10^5$ [A/m]: a very remarkable value. As a matter of facts, the order of magnitude for magnetic field in induction hardening treatments is known in literature, but the value is chosen to reach a deep saturation level in the *BH curve*.

5.2 Equivalent BH curve

After that the simulation in the time domain is run, the losses and the distribution of the magnetic field in one electromagnetic period are measured, the power equivalent model is developed as it is explained in the chapter {3}.
As final result, it is obtained the value of magnetic permeability in function of the magnetic field. Therefore, in order to plot it in a more interesting way, let us calculate the magnetization field and compare it with the normalized magnetization curve of *Figure 3.4*, used as reference curve.

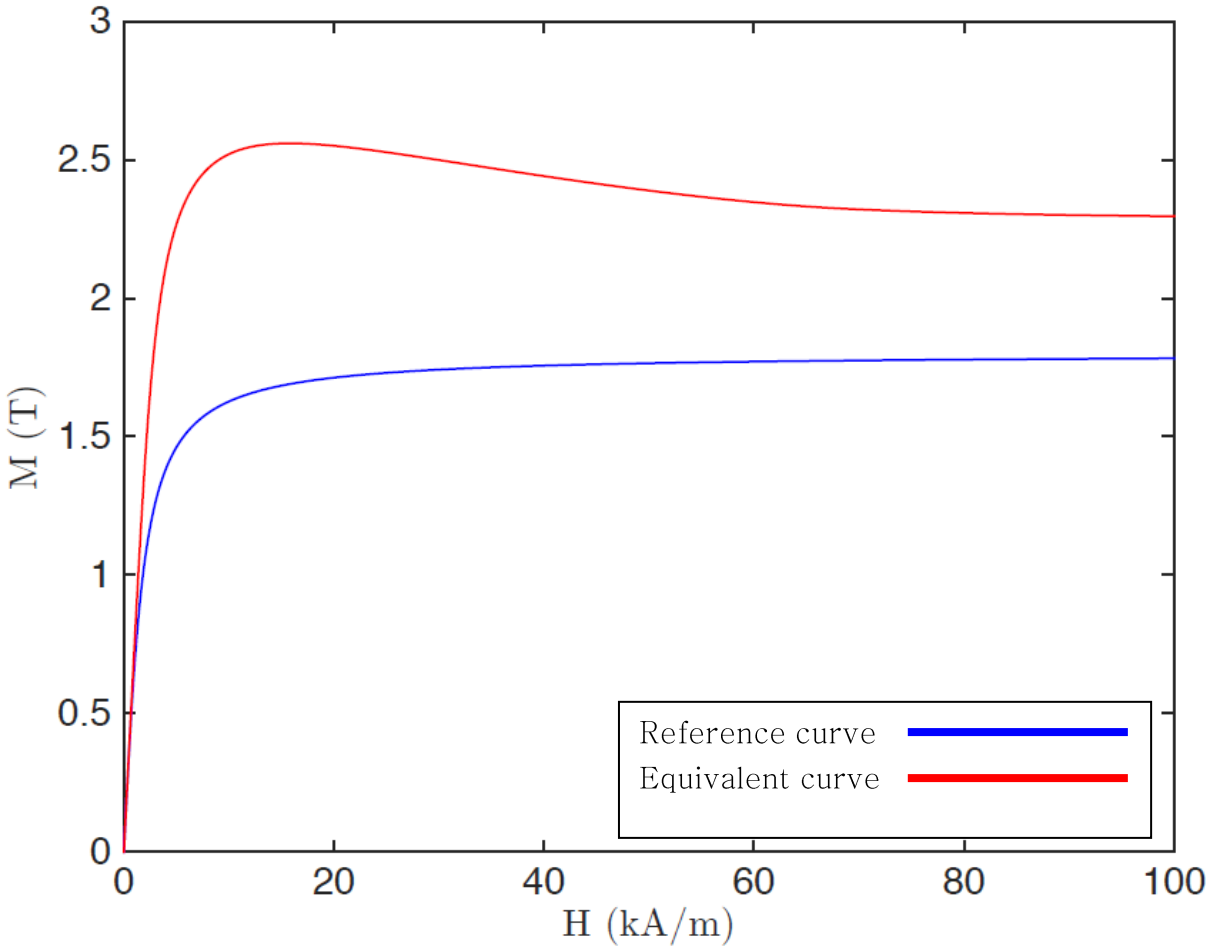

Figure 5.3 Normalized magnetization curves. The blue curve shows the magnetization field in function of magnetic field, extracted from the reference curve. The red line shows she same plot extracted from the new Power Equivalent model.

In the figure above, the two BHcurves can be compared and, even if they are different, they describe the same medium. As a matter of fact, one curve describes the material magnetization in function of the magnetic field. The first is used in the time domain simulation and it is the reference curve. The second one describes the magnetization of the medium but, it reaches greater values of induction magnetic field, it takes off and reaches a peak before decreasing and stabilizing into an asymptotic value.

This pattern for the two curves can be explained quite easily considering the fact that the nonlinear B–H behaviour introduces a high harmonic content of induced currents in a workpiece, that is exposed to an external magnetic field.

The new Equivalent Power model wants to approximate the same complicated superimposition of effects considering only the first harmonic.
That explains why the equivalent curve has higher values indeed and also because it presents a peak in correspondence of the reference curve's knee.
More interesting is to plot the normalized magnetization curve related to a parametric study for the amplitude of the imposed magnetic field. The image illustrates the equivalent curve built using the losses generated in the same medium when it is applied a periodic excitation. In the figure are plotted the reference curve and the equivalent curves obtained with a magnetic field that has several amplitude values (e.g. H_0 = (50,100;200) [kA/m]).
As is observable from the *Figure5.4* higher is the amplitude value, higher is the peak of the equivalent curve. However, all the equivalent curves tend towards a horizontal asymptote and near the origin have the same slope. This behaviour is justified by the electromagnetic behaviour of the medium: near the origin of the axes (i.e. with small value of magnetic field) the relation between magnetic field and induction magnetic field is linear. In case of deep saturation, the magnetization field does not increase because all the magnetic dipoles are oriented along the field direction so the equivalent curves describe the same phenomenon.

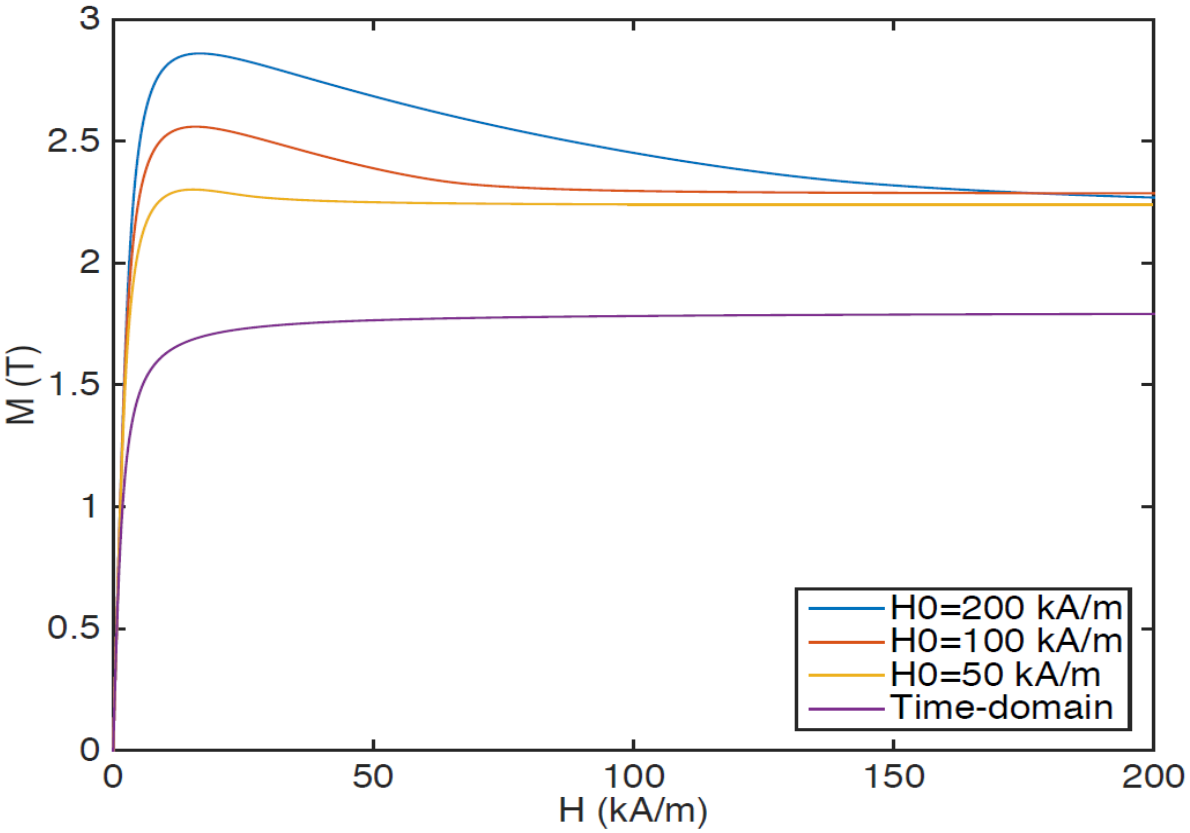

Figure 5.4 BH diagram where are plotted normalized magnetization curves. There is the reference curve and the equivalent curves obtained with a parametrization of the external magnetic field H_0.

What is more interesting is the pattern of the curves in proximity of the saturation knee. It can be noticed that the peak of the equivalent curve increases according with the amplitude of magnetic field (i.e. greater is the amplitude, greater is the peak value and vice versa). It is not possible to explicit such a direct implication because the equivalent curve is built through the distribution of the losses along the sample. However, it is quite intuitive to understand that, with an elevate value of magnetic field is reached a more elevate saturation point. Consequently, the higher order harmonic content induced in the workpiece will be greater and the equivalent curve (that has to approximate this content) will have a more altered pattern, compared to the reference curve.

5.3 Verification of the losses

Arrived at this point it is possible to run a simulation in the frequency domain with the finite element method (implemented in *COMSOL4.3 ®)* through a PDE physic formulation.

$$\begin{cases} \rho \dfrac{\partial^2 \bar{H}(x)}{\partial x^2} + j\omega\bar{\mu}(H)\bar{H}(x) = 0, & x \in]0, L[\\ H(0) = H_0; \;\; H(L) = 0, & L \gg \delta \end{cases} \tag{5.2}$$

The system is the transposition in the harmonic domain of the same problem presented in the system (5.1). Using the Steinmetz transformation, the dependence of time disappears and the time derivative becomes a multiplication for $j\omega$. Moreover, the induction magnetic flux had been decomposed in the product of the magnetic permeability and the magnetic field. In the expression, the magnetic permeability maintains the complex notation to have general validity, even if it has only real component in this simulation (for the reasons already explained).
The simulation is run in order to validate the PE model: hence, the magnetic permeability is the one obtained by the equivalent BHcurve of *Figure 5.3* . The equivalent magnetic permeability is introduced in the problem' s parameters thanks to an interpolating function by points; the other parameters are the same reported in *Table 5.1* .

Exported from the simulation the distribution of specific eddy current losses along the sample, it can be compared with the ones collected from the time domain simulation: the results are plotted in *Figure 5.5* .

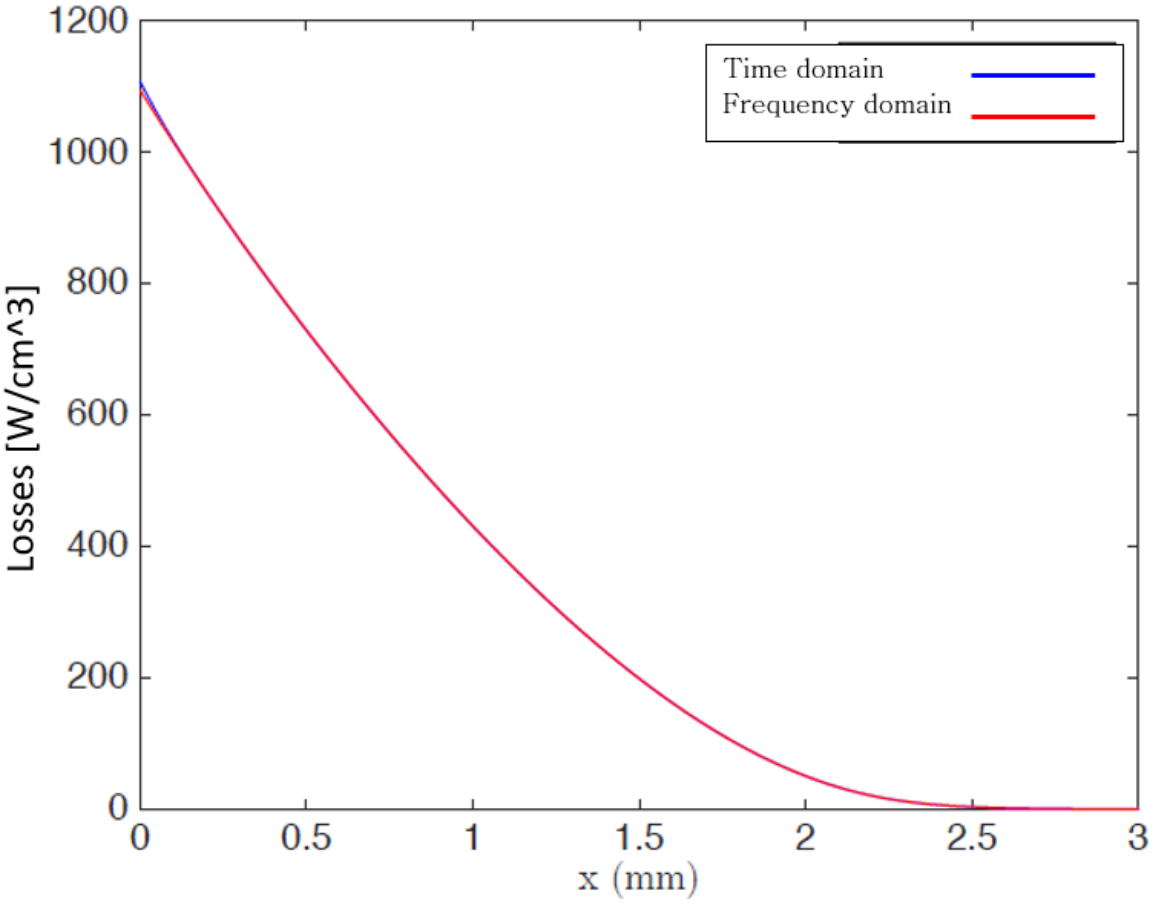

Figure 5.5 Comparison of losses collected in the time domain simulation and in the harmonic domain simulation.

The blue line represents the average distribution of the losses in one electromagnetic, period losses collected in the time domain simulation. The red curve represents the losses calculated in the harmonic domain with the new Power Equivalent model. As is evident from the graph: the two distributions of losses in perfectly match. This verify the validity of the Power Equivalent model in 1D problems. The Power Equivalent model will be studied and compared in 2D and 2D axial symmetric cases in the next chapter of this paper.

Giving a more accurate look at the curve we can notice that the penetration depth after whom the losses drop to zero is bigger than the one considered with the equation (3.7). This is since we are dealing with nonlinear behaviour so we are considering the worst case ever. Therefore, the real magnetic permeability decreases from the maximal value found in the origin of the diagram. Typical value to calculate the penetration of the losses are smaller than one hundred. However, in the analytic formulation is used the maximal value of magnetic permeability, so it is automatically

guaranteed that with at least three elements for penetration depth there is a sufficient accuracy.

In conclusion, the theoretical hypothesis presented in the previous chapter has been validated. However, the reason why these kinds of simulation had been defined "calibration problem" can be explained. The term calibration derives from the fact that we need some parameter to define a unique equivalent curve to use in the FEM frequency simulations: the most remarkable parameter is the amplitude of the external magnetic field. According with *Figure 5.4* a small change in the exciting magnetic field implies a notable variation in the losses.
Moreover, this calibration problem has a sample sufficiently long compared to the penetration depth because the aim is to simulate an induction heating process. There, the portion of medium interested by the induced currents is relatively small compared to the total length. However, in the case of induction heating of small samples or other electrothermic treatments is necessary to modify the boundary conditions of the problem.
As concerning the frequency, it can be noticed that the equivalent curve (as the reference BHcurve) is independent from this parameter: the curve collected at 1 [kHz] is still valid if it is used at 100 [kHz]. As is evident from the equation (5.2), the frequency component is considered in the multiplication with the angular velocity. Nevertheless, this affirmation is valid uniquely under the hypothesis that the hysteresis loop does not change according with the frequency. In this thesis this hypothesis is assumed, because of the aspects already discussed.

Chapter 6

Test Cases

In this chapter, dedicated to test cases, the distribution of the losses between a time domain simulation and a frequency domain one will be compared. As already done in the previous chapter, the time domain simulation supplies the distribution of eddy current losses in one electromagnetic period, when it is reached the steady state and the medium is characterized by the reference non-linear behaviour. On the other hand, the frequency domain simulation provides the distribution of the losses but it considers only the first harmonic with the new PE model.
To improve the comparison, the geometry will be moved from a simple situation and will be drawn near the induction heating simulation. Moreover, these studies are all characterized by a series of parametric sweeps in order to expand the knowledge of this new PE model.

6.1 Test case 1: 1D geometries

The first test case studies the transition from a thick to a thin slab in a 1D problem. As a matter of fact, we parametrize the length d of the slab: with this operation, we can see when our distribution of losses drifts apart from the time domain simulation's result.
Because the geometry is one-dimensional we can use the same model built for the calibration problem. The FEM simulations in COMSOL reproduce the same PDE physics expressed in the systems (5.1) and (5.2). The mesh elements are again customized to have, as maximal dimension, one tenth of the penetration depth. All the medium properties and the parameter of the magnetic exciting field are reported in *Table 5.1.*
In this first test case, the boundary conditions are punctual condition: on the right-hand side a Dirichlet boundary condition can be seen where is imposed the external magnetic field (it changes in function of time in the time domain simulation, while in frequency one it assumes only a punctual value). On the left-hand side instead, there is a Neumann boundary condition that links the outgoing magnetic flux.
As a matter of fact, if the spatial derivate along that point is equal to zero it means that the magnetic field cannot change in function of space, but this confutes Biot-Savart's law. Consequently, the only possibility is that the magnetic field is nihil.

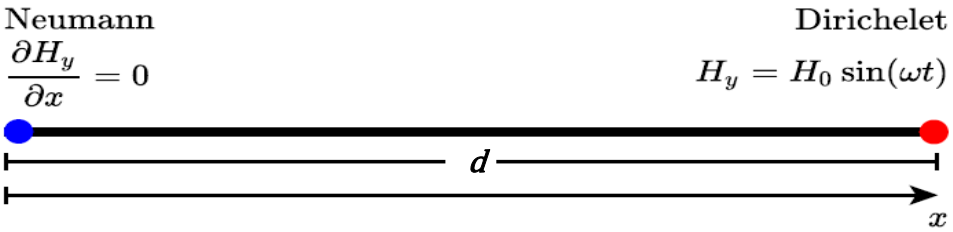

Figure 6.1 Test case 1: steel slab with parametrized length "*d*".

The results of the distribution are collected with the length that decreases from 10 [mm] until 1 [mm] with steps of 1 [mm] and after that with steps of 0.25 [mm]. With this approach, we can notice the limits of our model and we can recall the geometry parameter from the calibration problem. The *Figure 6.2* plots the specific absorption rate (losses divided by medium density) resulted from the PE model (in the frequency domain) and the ones coming from the time domain simulations. In addition, it is illustrated the distribution collected from the calibration problem. However, this reference curve is not visible because it is almost perfectly superimposed to the curves with a smaller length of the sample. In the figure are not plotted all the lines, but only some couples in order to have a cleaner graph to observe.

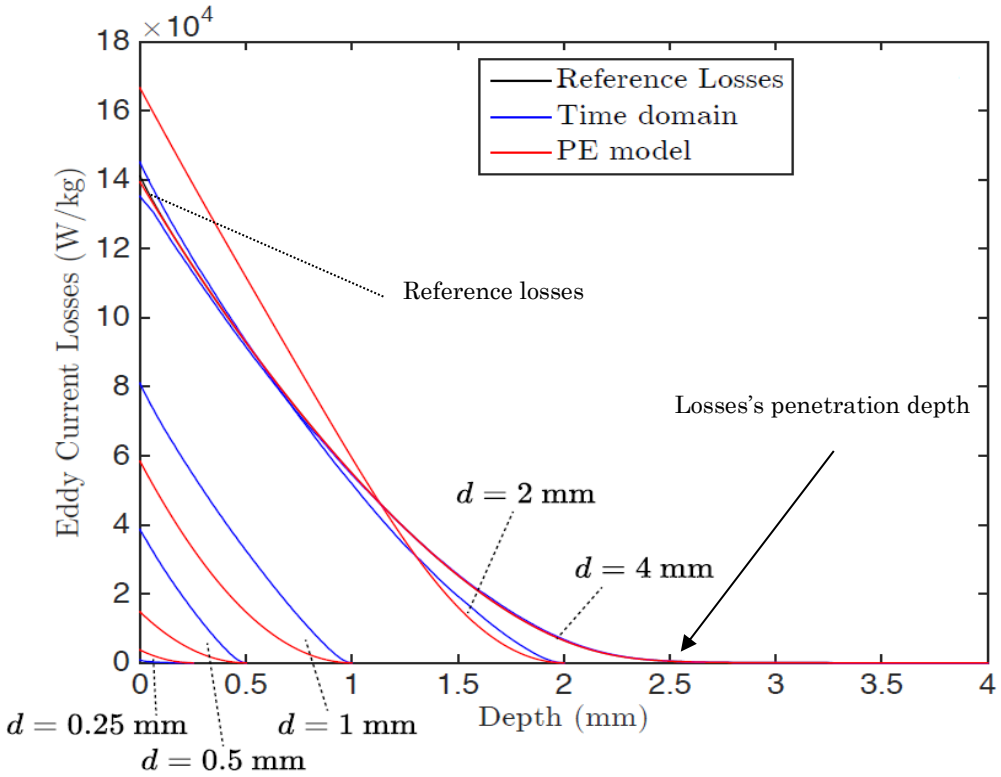

Figure 6.2 Test case 1: comparison with parametrized length "*d*".

The curves illustrate a good pattern match between the frequency and time solutions until the length is bigger than the "penetration depth of the losses". With this term, we considerate the spatial dimension at which the losses drop down near to zero. Because of the similarity with the calibration problem and for all the reasons already mentioned, the losses fall near 2.5 [mm]. When the length of the sample is minor than this length we see that the two curves become increasingly more detached.
In conclusion, from this test case, we have realized that is not possible to simulate problems where the length of the sample is smaller than the spatial penetration of the induced fields. The only possible operation is to return to the calibration problem and customized the boundary conditions in order to comprehend these cases. However, this situation is far away from the process that we want to simulate, so we give only this information as a comment to the results obtained.

At this point, the complexity of the geometry in the simulation can be increased and then compare the distributions in 1D axial symmetric case. Therefore, the sample becomes a cylinder with infinitesimal height. The boundary conditions and the material parameters are the same of the previous test case. The only difference is that now the parametric study is made modifying the radius R of the cylinder that has the exciting sinusoidal field applied around its surface.

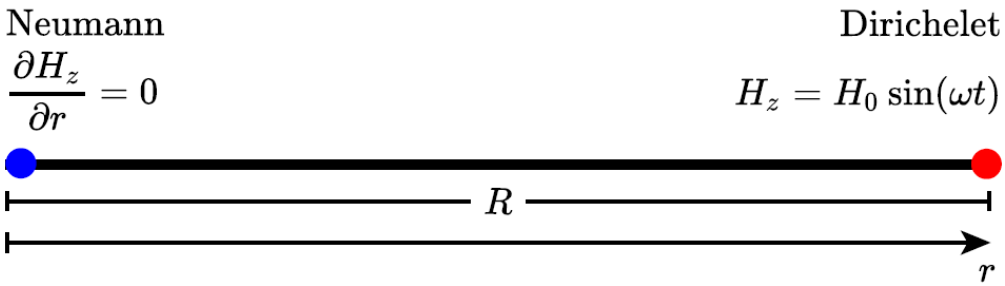

Figure 6.3 Test case 1, 1D axial−symmetric geometry: infinitesimal cylinder with parametrized radius "R".

In this second geometry, the losses collected with the PE model have a good pattern match with the time domain ones until we reach the penetration depth of the losses. Taking as reference the distribution collected with the calibration problem we can see that it changes a little bit with the reduction of the radius.
Bigger is the radius, close the problem is to the calibration problem and their boundary condition. Taking into consideration a smaller radius the boundary condition in the symmetric axis becomes more inaccurate. This can be particularly observed in *Figure 6.4* where the radius is parametrized in function of the analytic penetration depth. However, the objective of our study (i.e. compare time and frequency domain simulations) is reached; so the analysis of test cases will be carried on.

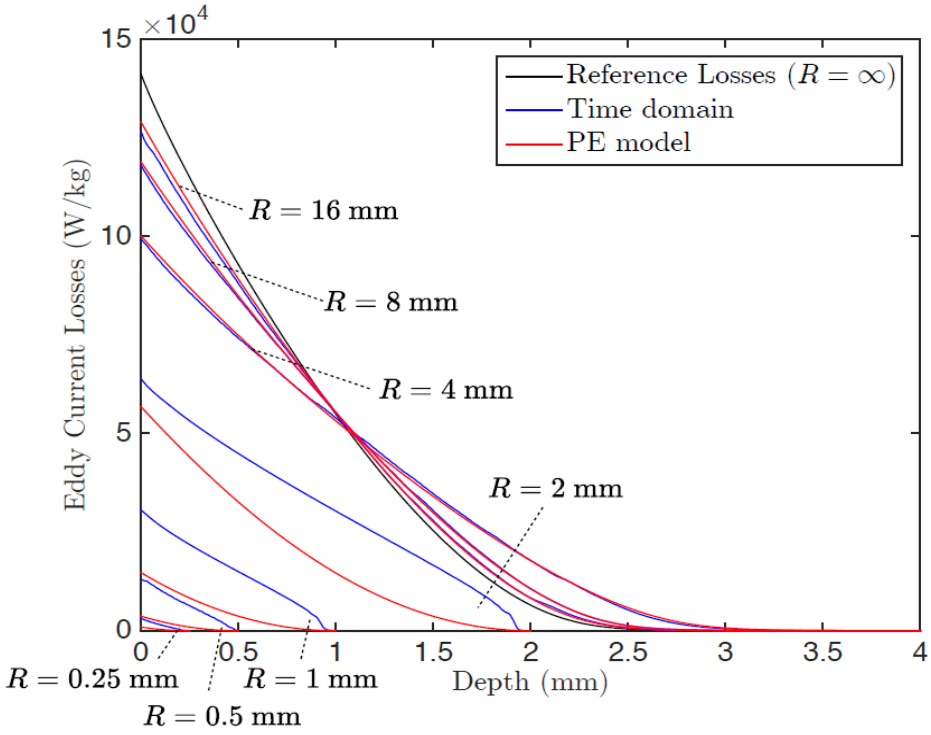

Figure 6.4 Test case 1,1D axial−symmetric geometry: comparison of specific absorption rates in an infinitesimal cylinder.

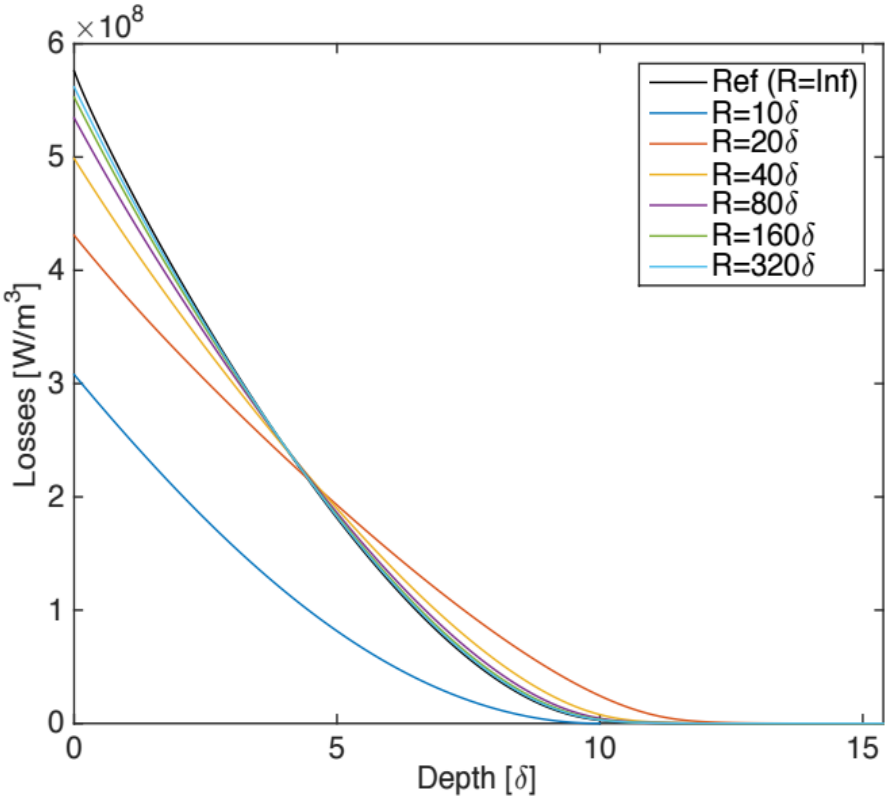

Figure 6.5 Test case 1,1D axial−symmetric geometry: specific losses in an infinitesimal cylinder, with a parametrization of the radius R.

6.2 Test case 2: 2D geometry

In the second test case, a 2D geometry is carried out with a study from narrow fins to narrow gaps. In fact, the behaviour of the induced magnetic field near corners and boundary conditions, is analysed. There is a steel "*L*" profile where the thickness of the lateral extrusion (named with the parameter *a*) changes. Three groups of simulations are made: *a*=1, *a*=5 and *a*=9 [mm].

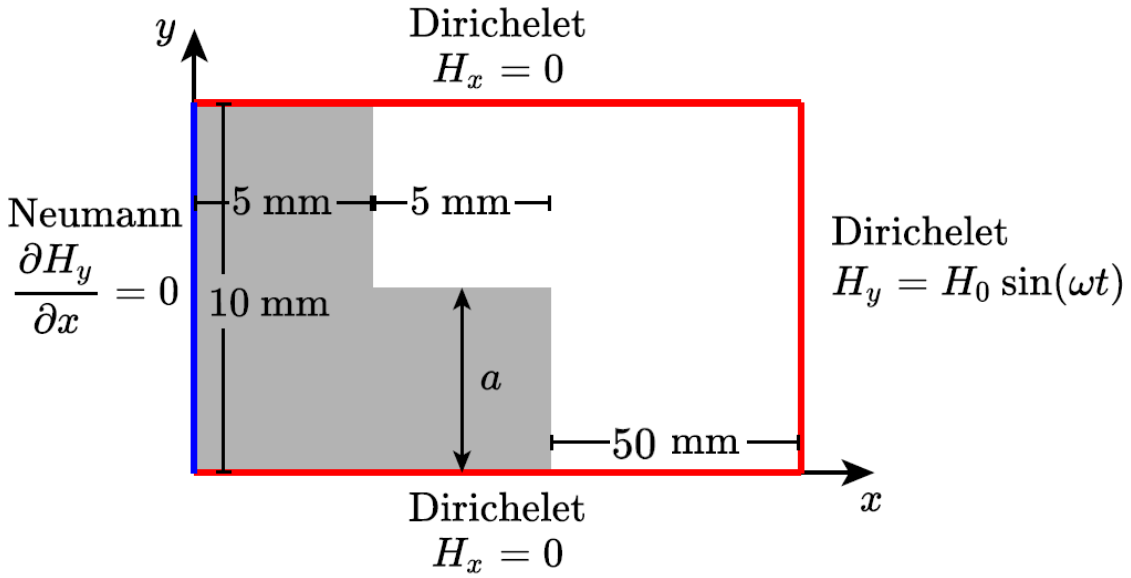

Figure 6.6 Test case 2, study from narrow fins to narrow gaps.

In the figure above are represented not only the dimensional values of the sample, but also the boundary conditions. On the right side, there is the Dirichlet condition that impose the sinusoidal magnetic field, on the bottom and on the top, there is another Dirichlet condition that bound the value of the magnetic field's component along abscissa equal to zero. Finally, there is the Neumann condition on the left side that impose the gradient of the exciting magnetic field equal to zero (i.e. the tangential component of the magnetic field is nihil). Those conditions work as symmetric plane: it means that the sample is immerged in a region where there is a uniform alternating magnetic field. Along the top and bottom lines the field is perfectly perpendicular: practically speaking we are considering only a small portion of an infinite long sample where the exciting field is generated on one side.

Below there is a chart containing all the parameters utilized in this test case. Mostly are the same of the calibration problem, however it is interesting to notice that the air region is considered with an electrical conductivity of 50 [S/m]. This decision was made in order to speed up the convergence of the simulation, but the physical accuracy is maintained because there are no currents that flow outwards the steel sample and close a lop in the air (the difference is more or less five orders of magnitude).

Parameter	Symbol	Expression	Value	Unit
rho_steel	ρ_{steel}	$1/\sigma_{steel}$	$25e^{-8}$	$[\Omega * m]$
rho_air	ρ_{air}	$1/\sigma_{air}$	$2e^{-2}$	$[\Omega * m]$
Maximal magnetic permeability	μ_{r0}	–	600	-
frequency	f	–	1000	$[Hz]$
period	T	$1/frequency$	$1e^{-3}$	$[s]$
Final time	t_{max}	$10 * T$	$10e^{-3}$	$[s]$
height	h	-	$10e^{-3}$	$[m]$
width	l	-	$10e^{-3}$	$[m]$
Lateral extrusion	a	-	$(1; 5; 9)e^{-3}$	$[m]$
Fillet radius	R_{fillet}	-	$25e^{-5}$	$[m]$
Air gap	air_{gap}	-	$50e^{-3}$	$[m]$
Penetration depth	δ	$\sqrt{\frac{2\,\rho_{steel}}{\omega\,\mu_0\,\mu_{r0}}}$	$3{,}2487e^{-4}$	$[m]$
Amplitude	H_0	-	$1e^{5}$	[A/m]

Table 6.1 Parameters of Test case 2.

Before analysing the results of this test case it is relevant to give a look to the construction of the mesh. There is a finer mesh in the steel layer close to the surface: the thickness of this layer is around 1.5 [mm] (i.e. 5 penetration depths). Here the triangular elements have a quadratic interpolation and a maximal size of one quarter of the penetration depth. Hence, we can have a good accuracy near the corners of the profile too. Outside the fine structure region, the mesh grows with a growth rate of 1.5.

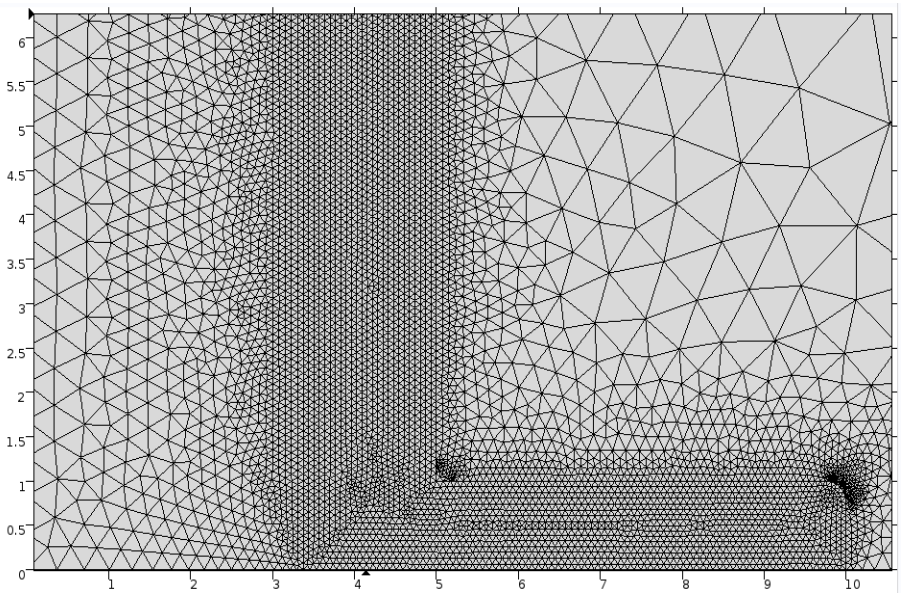

Figure 6.7 Test case 2, mesh structure of the steel profile.

As concerning the physic model that compares the distribution of the losses between the time and PE model simulations, we have to underline a peculiar aspect.
While the time domain simulation uses the reference BHcurve and the relative magnetic permeability plotted in function of the magnetization field (in the "*mf*" physic in COMSOL), this is not possible in the simulations made with the PE model. As the *Figure6.6* illustrates, the relative magnetic permeability does not describe a bijective function. Hence, the only possibility, to include this equivalent non-linearity, is to customize a PDE formulation building the equation (4.12) for every component of the magnetic field.

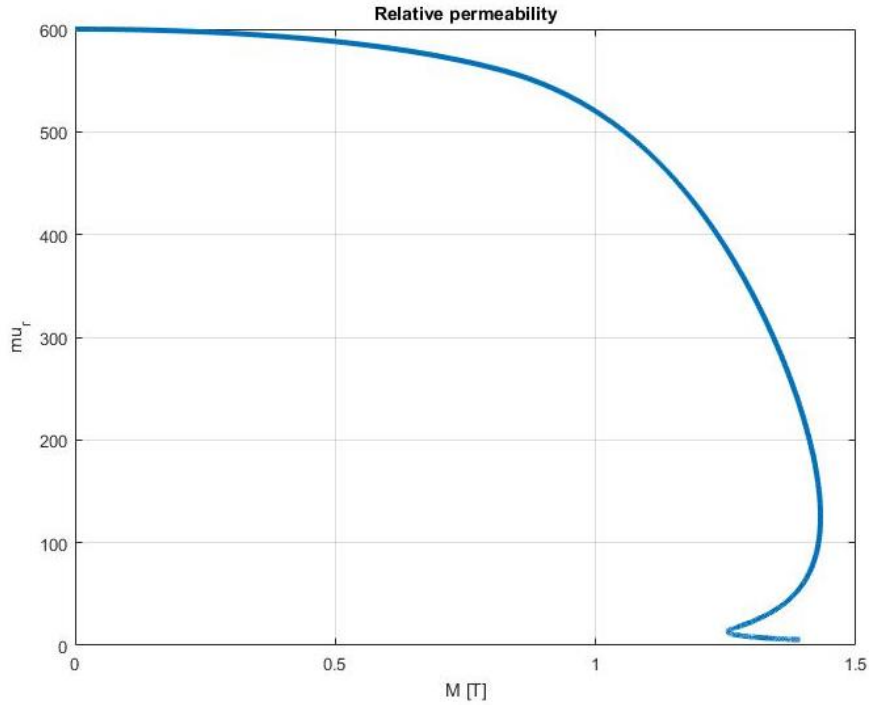

Figure 6.8 Relative magnetic permeability of PE model plotted in function of the magnetization field M[T].

Results of Test case 2

To better analyse the results of this test case in function of the parametric study, the data are subdivided in two group. In a first part, it is illustrated the comparison of the losses along some cut-lines. Then, it is plotted the distribution of the losses in the whole steel surface.
For every value of the parameter ***a*** three cut-lines are drawn in correspondence of the lateral extrusion plus one above and below it. Operating in this way we can collect a distribution on the thicker part of the sample and in the thinner one.
In the figure below there is a qualitative illustration of the cut-lines. All the diagrams show for every cut-line a continuous line for the time domain simulations and a dot line for the harmonic domain simulation.

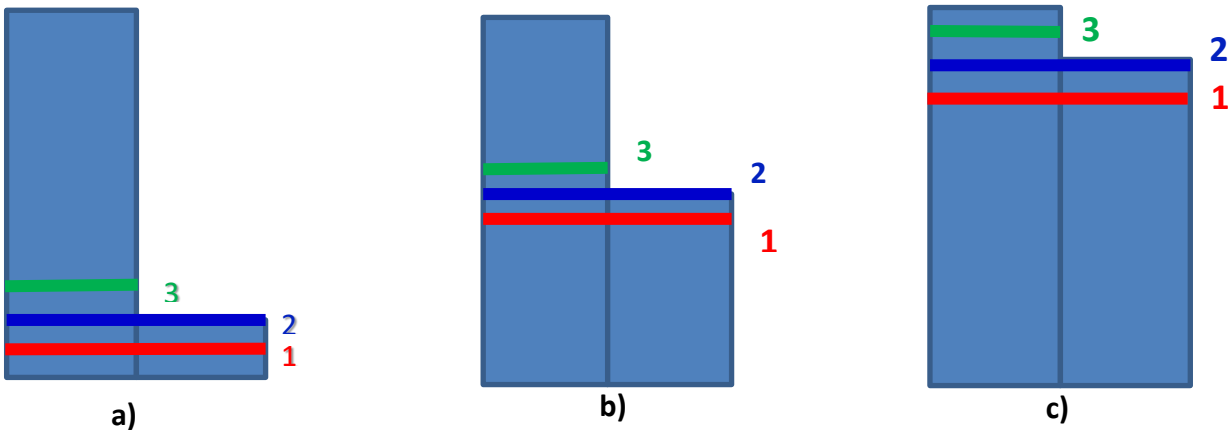

Figure 6.9 Cut−lines in the Test case2 characterized by a numeration and a colour. In a) the height of a =1 [mm]; b) a =5 [mm]; c) a =9 [mm]

As evidenced in the figures below, the losses in the PE models give a greater value of specific losses compare to the time domain. The surface of steel sample coincides with the ordinate axis in the diagrams. The pattern match is good in the green lines (the cut−lines above the lateral extrusion) while the curves are detached in the other situations. To understand better the reasons of this behaviour let us take into account the surface distribution of the losses in the 2D plot group. In the following pages are presented also, the images of the test cases divided by value of the parameter ***a.*** For each parametrization are presented the absolute values of: the distribution of specific absorption rate, the normalized value of the magnetic field, the absolute error between time and harmonic simulations and the relative error (considering the time simulation as reference).

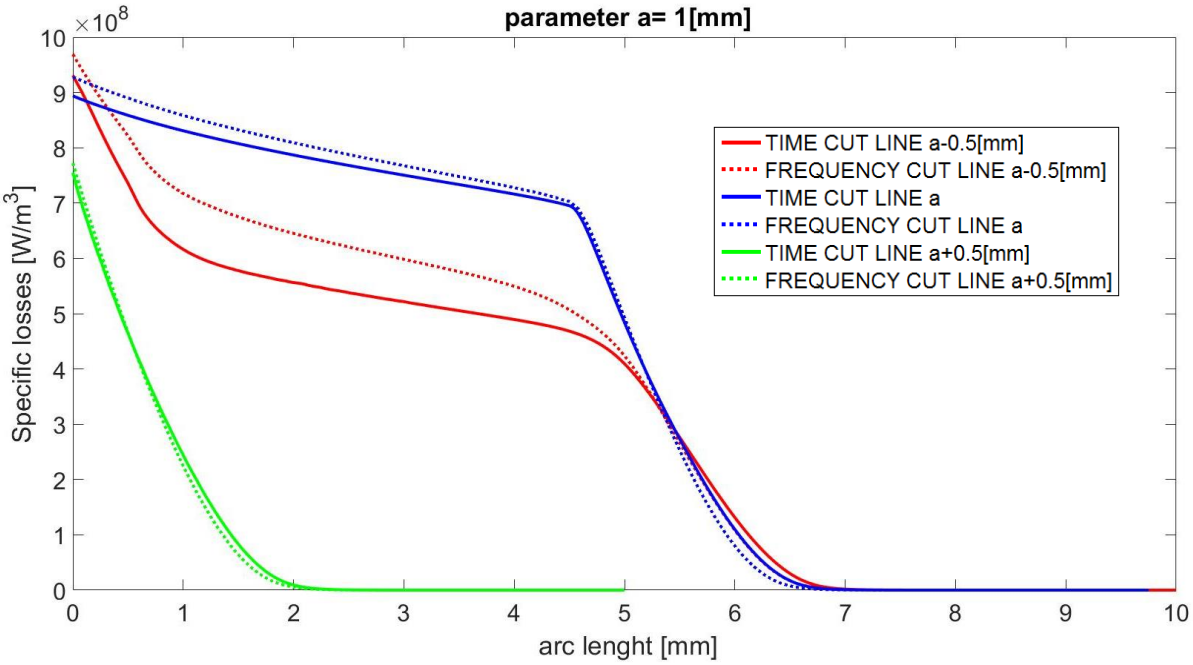

Figure 6.10 Cut−lines in the Test case2 with the parameter a =1 [mm]

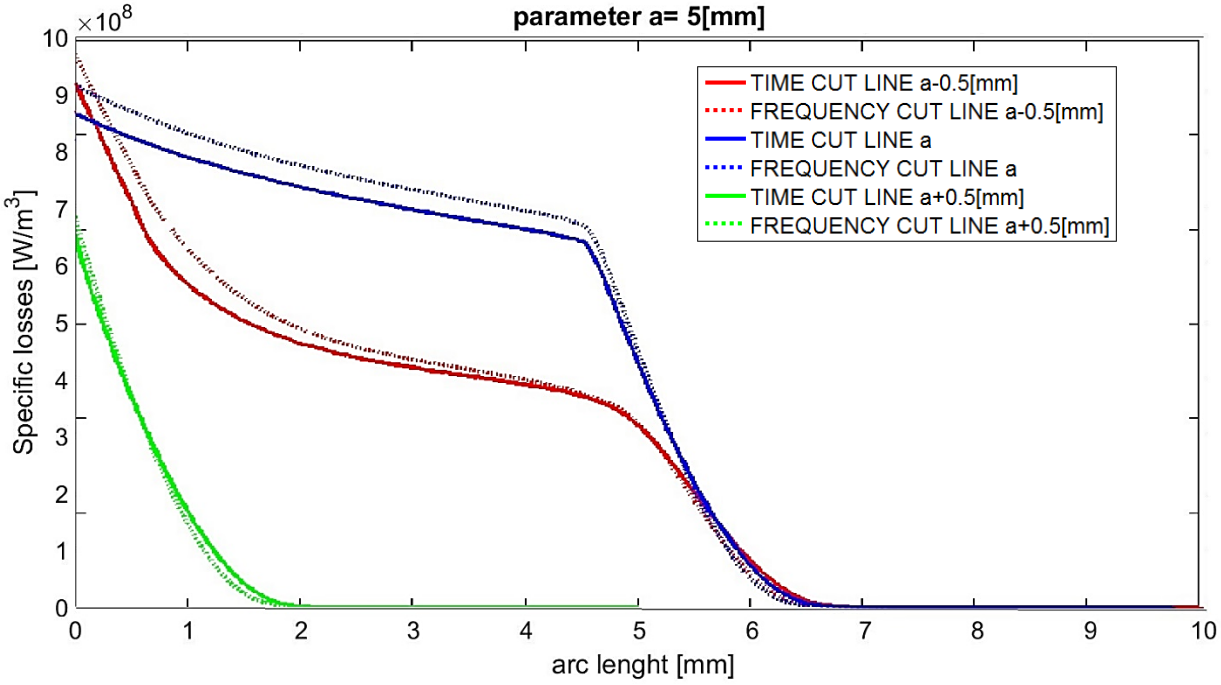

Figure 6.11 Cut-lines in the Test case2 with the parameter a =5[mm]

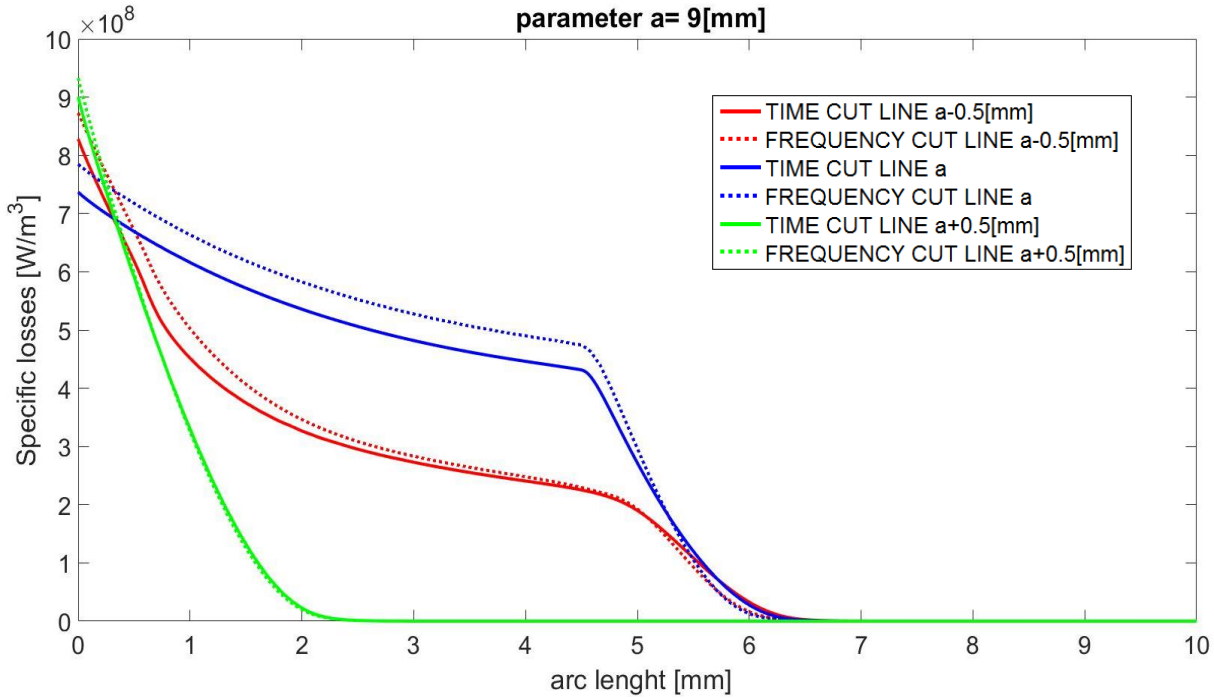

Figure 6.12 Cut-lines in the Test case2 with the parameter a = 9[mm]

Lateral extrusion a= 1 [mm]

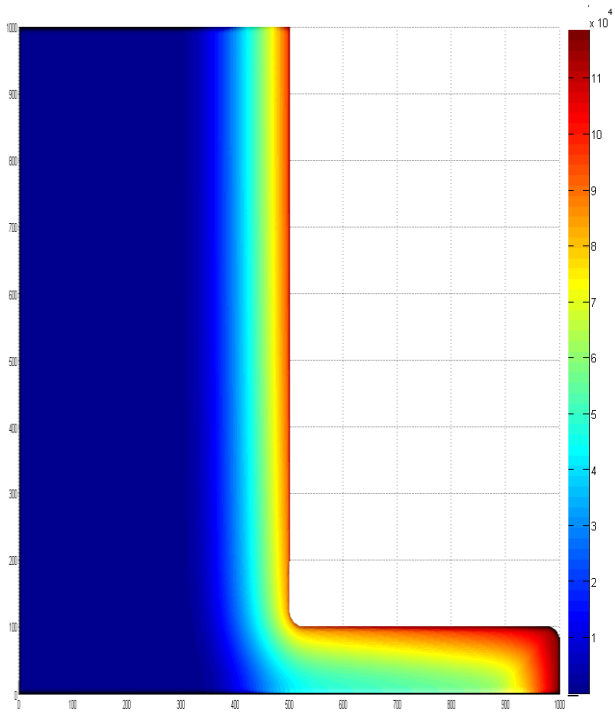

Figure 6.13
specific losses [W/kg] in the time study

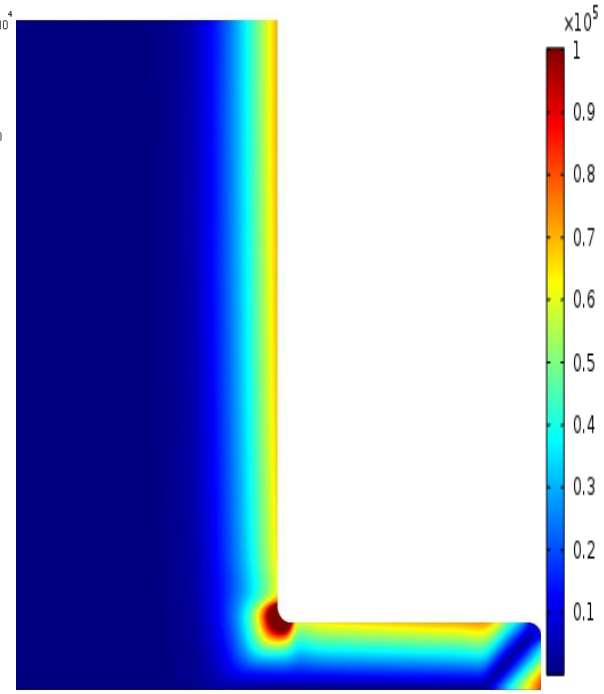

Figure 6.14
Absolute value magnetic field [A/m]

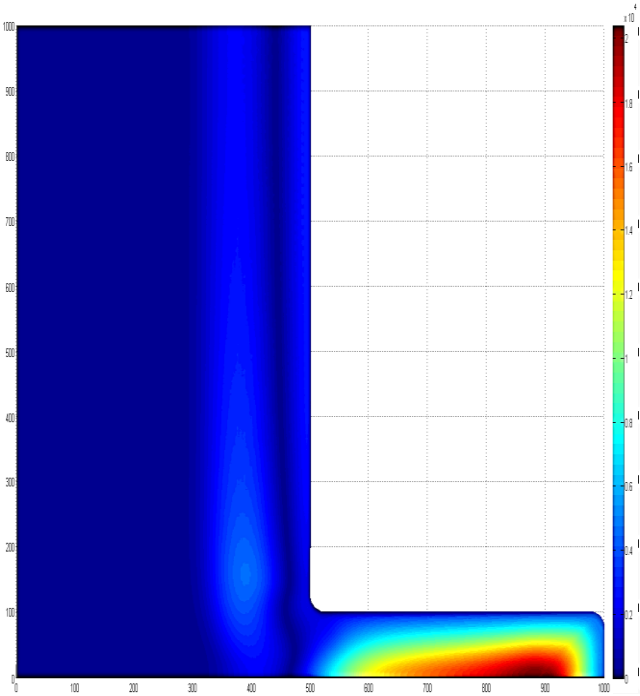

Figure 6.15
Absolute error between the losses [W/kg]

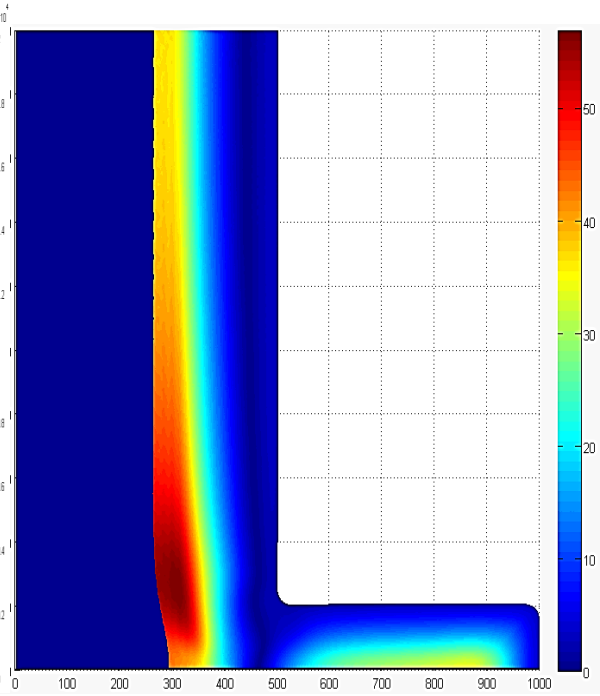

Figure 6.16
Relative error of the losses in %

Lateral extrusion $a = 5$ [mm]

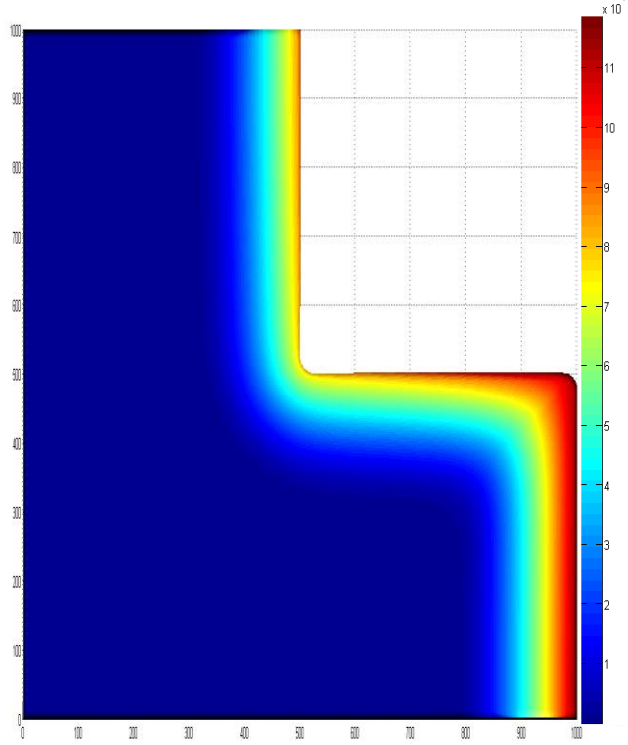

Figure 6.17
specific losses [W/kg] in the time study

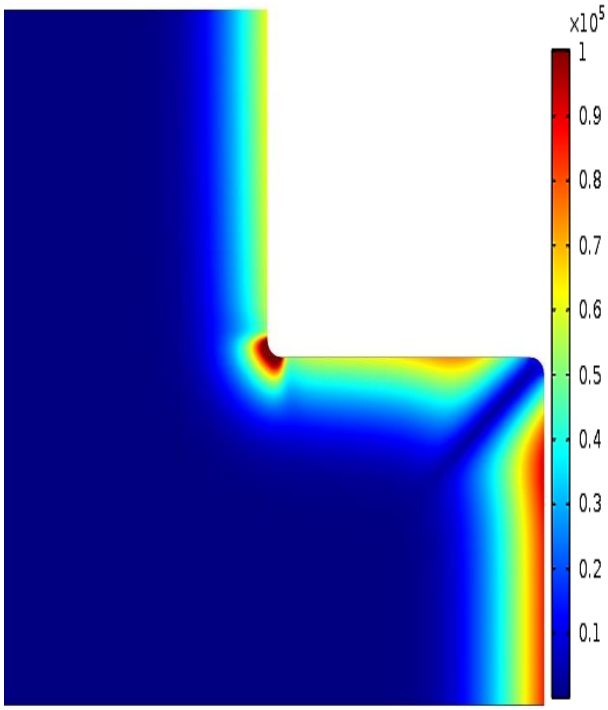

Figure 6.18
Absolute value magnetic field [A/m]

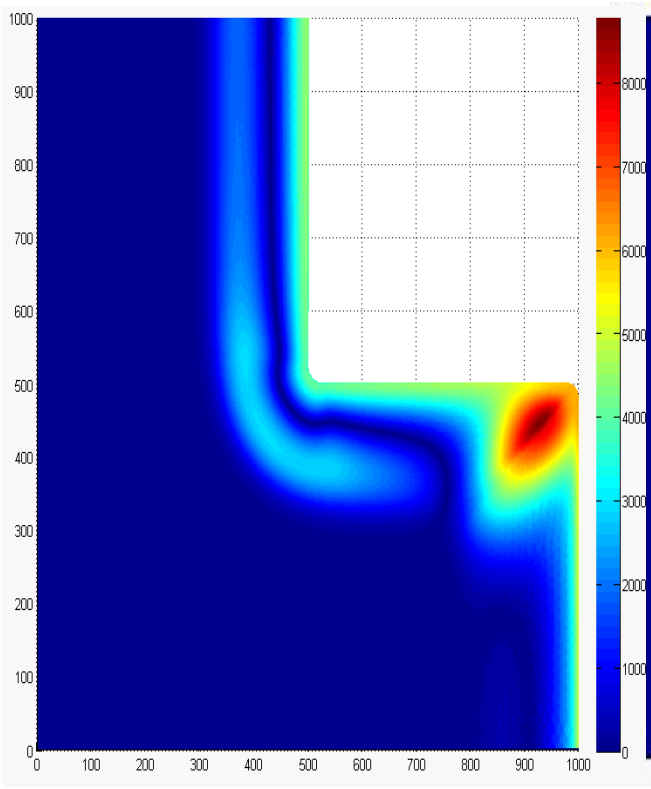

Figure 6.19
Absolute error between the losses [W/kg]

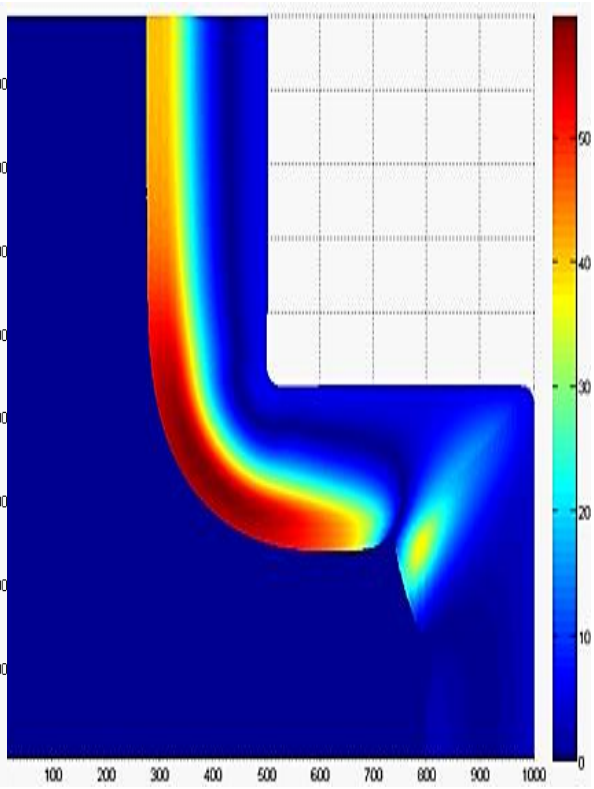

Figure 6.20
Relative error of the losses in %

Lateral extrusion $a = 9$[mm]

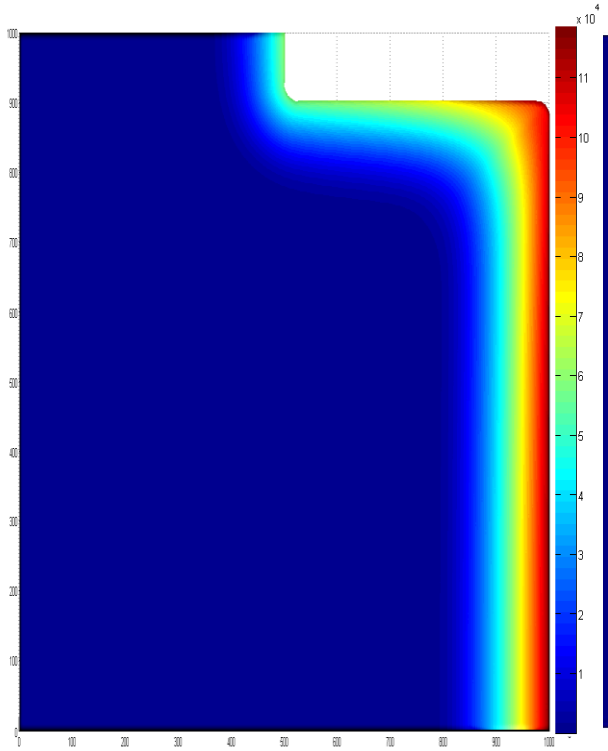

Figure 6.21
specific losses [W/kg] in the time study

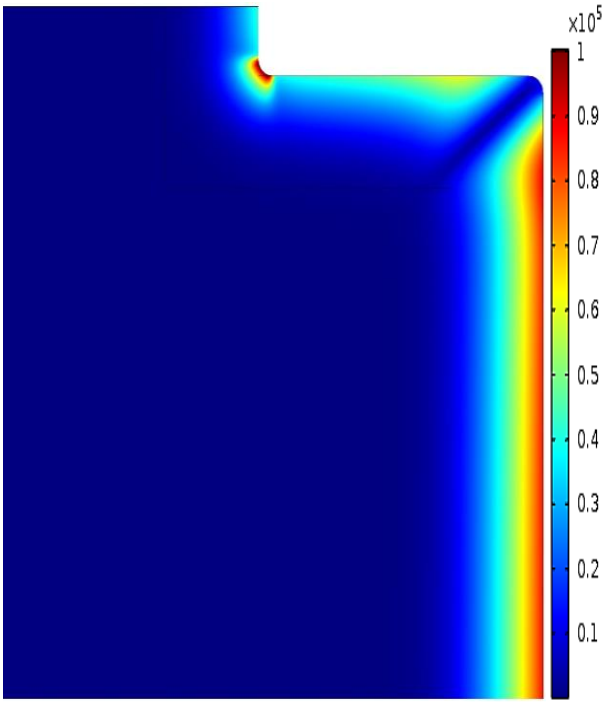

Figure 6.22
Absolute value magnetic field [A/m]

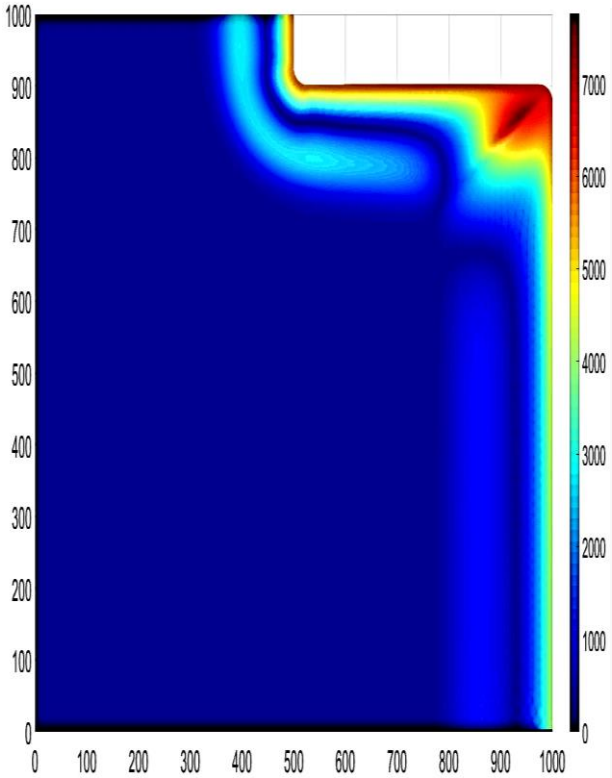

Figure 6.23
Absolute error between the losses [W/kg]

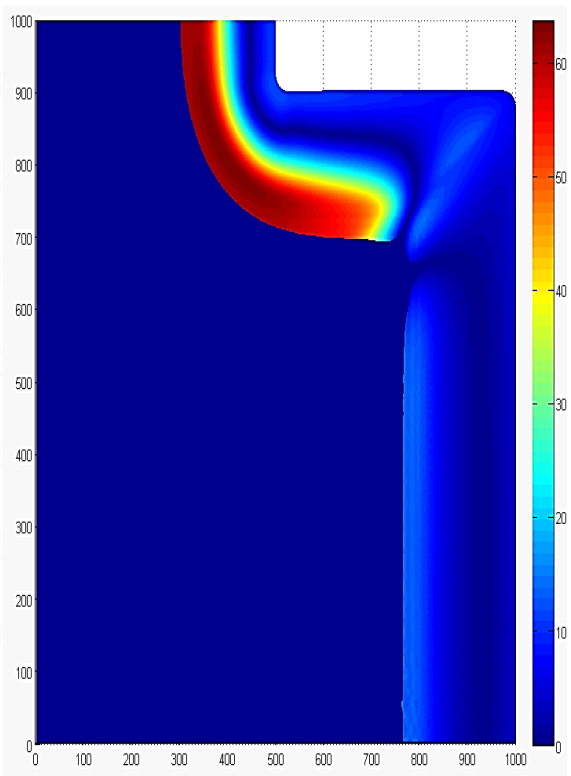

Figure 6.24
Relative error of the losses in %

To plot the images, the data are collected in a regular grid made of 1000x1000 points: the number of points was decided to obtain a good accuracy of the space of interest. Moreover, the full scale values are the same for every group of images, so it is possible to describe the general results just giving a first sight.
As concerning the specific absorption rate the full scale value is $12*10^4$ [W/kg], the value for the magnetic field is $1*10^5$ [A/m], that is equal to the value of the exciting field H_0. The full scale value of the absolute error between simulations in time domain and with PE model is 8000 [W/kg], instead the image of relative error has a maximal value equal to 60%.
According to the images of the absorption rate for all the parameters we can notice that the maximal values are concentred on a thin layer of the external surface and of the convex corner (i.e. the area that are closer to the exciting magnetic field).
Substantially, the absolute error is confined along a sensible region that is near the convex corner.
However, this error becomes smaller in relative terms. As a matter of fact, when we give a look to the figures of the relative error we see that, in the regions where the maximal losses are greater, the relative error is smaller than 2% and it increases a little bit in the corner region. The relative error assumes unacceptable values far away the surface, where the losses are almost nihil.
The images illustrating the distribution of magnetic field show that the current induced by the external magnetic field generates a second magnetic field that superimposes to the first one.
This results in a phenomenon known as **demagnetizing effect**: the areas near the corner are the ones mostly affected by this effect.
Nevertheless, the most interesting thing to observe is the correlation between the magnetic field induced in the steel workpiece and the absolute error.
As *Figure6.25* shows, inside the red ellipse we have the greatest error and a magnetic field that is more or less one order of magnitude smaller than H_0 (amplitude of the exciting field, used in the calibration problem too). The green ellipse in the middle of the sample shows that the magnetic field is almost equal to H_0 used in the calibration problem.
The reason why so many importance is given to the correlation between demagnetizing effect and absolute error is because it can explain the behaviour of the results. As a matter of fact, recalling the *Figure5.4,* we can notice that the value of the magnetic field chosen for the calibration problem has a key role. The equivalent BHcurve, used in the PE simulation, changes according with the amplitude of the magnetic field.

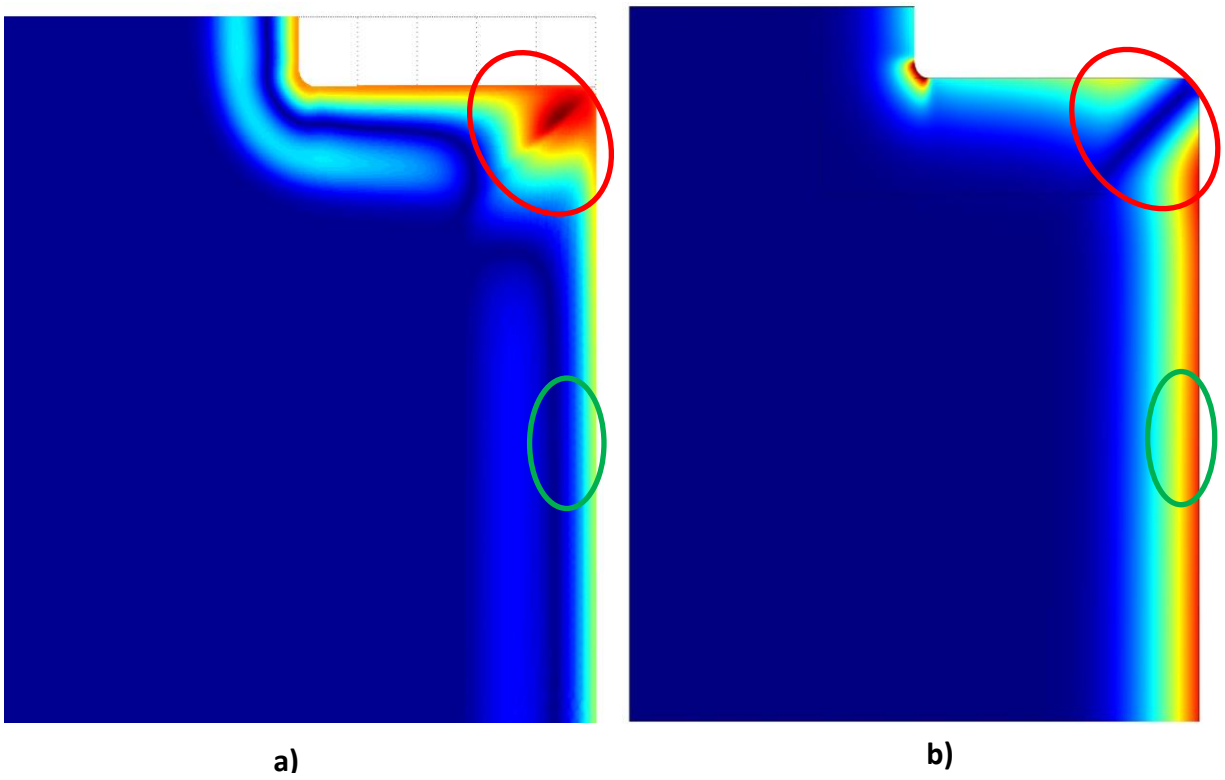

Figure 6.25
Correlation between absolute error **a)** (the figure on the left) and magnetic field **b)** (on the right side), two regions are evidenced by a red and a green ellipse.

Where the magnetic field decreases, because of the demagnetizing effect, we should take into account an equivalent curve with a smaller peak that, consequently, has a minor harmonic content. It means that we should have used a curve less altered and more similar to the reference one.
In the convex corner, the greater number of harmonics considered produced an overestimation of the PE' s losses compared to the time domain simulations. Instead, when the magnetic field increases we see that the absolute and relative error remain bounded. This is due to the
fact that equivalent BHcurves have an asymptotical value for high values of magnetic field. Therefore, the PE model shows a more remarkable sensibility in case of lowered magnetic fields.
These considerations are very useful because, anticipating some results, we will find the same characteristics in the next paragraphs and chapters.

6.3 Test case 3: 2D axial-symmetric geometry

The last test case provides a comparison between time domain simulations and harmonic domain simulations (solved with the PE model) in a 2D axial−symmetric geometry. This geometry is used for the heating process of the steel disc, so the modelling of the physics is crucial for the next steps.
In this paragraph, we are going to analyse the behaviour of a sphere immersed in an alternating uniform magnetic field, with a parametric study of the sphere' s radius "R".

Radius	Value	Unit
Radius_1	1	$[mm]$
Radius_2	3	$[mm]$
Radius_3	5	$[mm]$
Radius_4	7	$[mm]$
Radius_5	9	$[mm]$
Radius_6	15	$[mm]$
Radius_7	25	$[mm]$
Radius_8	40	$[mm]$
Radius_9	50	$[mm]$

Table 6.2 Parametrization of Radius in Test case 3.

The parametric sweep moves from a dimension of 1 [mm] until a dimension equal to the one used for the calibration problem and comparable to the real dimension of the steel disc.
In the figure below is represented the sphere with its boundary conditions. Even if we study a sphere, it is possible to represents the problem in a 2D plot because of the symmetric axes. The rotation axis coincides with the ordinate one (z *axis*): here is applied a Neumann condition on the zeta component of the magnetic field. Operating in this way the z *axis* not only is the symmetric axis for the geometry but also for the physic model. To the usual 2D axial−symmetric geometry, another symmetric axis is added thanks to the simple geometry that we are going to study. Implementing as much axes of symmetry possible is always a suggested choice: it allows to reduce the computational time.
The radial axis r that represents the abscissa axis in the image works as reflection plane. Along that line, it is imposed a Dirichlet boundary condition that poses the radial component of the magnetic field equal to zero. It means that the magnetic field is completely perpendicular to that axis. Therefore, imposing the same condition on the top segment that closes our study region it means that we are considering an area where the magnetic field is uniform. Finally, imposing on the last side another

Dirichlet condition we can assure that the magnetic field in the region analysed not only is uniform, but also it is an alternating sinusoidal field.

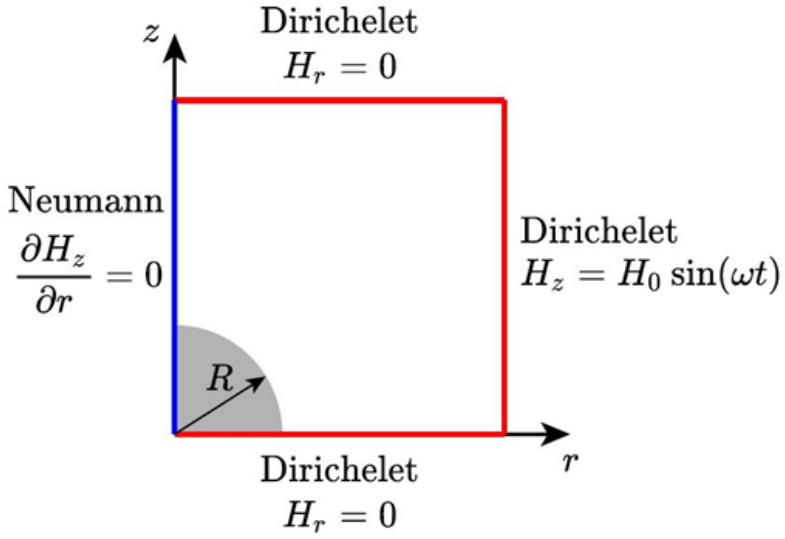

Figure 6.26 Test case 3: 2D axial−symmetric geometry. Study of a sphere with a parametrized radius. In the image are evidenced the boundary conditions.

The parameters that describes the properties of the medium and the exciting magnetic field are the same introduced in the previous test cases and summarized in the *Table6.1*. As concerning the mesh, it is utilized the same expedient of the inner virtual box with a finer mesh. In these simulations, a second sphere is built with a radius shorter of 8 penetration depths ($\simeq 2.5$[mm] using analytic expression (3.7)). The region included between the two spheres has a maximal element size of one quarter of penetration depth with a quadratic interpolation. Inside the inner sphere the mesh size grows with a rate of 1.5 until the elements reach a size of 2 [mm].

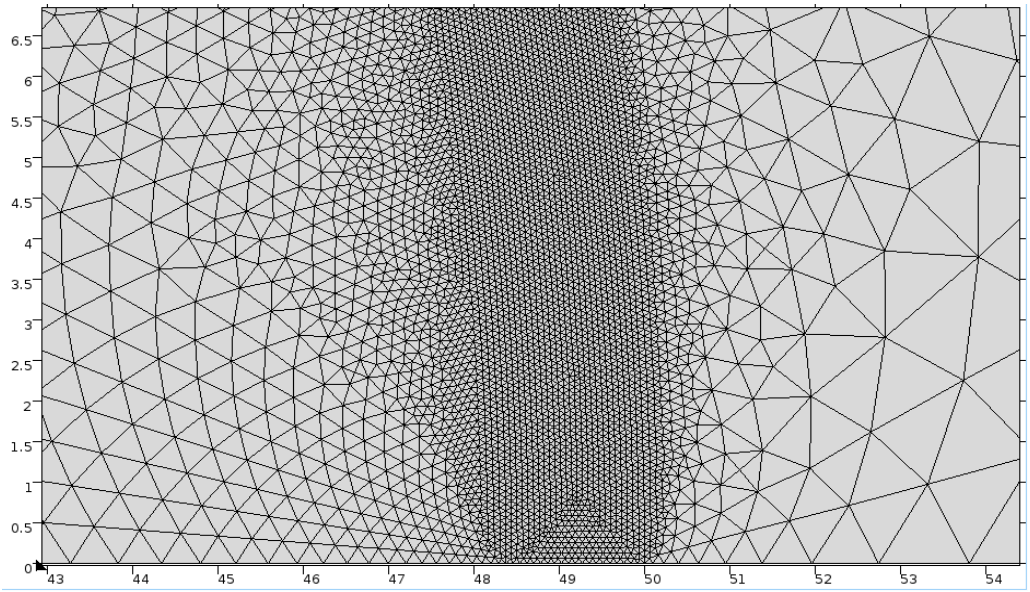

Figure 6.27 Mesh structure in Test case 3: 2D axial−symmetric geometry. View zoomed at the end of the radius of 50 [mm].

The simulations have a different physic depending on they are in time domain or in harmonic domain.
The time domain has a ***mf*** physic in COMSOL based on the magnetic potential and the reference BHcurve. As explained in the *paragraph* {1.3}, the 2D axial–symmetric magneto quasi static formulation introduces some simplifications.
The harmonic formulation is synthesized in this table:

General PDE equation
$e_a \frac{\partial^2 \boldsymbol{u}}{\partial t^2} + d_a \frac{\partial \boldsymbol{u}}{\partial t} + \nabla \cdot \Gamma = f$ $\mathbf{u} = [\mathrm{H_r}, \mathrm{H_z}]$ $\nabla = \left[\frac{\partial}{\partial \mathrm{r}}, \frac{\partial}{\partial z}\right]$
Conservative flux
$\Gamma = \mathrm{r} * [(0, \mathrm{E_\varphi}); (-\mathrm{E_\varphi}, 0)]$ [V]
Source term
$f = \begin{matrix} r * -j\omega\mu(\boldsymbol{H})\boldsymbol{H_r} \\ r * -j\omega\mu(\boldsymbol{H})\boldsymbol{H_z} \end{matrix} \quad \left[\frac{V}{m}\right]$
Dampingand mass coefficient
$e_a = 0; \;\; d_a = 0$
Global Variables
$\mathrm{E_\varphi} = \rho J_\varphi$ [V/m]
$J_\varphi = \left(\frac{\partial H_r}{\partial z} - \frac{\partial H_z}{\partial r}\right) \quad \left[\frac{A}{m^2}\right]$
$\boldsymbol{H} = sqrt(realdot(Hr, Hr) + realdot(Hz, Hz))$ [A/m]

Table 6.3 General PDE equation and its variables.

Before comparing the results of the simulations and discuss them, it is relevant to specify an aspect related to the visualization of the results. Because of all the symmetric planes it is possible to analyse the workpiece only in a quarter slice of a circle. Indeed, the rotational symmetry allows us to analyse the results along a plane that cuts the sphere while the reflection plane permits to show the results only on a quarter of the circle.

The first result discussed is the comparison of the specific losses between time and harmonic domain with the parametrization of the first five radiuses.
The distribution of the losses is plotted in a cut–line that has a length of 5 millimetres and starting from the external surface of the sphere moves forward the core of the sphere along the radial axis (i.e. along the middle plane of the sphere).

The results show an inacceptable pattern match, where the curves are detached for all the radiuses.

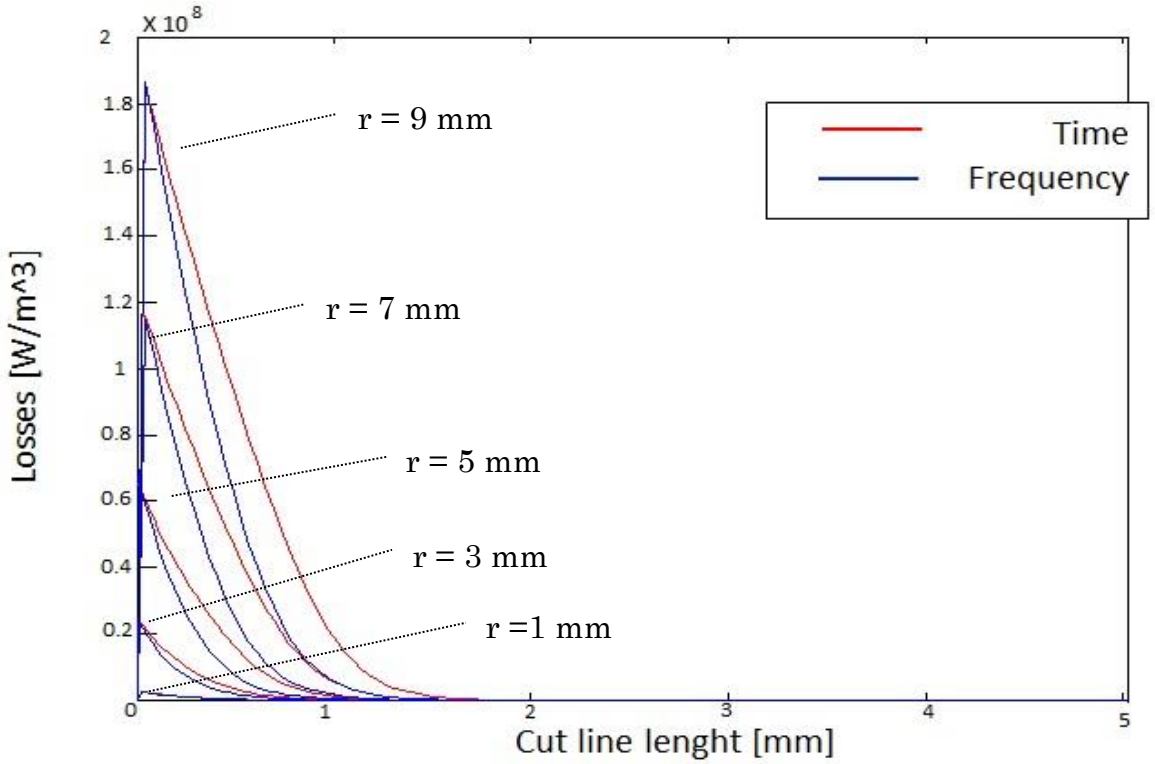

Figure 6.28 Distribution of the losses along the cut-line for the parametrization of the radius from 1 to 5.

The motivation that explains this behaviour was already introduced in the previous paragraph: it is the demagnetization effect and the reduced geometric length that drift apart the simulations from the calibration problem. As a matter of facts, if the maximal values assumed by the magnetic field are plotted in function of the radius it is observed that the geometry and the demagnetization effect play a key role.

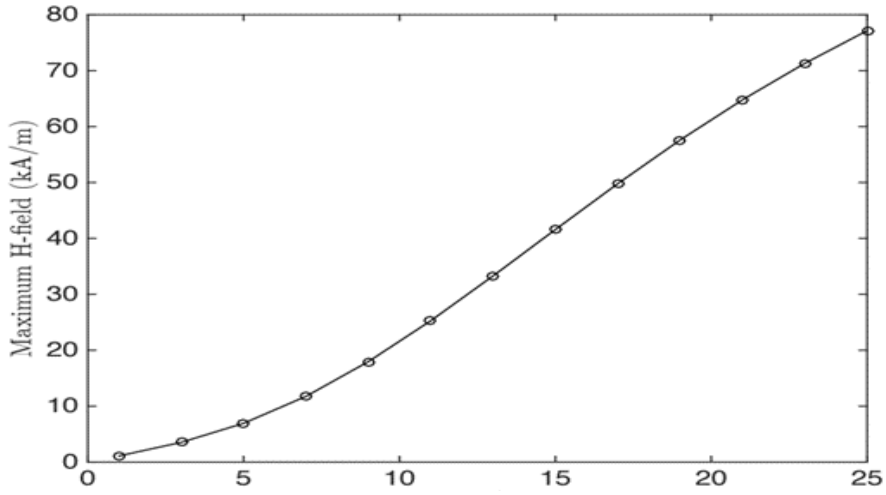

Figure 6.29 Maximum value of magnetic field in function of radius size.

As a reproof of this, another simulation is run, changing the equivalent PE curve and choosing 25 [kA/m] instead of the usual 100. In the figure below are plotted not only the distribution of losses in time domain, but also the ones in the harmonic domain with the PE from the calibration problem and the modified one.

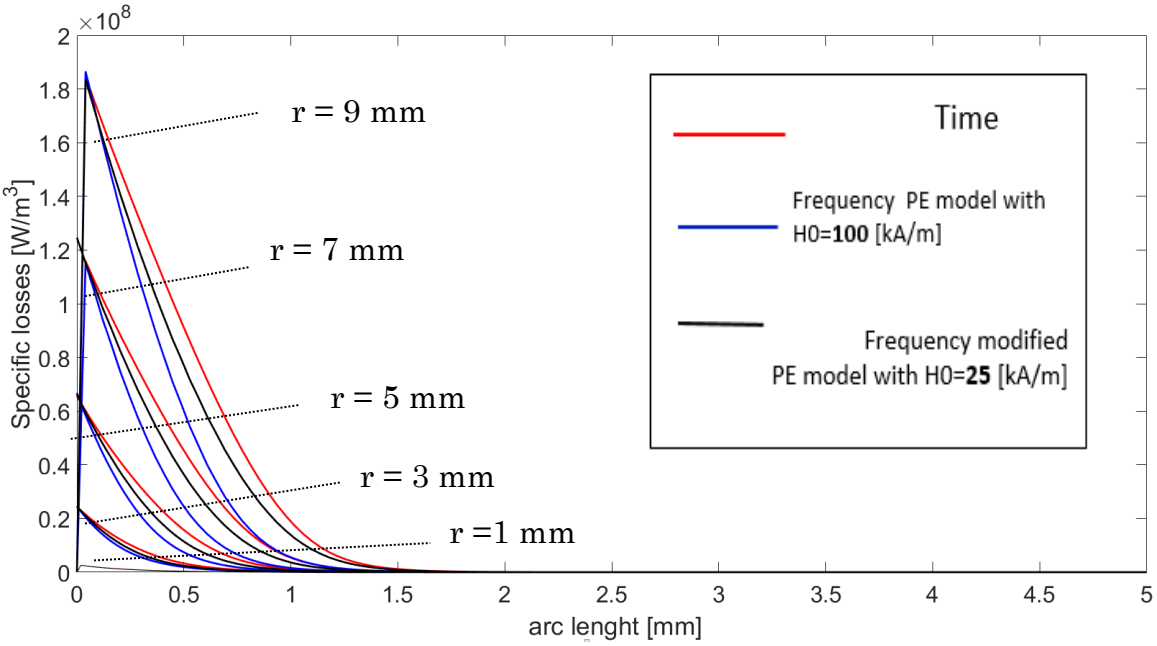

Figure 6.30 Distribution of the losses along the cut−line for the parametrization of the radius from 1 to 5. The red line are the time losses while the blue and black lines are the harmonic losses

As *Figure6.5* shows, the equivalent BHcurve modified raised the accuracy between the time domain simulations and the frequency domain ones. However, acceptable matching is not yet achieved because we should have run a more precise calibration problem (e.g. for the sphere with r=9[mm] the maxim value of magnetic field is 18and not 25[kA/m]).

Nevertheless, let us focus on the second part of parametric study because they have a bigger radius and are more similar to the real process of induction heating.
Increasing the radius, a better pattern match is achieved because the simulated geometries get closer to the calibration problem and the proper value of magnetic field.
Now, thanks to the experience maturated with all these tests, the analyses of results related to the sphere with the longest radius can be developed. From these preliminary observations indeed, emerges that it is the case with the closest equivalent model to the calibration problem and to the hardening process.
The first graph presented (*Figure 6.32*) is the distribution of the specific losses [W/m^3] in the quarter slice of the sphere. The data, extracted from the time domain simulation, are plotted in a regular grid made of 2000x2000 points.

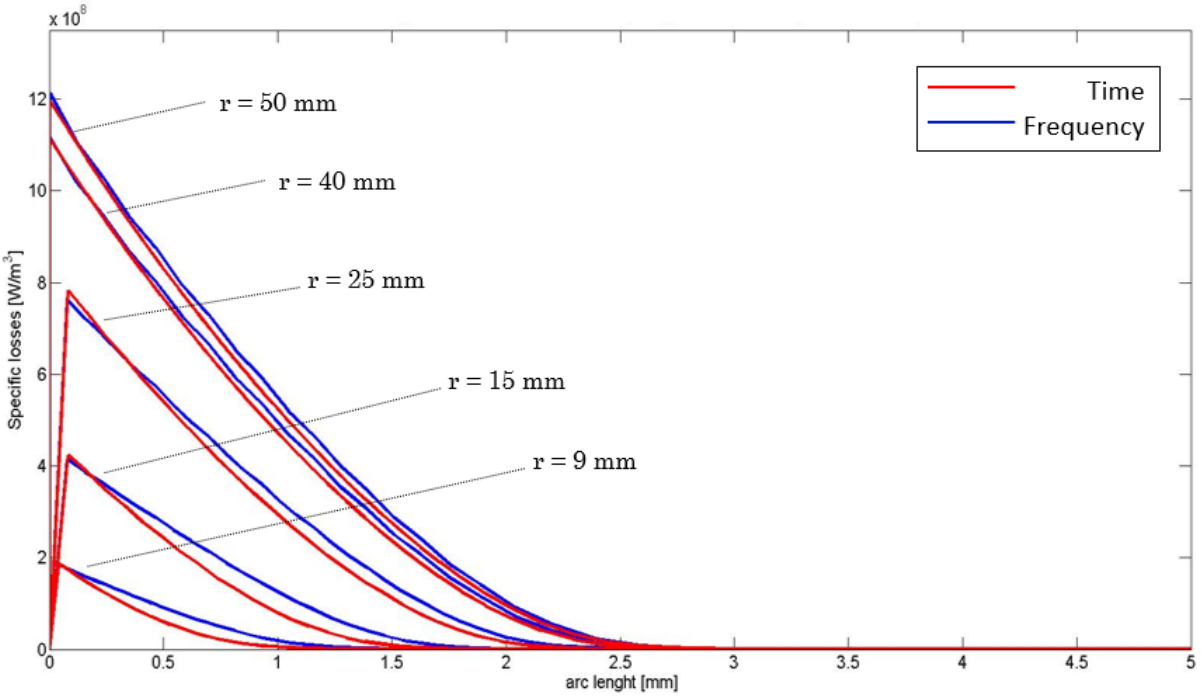

Figure 6.31 Distribution of the losses along the cut-line, from 5th to 9th parametrization of the radius.

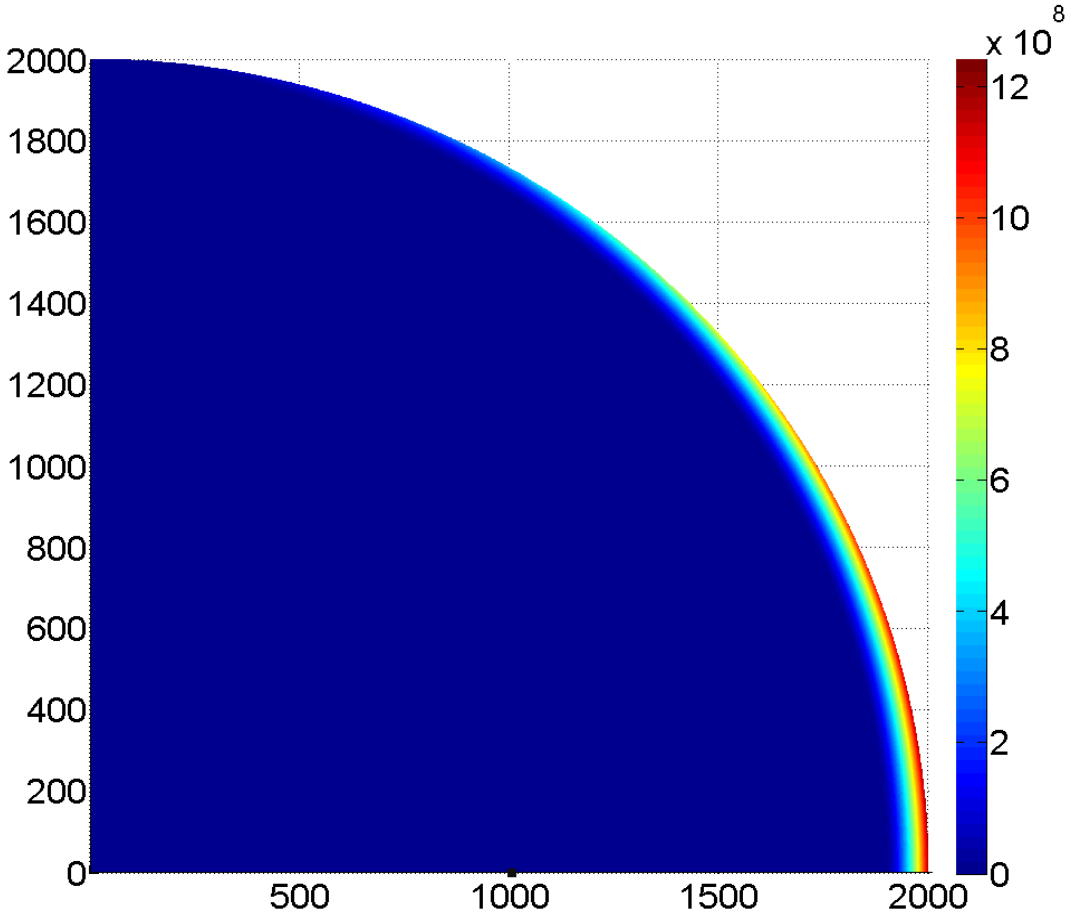

Figure 6.32 Distribution of the specific losses [W/m^3] for the sphere with R=50[mm]. The plotted data refer to the quarter slice of the time domain simulation

As *Figure 6.32* shows, the losses are concentrated in the centre of the sphere and then they decrease progressively approaching to the upper part of the sphere. To analyse this behaviour, two cut–lines are built. The upper one has a length of 5 millimetres, is parallel to the radial axis and it is posed at an ordinate of 40 millimetres. The bottom cutline is realized along the radial axis, starts on the sphere's surface and penetrates for five millimetres.

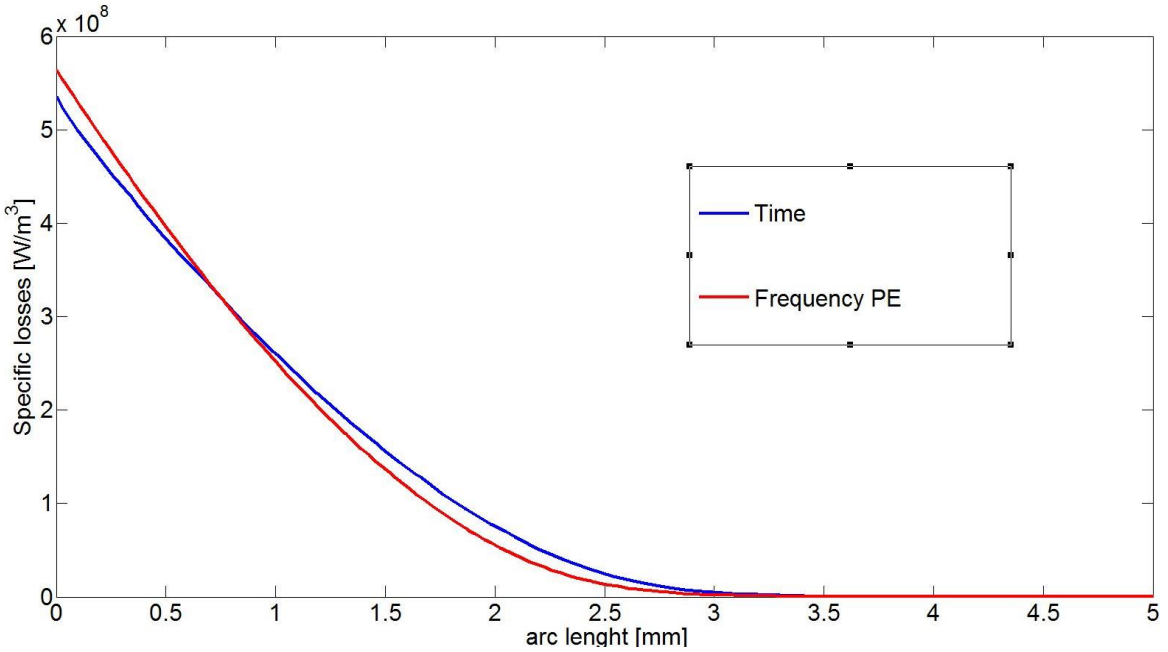

Figure 6.33 Distribution of the specific losses [W/m^3] along the **upper** cutline, with ordinate equals to 40 [mm]. The sphere has Radius_9.

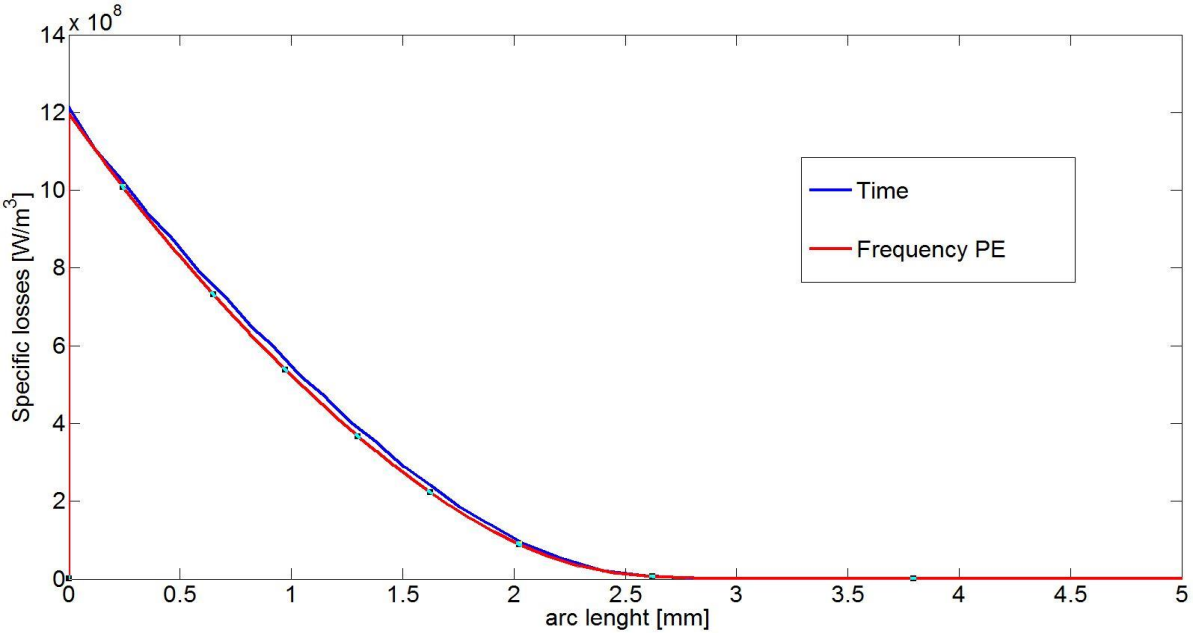

Figure 6.34 Distribution of the specific losses [W/m^3] along the **bottom** cutline, with ordinate equals to 0 [mm]. The sphere has Radius_9.

Once again, in the figures the red lines indicate the losses collected from the time domain simulations while the blue ones the frequency simulations made with the PE model. Comparing the two plots, not only is found a confirmation of the different maximal values of the losses but also, they provide the evidence that along the bottom cutline there is a better matching compared to the upper one. In order to quantify the accuracy of the new model in relation to the time simulations, a new dimensionless parameter is introduced. It is named ***ratio*** because indicates the average ratio between the absolute error of losses and the value of the losses along the cutline.

$$\boldsymbol{ratio} = average\left(\sum_{x=0}^{L}\left(\frac{absolute\ error(x)}{losses_{time}(x)}\right)\right) \tag{6.1}$$

In the expression x is the dimensional variable that extends from the sphere's surface (x=0, beginning of the cutline) until the end of the cutline (x=L).
The losses considered in the denominator are the reference ones of the time domain simulations. Besides, due to the fact that the parameter is dimensionless but it is similar to a relative error we are going to give the percentage value.

–	Upper cutline	Bottom cutline
L=5[mm]	23.28%	2.19%
L=0.75[mm]	3.55%	0.77%

Table 6.4 Values of the parameter "*ratio*".

However, the parameter does not draw accurate conclusions for the overall behaviour of the model. As a matter of fact, the parameter does not provide a weighted average: for the upper cutline it shows an elevate value because it takes into account the relevant relative error between the two models used. So, as to find a more substantial value, the same parameter has been calculated in a shorter portion of cutline: more or less one penetration depth of the power lost.
The values are more meaningful but there is still a marked difference between the two cut-lines, in particular the new equivalent model overestimates the losses in the upper cutline.
As it was operated in the previous test case, in the following page is reported the 2D plot group that presents: the absolute error, the relative error and the distribution of the magnetic field in the quarter slide of the sphere.
The first image illustrates how the absolute error has its maximal values in the centre of the sample, in correspondence of the radial axis. This is due to the fact that, in the same area is localized the maximum of power lost. It is more interesting indeed, to observe the second image where there are the relative errors.
In a thin surface layer, the relative error is bounded with a rough value lower than five percent.

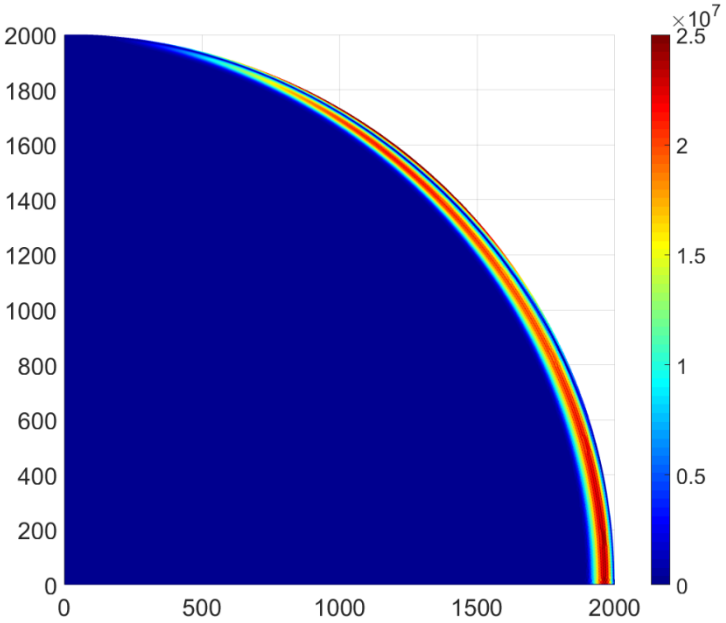

Figure 6.35 Distribution of the absolute error [W/m^3] between time and harmonic with PE model simulations.

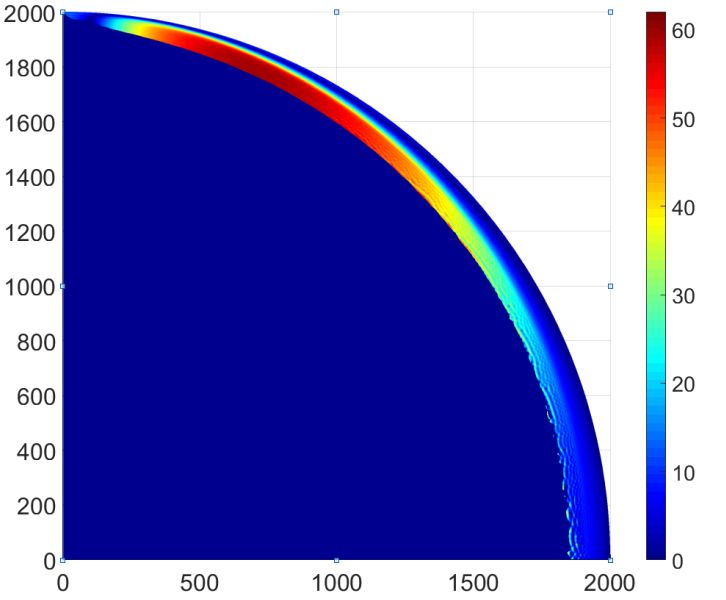

Figure 6.36 Distribution of the relative error in % between time and harmonic with PE model simulations.

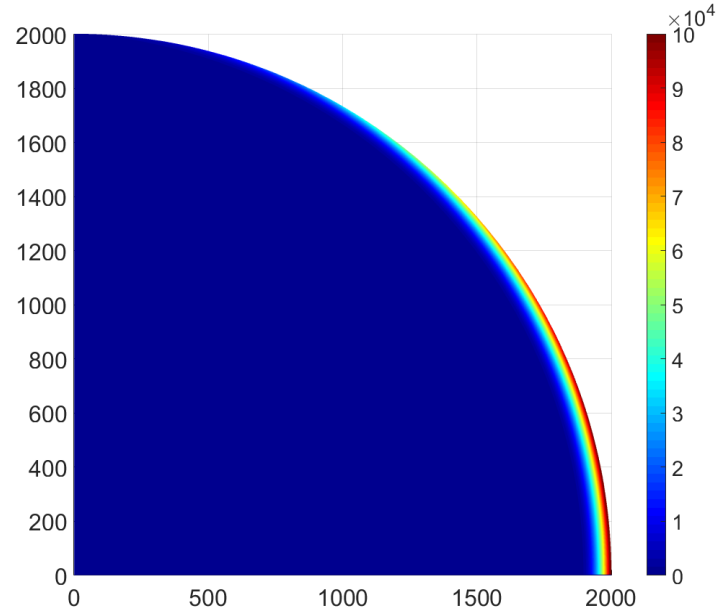

Figure 6.37 Distribution of the magnetic field [A/m] in the sphere's quarter slice.

Moving forward the core, the values raise and achieve huge percentages. The area near the top of the sphere is particularly afflicted by this growth.
Finally, there is the distribution of the magnetic field in the workpiece. Because of the demagnetization effect, the magnetic field decreases not only inversely correlated to the radius, but also along the surface: from the centre of the sphere to the top part. Therefore, comparing the distribution of the magnetic field with the relative error, the modifications of the new equivalent curve in function of H_0 emerges.
In conclusion, it is notable that the behaviour of the model is, once again, tied to the calibration problem and the value assumed by the magnetic field.

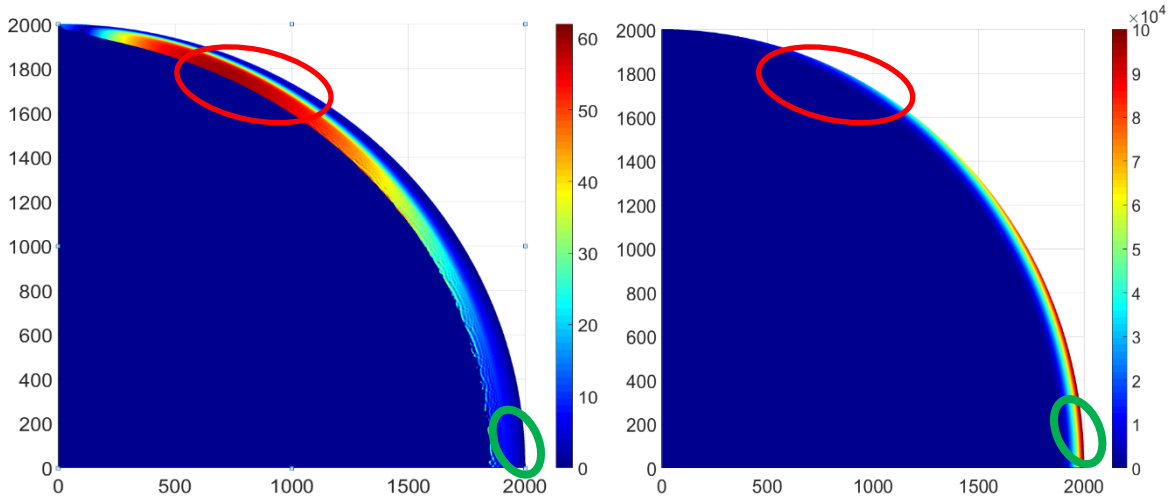

Figure 6.38 Correlation between the relative error and the magnetic field values in the Test case 3. Two elliptical regions are evidenced.

As a friendly reminder to these comments, the *Figure5.4* is replotted.

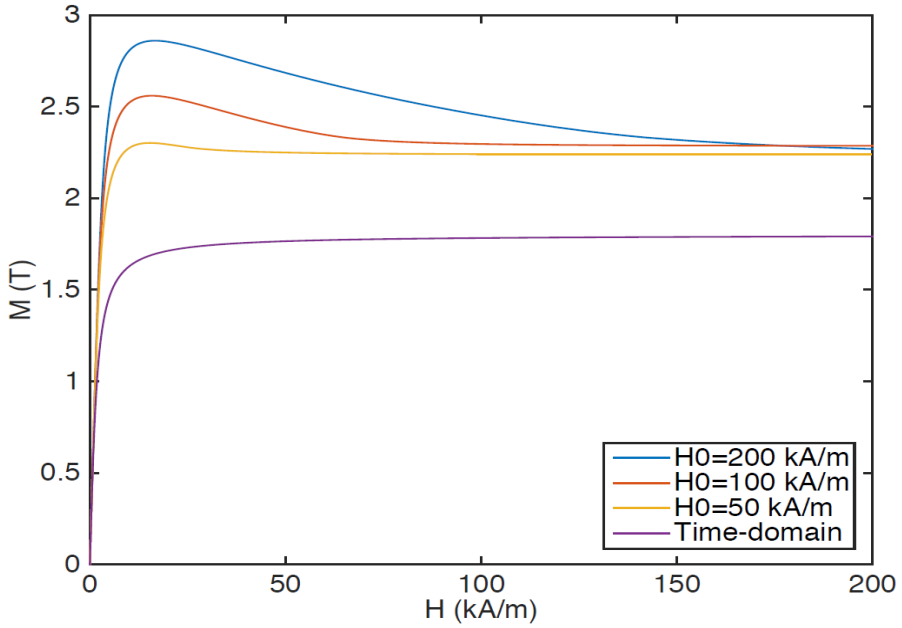

Figure 5.4 BH diagram where are plotted normalized magnetization curves. There are the reference curve and the new equivalent curves obtained with a parametrization of the external magnetic field H_0.

Chapter 7

Simulation of Induction Heating Process

In the previous chapter were presented some test cases referred to the electromagnetic steady state simulations: the errors, related to the application of the new PE model, are mostly concentrated in the region where the magnetic field diminishes. Because these errors can be considered acceptable, and the new equivalent model has a particularly good approximation in the region with the greatest power lost, it is more interesting to study thermal and electromagnetic problems coupled in induction hardening process.

However, in the multiphysics simulation, only one part of the induction hardening process is taken into account: the induction heating. Hence, the complexity of the simulation is gradually increased, besides the application of the new Power Equivalent model concerns only the electromagnetic process and not the thermal (e.g. quenching and tempering treatments).

7.1 Description of simulation model

The steel workpiece chosen to be heated by induction is a disc because it is the simplest geometry that can be dealt with in 2D axial−symmetric simulation.
In the image below it is possible to see in blue the steel disc, the copper coil in orange and two cut−lines along whom some data will be collected.
Thanks to the symmetrical geometry presented by the disc we can still apply the rotational plane to reconduct the study of the 3D geometry into a 2D geometry; moreover another symmetry plane is introduced in correspondence of the radial axis in the centre of the sample in order to halve the geometry and the number of elements.
As *Figure 7.1* evidences, there are two particular air areas: one is included between the symmetry axis and the steel disc, and the second is inside the copper coil. The first one is the through hole for the driveshaft, while the second one is a region where flows water to cool down the inductor. The symmetric z−axis coincides with the Neumann condition imposed on the tangent component of the magnetic field. Along the radial−axis is imposed a Dirichlet conditions that bounds the radial component of the magnetic field equal to zero (it means that the magnetic field is orthogonal to the plane). In addition to these two conditions, seen in the *test case 3* too, we use a Dirichlet condition that imposes a null magnetic field. These conditions are imposed on the upper and right side of the domain: the exciting magnetic field is generated by the current flowing in the copper coil.

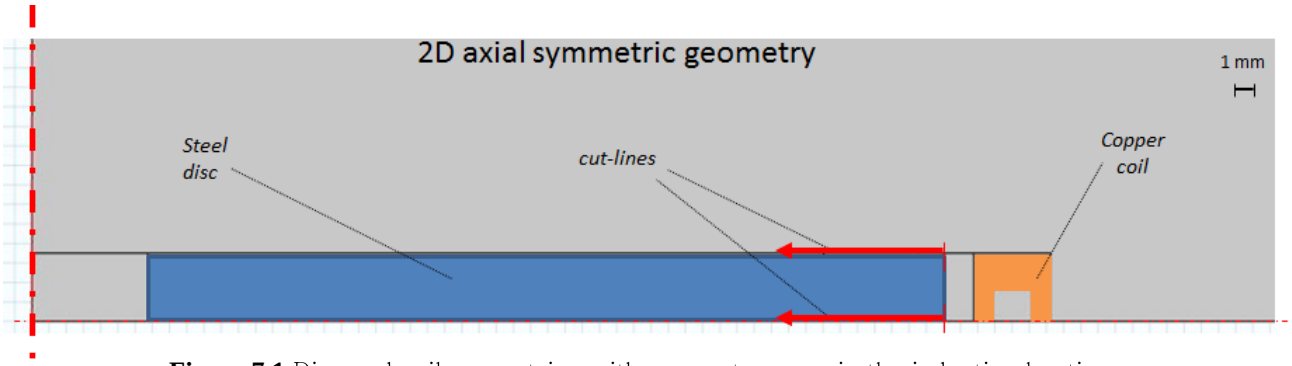

Figure 7.1 Disc and coil geometries with symmetry axes in the induction heating

All the geometrical and electrical parameters relevant to build the model are introduced in the following table. The thermal aspects were illustrated in the *Chapter {3}*.

Parameter	Symbol	Expression	Value	Unit
rho_steel	ρ_{steel}	$1/\sigma_{steel}$	$25e^{-8}$	$[\Omega * m]$
rho_air	ρ_{air}	$1/\sigma_{air}$	$2e^{-2}$	$[\Omega * m]$
Maximal magnetic permeability	μ_{r0}	–	600	-
frequency	f	–	$190e^{-3}$	$[Hz]$
period	T	$1/frequency$	$5.26315e^{-6}$	$[s]$
Treatment time	T_{total}	-	0.1	$[s]$
radius	r_{disc}	-	$53.05e^{-3}$	$[m]$
height	h	-	$7e^{-3}$	$[m]$
Driveshaft radius	$r_{driveshaft}$	-	$6.75e^{-3}$	$[m]$
External coil radius	r_{ext}	-	$59.25e^{-3}$	$[m]$
Internal coil radius	r_{int}	-	$57.75e^{-3}$	$[m]$
Air gap	air_{gap}	-	$1.7e^{-3}$	$[m]$
Penetration depth	δ	$\sqrt{\frac{2\,\rho_{steel}}{\omega\,\mu_0\,\mu_{r0}}}$	$2.357e^{-5}$	$[m]$
Current	I_{coil}	-	1250	[A]

Table 7.1 Parameters used in the induction heating simulation.

Particularly relevant is to note that frequency is drastically raised to 190 [kHz] and the root mean square of the current is 1250[A] (2500 in the whole coil). These peculiar values are chosen because they are the same values used to analyse the hardening process of a similar disc in the electrothermic laboratory of ÈTS. However, the simulations that are going to be run, differentiate from the real hardening process for two aspects. Firstly, the total time of the experimental treatment is not 0.1[s]: this value is arbitrarily chosen. It is the shortest possible in order to limit the computational time of the whole simulations, but the treatment has to last until the

sample oversteps the A_3 transformation temperature. Secondly, this simulated treatment is a **current control** process. Usually, hardening processes are realized in power control, so this work condition is uncommon. However, a current control process that maintains unaltered the amplitude of the current during the process, produces an unaltered exciting magnetic field. Therefore, we are hypothesizing an intermediate situation which is absolutely necessary to study the behaviour of the PE model. In the mentioned situation exists an alternating sinusoidal magnetic field generated by a current flowing in a single−turn coil.

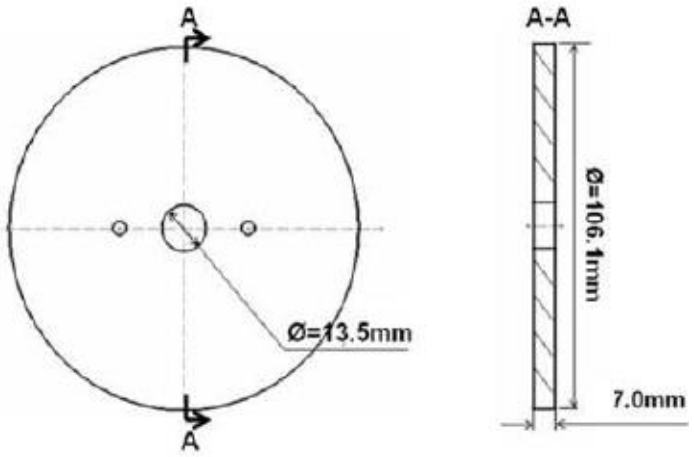

Figure 7.2 Disc and its geometry.
Larregain, B., et al., *Method for Accurate Surface Temperature Measurements During Fast; Induction Heating.* Journal of Materials Engineering and Performance, 2013. **22**(7): p. 1907−1913.

Mesh

The FEM models used in COMSOL present several virtual boxes used to regularize the mesh structure. Talking about induction heating it is relevant to have a fine mesh in the first penetration depths of the medium. However, because of the thermal process and the rise of the penetration depth, a finer mesh was built in a thin layer of one millimetre that corresponds to the desired hardened layer.

As *Figure 7.3* shows the fine mesh virtual box follows the shape of the disc and covers the upper part of the disc too, for a length of seven millimetres. The reason of this choice is related to the proximity effect born between the inductor and the ferromagnetic disc: the proximity of corners steeply modifies the magnetic flux lines that close their loop through the air gap.

The fine layer has elements with quadratic interpolation and a maximal size equal to the penetration depth calculated analytically. Moreover, another virtual box can be noticed in the air gap between the steel sample and the inductor. It is used to regularize the air elements with a maximal grow rate equal to *1.05*.

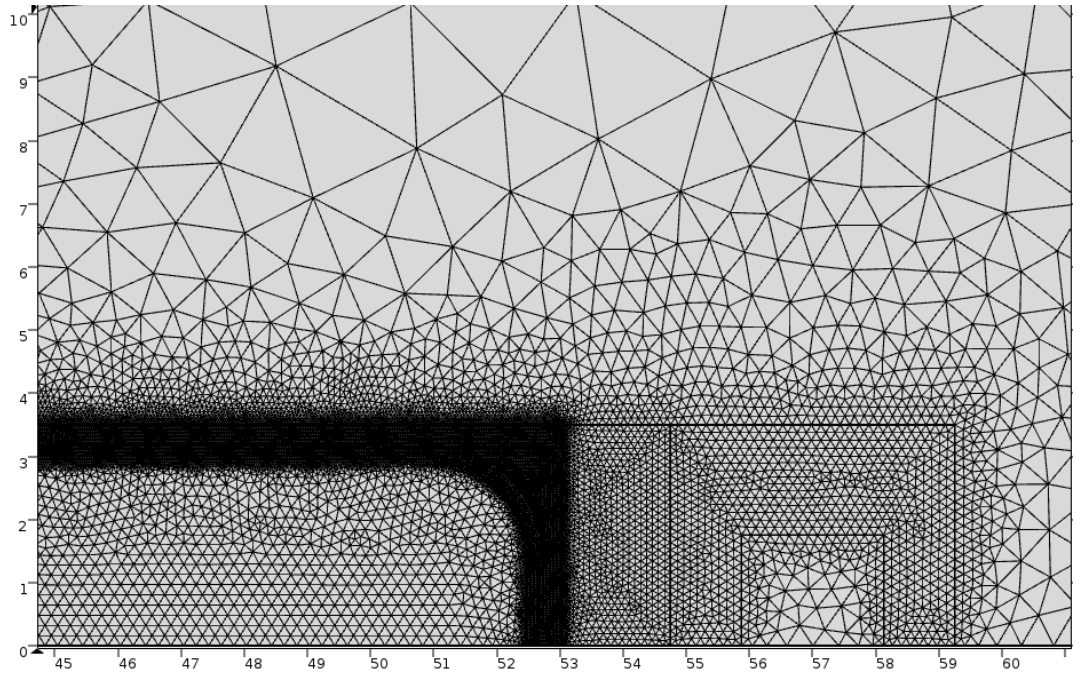

Figure 7.3 Structure of the mesh in a zoomed view of the steel disc, air gap and copper inductor.

Magnetic permeability models

In the comparison between the simulation with the reference BHcurve and the new PE model, it is added a third simulation with a constant value of magnetic permeability.

Even if it is known that a constant value of magnetic permeability, that gives back a linear BH curve, is a bad approximation to describe the behaviour of a steel sample, it is still widespread.

As a matter of fact, especially companies and factories want to maintain the computational time cost as low as they can. Only recently, with the research and study of quality workpieces, the numerical simulations are leaving behind the constant magnetic permeability.

This thesis wants to demonstrate that the new PE model maintains a good accuracy of the results, comparable with the time domain simulations, combined with the fast-computational time of a linear frequency study. The simulation time of these three models is indicated to give an idea of the order of magnitude of the computational time cost. The constant magnetic permeability requires around thirty minutes (~1500 [s]), the new Power Equivalent model requires around two hours (~7000 [s]), while the time domain simulation requires almost one day (~100.000 [s]).

The simulations are run with the same simulation machine (16GB or RAM, processor Intel i7-6850K with a clock cycles of 3.4GHz) and the same number of elements (~50 thousands).

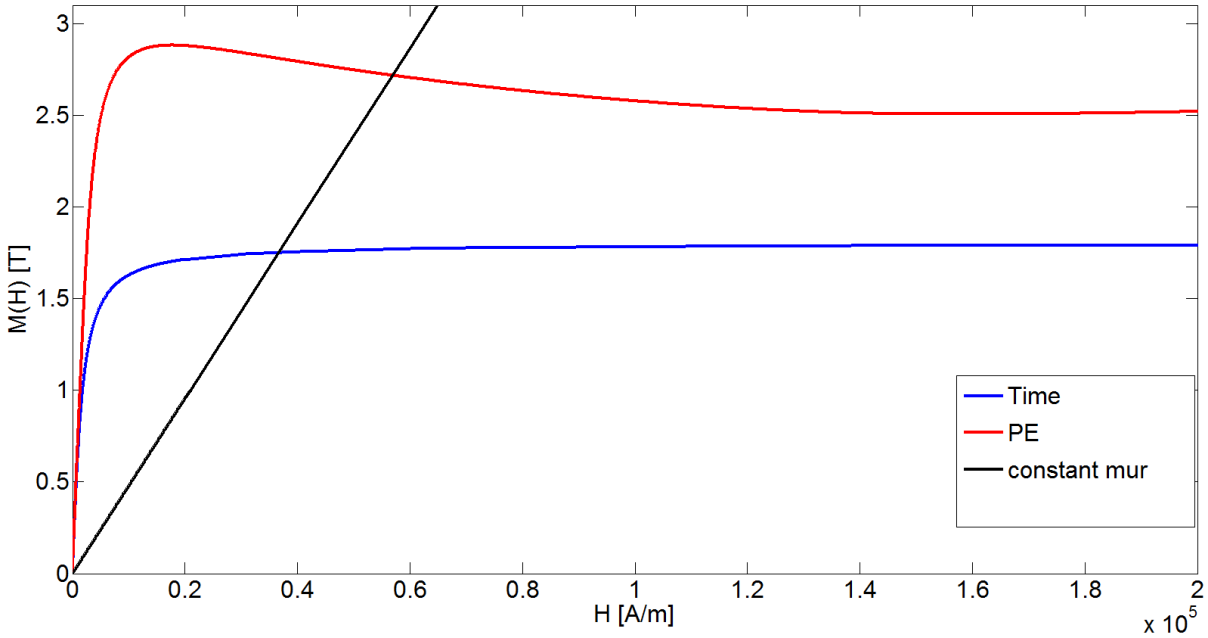

Figure 7.4 Magnetization in function of magnetic field, to plot the BHcurves. In blue there is the reference curve used in time domain simulation, then the red equivalent curve with H_0 =200[kA/m], finally there is the black line with μ =39.

As the figure above shows, the value for the magnetic permeability chosen for this application is 39. Usually values around 15 are used but they are chosen to maximize the accuracy of the temperature at the end of the process. This simulated treatment, not only is current controlled, but also it achieves that the processing time is shorter. Anyway, the value of 39 is chosen to minimize the error of the power lost in the sample, comparing the time domain simulation with the linear frequency one.
As a matter of fact, as the PE model is built to give the most accurate distribution of losses, the constant magnetic permeability is chosen to operate in the same way.

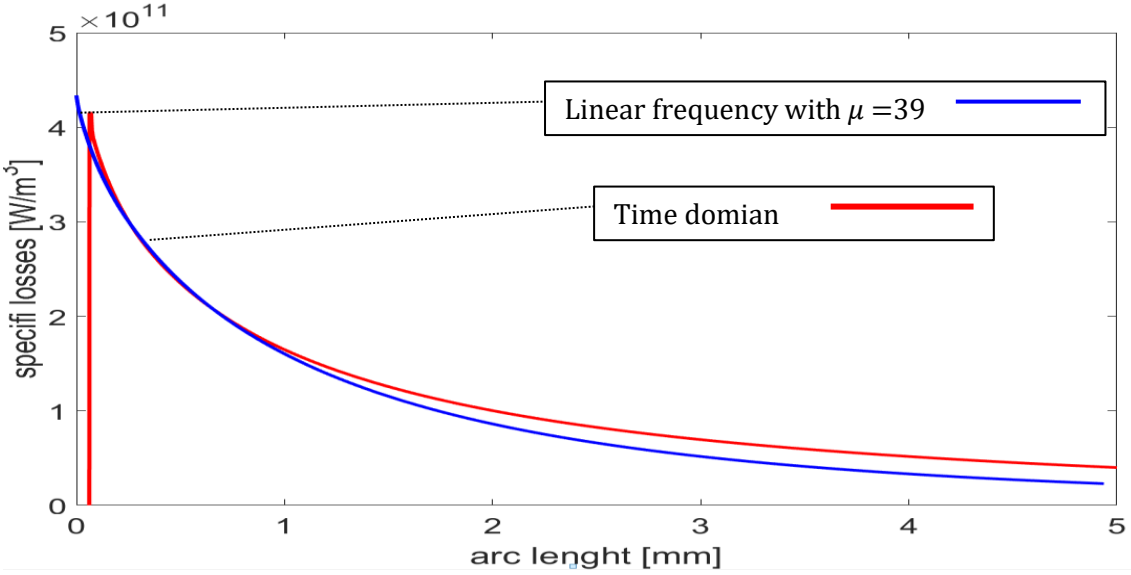

Figure 7.5 Power lost distribution along the middle cut−line. In red the time domain distribution, in blue the frequency one with μ =39. The accuracy and the good pattern match is researched in the first millimetre.

Coupling and Solvers

The coupling between the two physics is performed through the temperature distribution in the disc and through the heating power. This is numerically computed thanks to the interface of COMSOL with MATLAB.
Starting from an initial condition of uniform distribution of temperature T= 20 [C°], the electromagnetic problem is solved. The computation of the electromagnetic problem has as solution the magnetic scalar potential. From the latter can easily be obtained the trend in time of the induced power. After that the power distribution in one electromagnetic period is integrated, it is exported and used as input data for the thermal process.
The numerical computation of the thermal problem has as solution the temperature distribution in the steel sample. This is useful to update the parameters of the material that are all in function of the temperature. The final temperature is exported to reinitialize the cycle for the successive step. Operating this kind of coupling, the heating process is subdivided in several time steps. Every time step is calculated by a customized code in order to bound the maximal temperature jump inside the whole workpiece in the interval of 30[℃] ± 15%. Therefore, all the non−linear properties of the medium are subdivided in small temperature intervals inside whom we can assume a linearized behaviour. The maximal temperature jump was chosen in order to have the biggest temperature jump possible, but small enough to have a good approximation during the steel transformations and Curie' s transition.

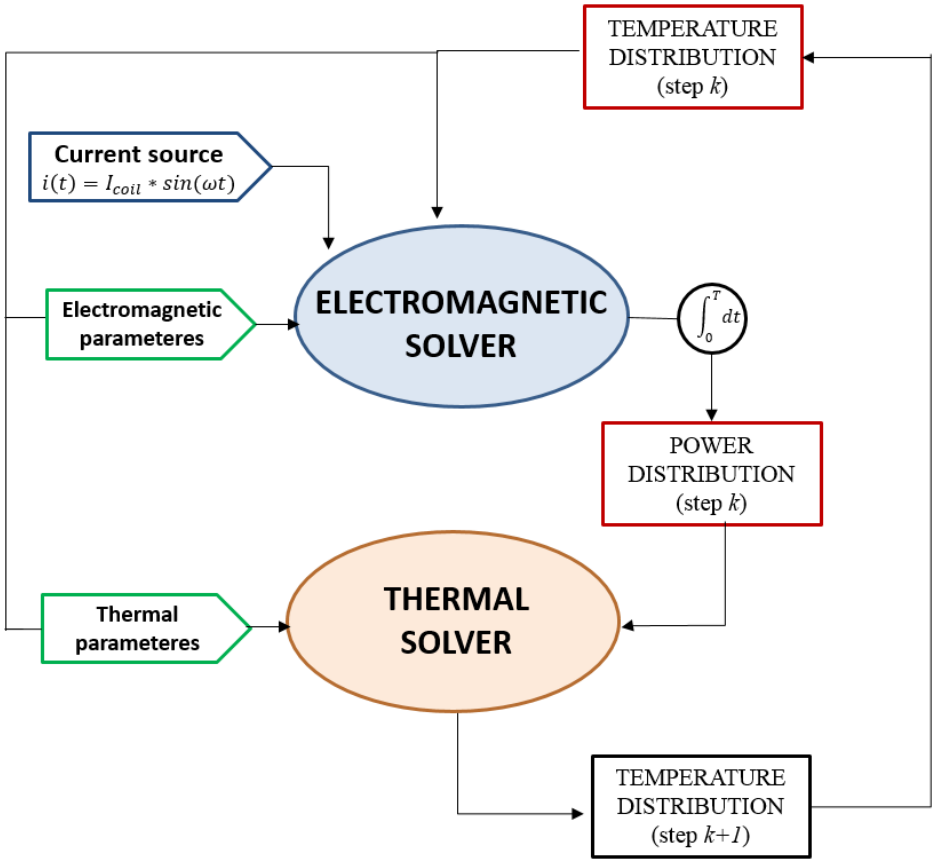

Figure 7.6 Flow chart of the electromagnetic model coupled with the thermal one.

The resolution of the electromagnetic problem is the more time-consuming part of the solution of the model. In fact, the magnetic non-linearity makes it very slow and costly resolution.
To ensure a convergence of the method and to obtain a solution, it was chosen a direct solution method. For the time-dependent solver it was chosen the Direct solver PARDISO with a BDF-strict, with a strongly nonlinear Newton-Raphson. The strict BDF means that the electromagnetic period is divided in small and equals steps; the electromagnetic period was divided in five hundred steps.
As concerning the frequency simulations with the new PE model and the constant magnetic permeability are adopted respectively a stationary solver and frequency-transient solver. In both simulations is used the Direct PARDISO solver with an automatic Newton-Raphson method to face the non-linarites.

7.2 Simulation Results

The results are divided in two main groups: the 1D plot group and the 2D plot group. The first result shown in this paragraph is the evolution of some isotherms obtained in the simulation along the upper cutline. This graph is shown as first because nowadays it is possible to follow the evolution of isotherms curves thanks to thermal lacquers. Among ÉTS, this is one experimental acquisition of data made in hardening process.
In the figure below, along the x-axis there is the time scale, while along the ordinates there is a length dimension: it corresponds to the depth where are found the temperature values.
Every colour corresponds to a different isotherm, while every geometric marker indicates a physic model. Focusing for one instant on the PE shapes (with the circular marker) of three and five hundred degrees, it is notable that they overestimate the power lost. For every instant the penetration depth is greater than the one found in the time reference model.
As an additional proof, the isotherm of 816 [C°] is retraced before the other ones.
In the image, there is a vertical green line, posed at 0.54 [s] to indicate the time when the Curie' s temperature is reached for the first time in the simulation with the PE model.
The curve obtained by the simulation with a constant magnetic permeability underestimate the losses, except for the isotherms of 816[° C] that has a good pattern match for a chance reason.

As the curve show, after the Curie's temperature, the slope of the PE isotherms changes and eventually they underestimate the final depth of temperature in the sample.
A possible reason of this behaviour for the PE simulation might be found in the deformations of induced magnetic field in the sample. From the test cases is known indeed how the PE model is sensitive in relation to the amplitude of magnetic field and the Curie's temperature has a primary role on this. The transition, from ferromagnetic material into paramagnetic medium, changes the equivalent reluctance seen from the inductor and consequently the magnetic field, induced by the constant current flowing in the coil, is deformed (*Figure 7.8 b)*).

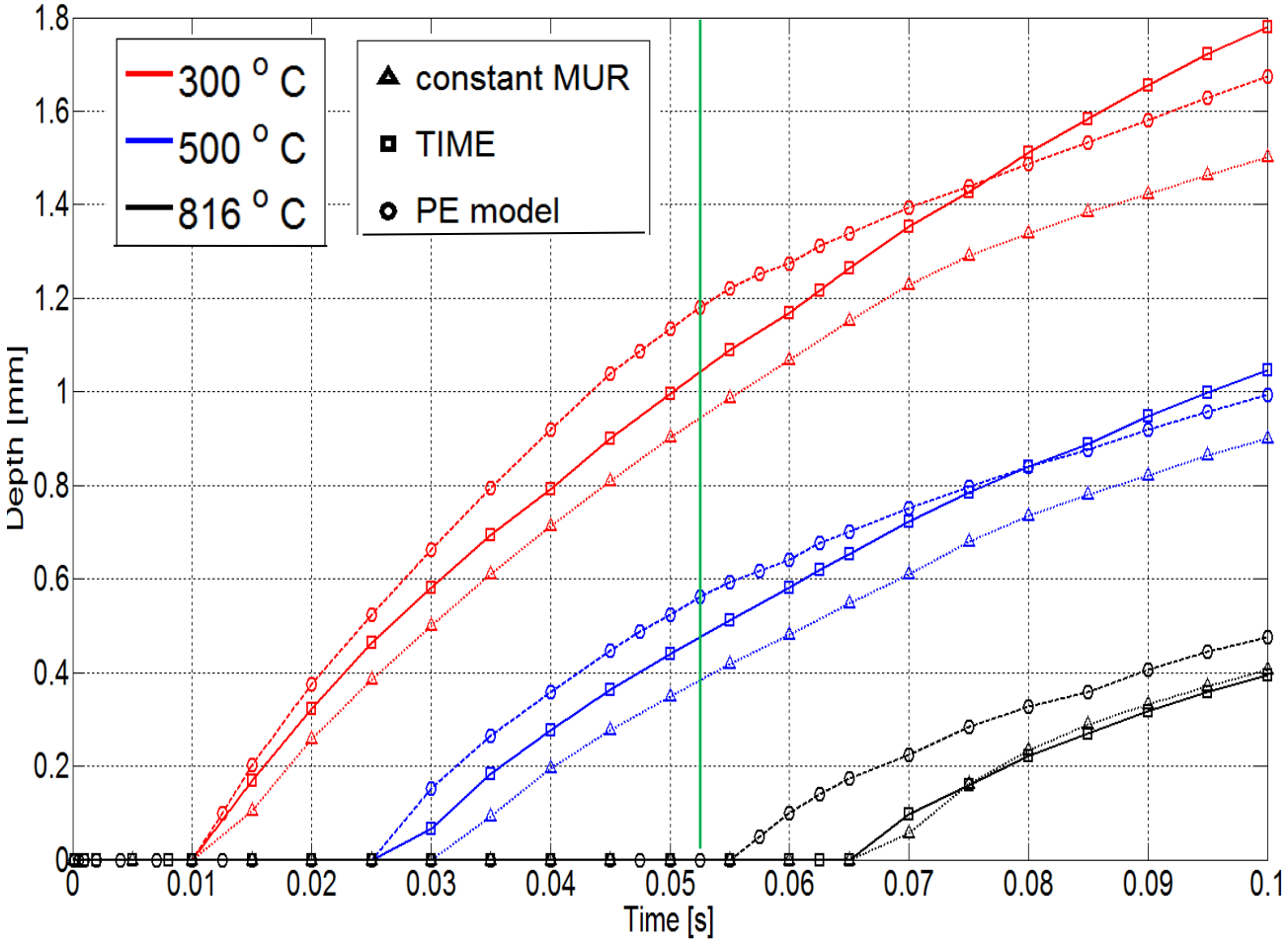

Figure 7.7 Evolution of some isotherms obtained in the upper cut−line, in the simulation of induction heating with current control.

The figure provides inconclusive evidences regarding the accuracy of the PE model, therefore the final profiles of temperature along the cut−lines are plotted.

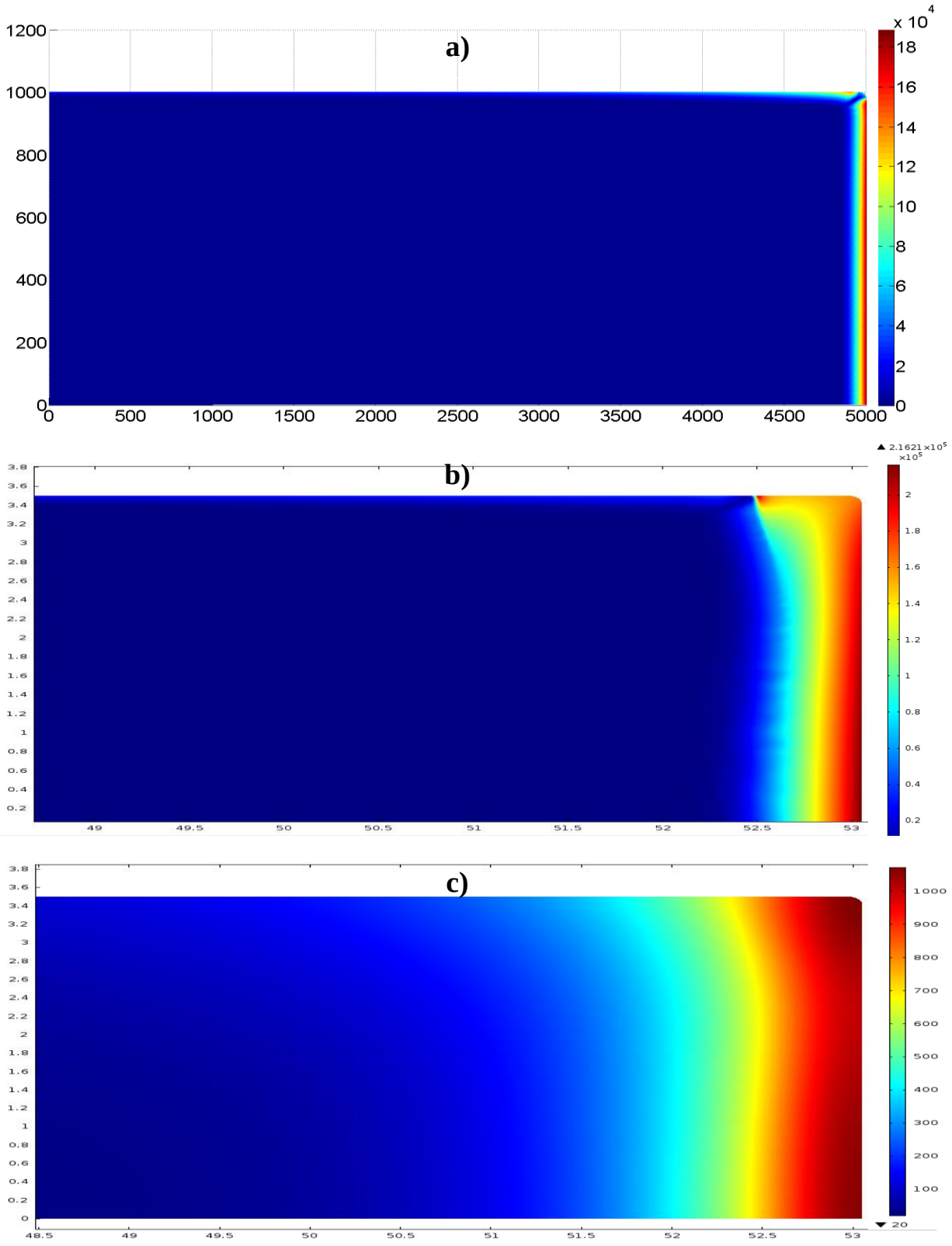

Figure 7.8 a) magnetic field at room temperature in a zoomed view of the disc. It measures 5x7 [mm] and is collected in a regular grid 5000*1000; **b)** magnetic field at the end of the process: there are the deformations induced by Curie's transition; **c)** Final temperature distribution n the time simulation: Curie's temperature corresponds to the yellow line in the colormap.

CUT−LINE in the MIDDLE of the disc.

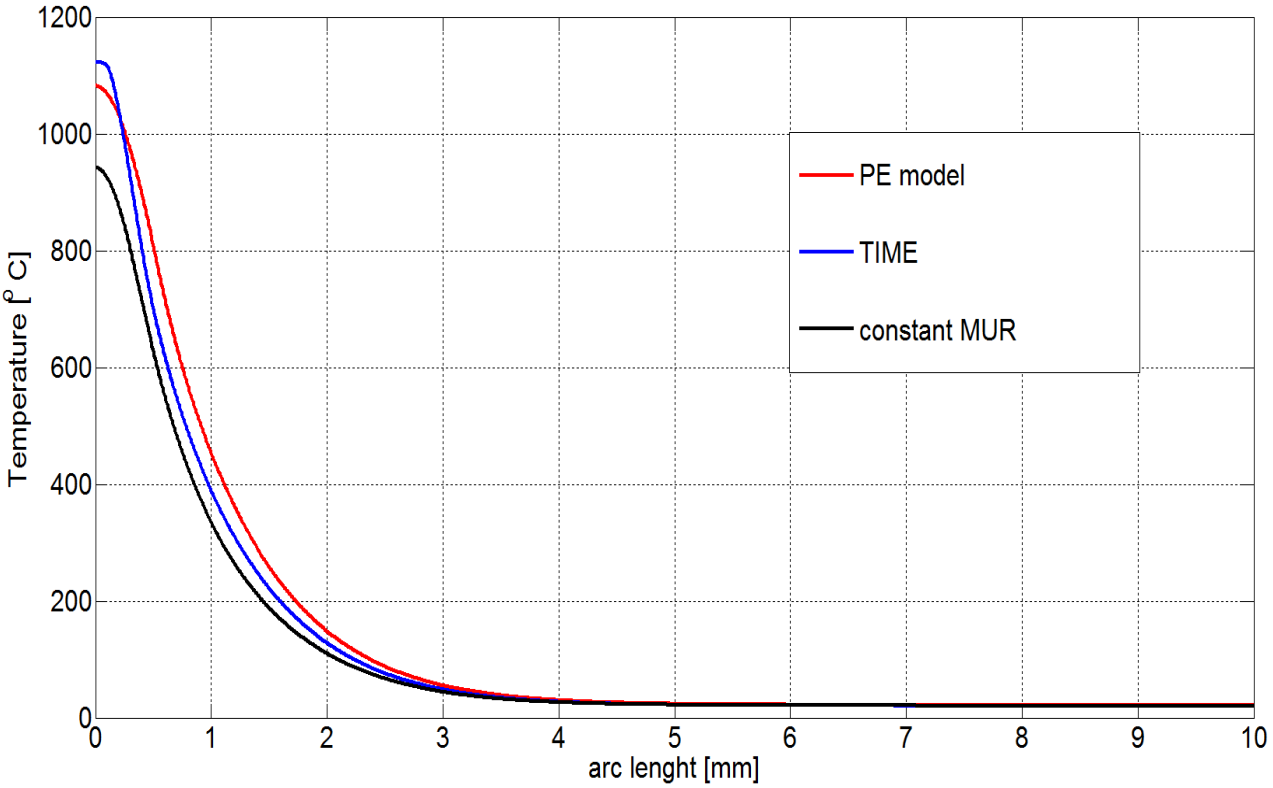

Figure 7.9 Distribution of the temperatures, at the end of the simulated induction heating process, along the cut−line in the **middle** of the disc.

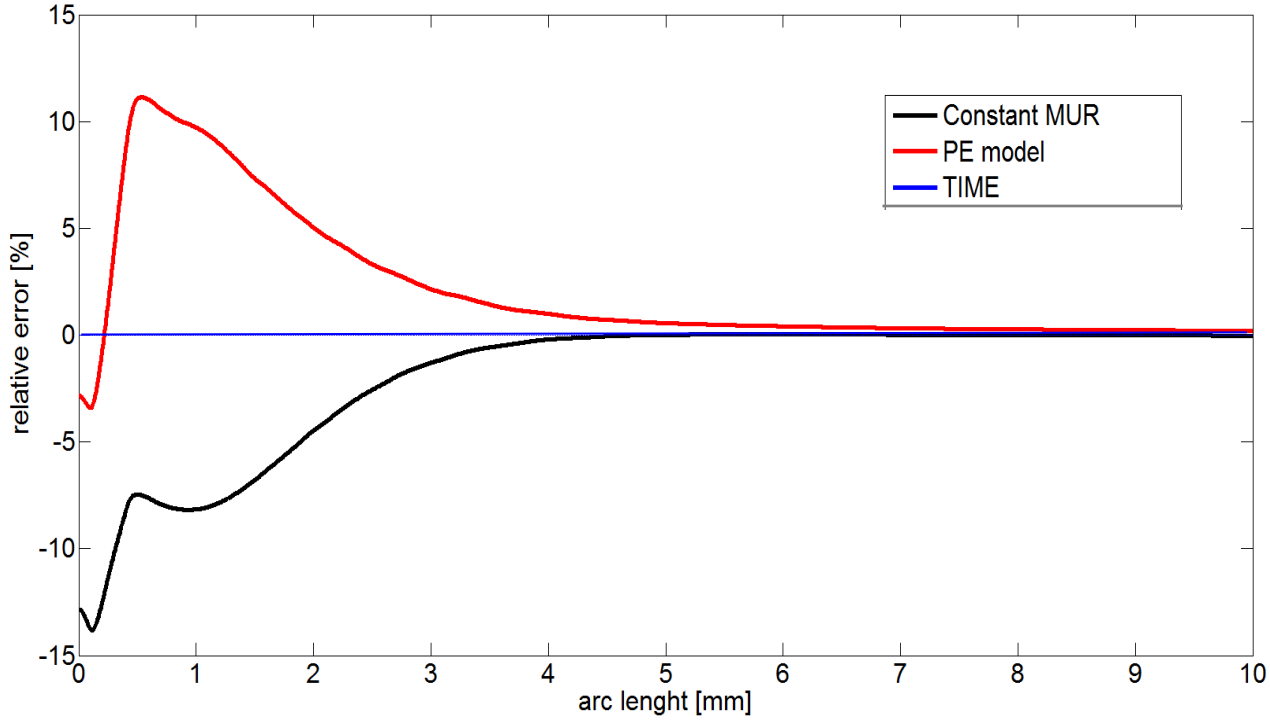

Figure 7.10 Relative error in % along the cut−line in the **middle** of the disc.

CUT−LINE on the SURFACE of the disc.

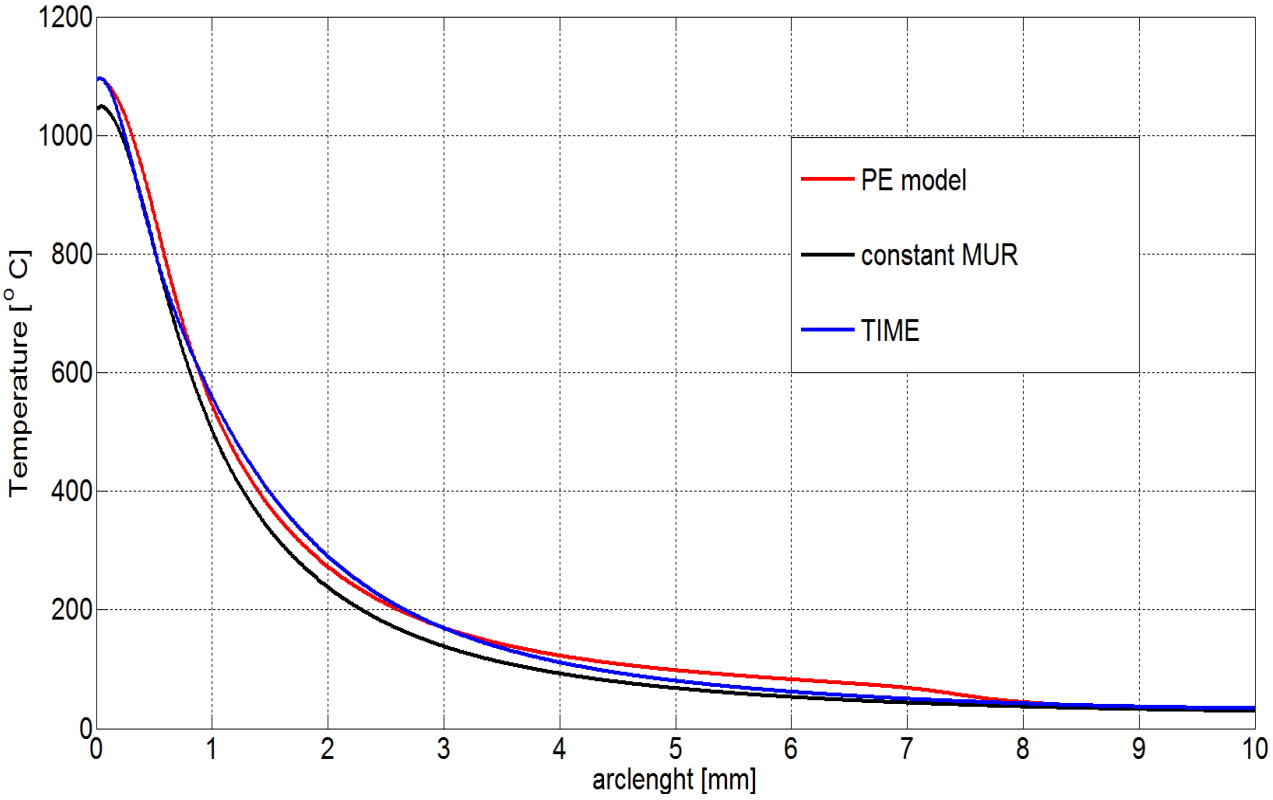

Figure 7.11 Distribution of the temperatures, at the end of the simulated induction heating process, along the cut−line on the **surface** of the disc.

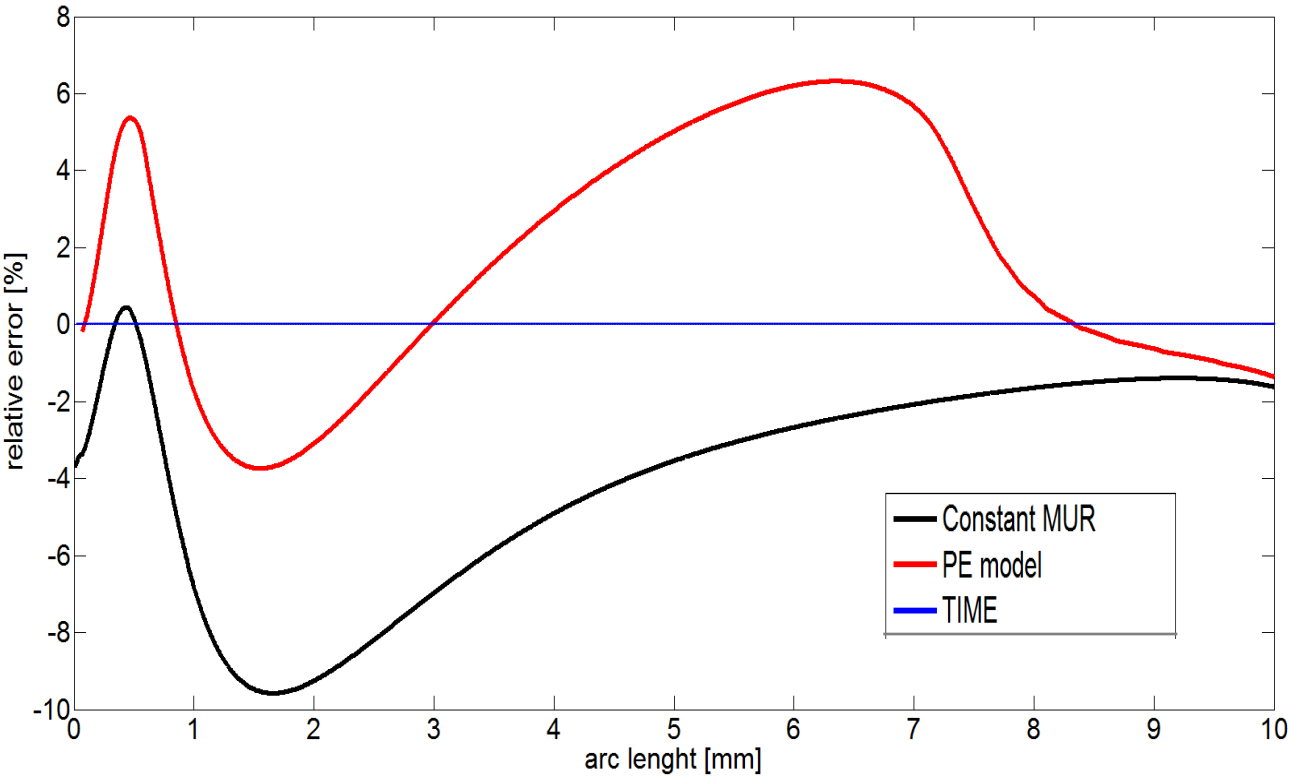

Figure 7.12 Relative error in % along the cut−line on the **surface** of the disc.

The *Figure 7.9* shows the final profile of temperatures along the surface of the disc. In order to put in evidence the most relevant region, the length of the cut–lines has been reduced to 10 [mm] of depth. Every colour in the plot corresponds to a different magnetic model utilized in the simulation. It is notable the huge excursion of temperatures that characterized induction hardening process: in 1 [mm] there is a gradient of more than five hundred degrees.
In the same page is present the figure of the relative error too. Along the length arc are plotted the relative errors of the models compared to the time domain simulation used as benchmark (that explains why the blue line of the time simulation is perfectly superimposed to the abscissa axis).
The images illustrate how the magnetic model with a constant magnetic permeability underestimates the losses along all the cut–line. The PE model underestimates the maximal temperature, but after 0.3 [mm] overestimates the final temperature.

In the *Figure 7.11* are plotted the temperature profiles along the surface cutline.
In this situation, the overall trend is difficult to track because the magnetic models oscillate around the reference time domain curve. It should be remarked that the PE model has almost the same final temperature, while the constant magnetic permeability uses to underestimate the reference temperature pattern.
These characteristics can be found easily in the relative error figures where the ***ratio*** (the dimensionless parameter introduced in the expression (6.1)), gives the following values:

–	Middle cutline	Surface cutline
constant **μ**	2.05%	3.98%
PE	2.21%	2.93%

Table 7.2 Values of the parameter "*ratio*".

However, this parameter is led astray because does not represents the real behaviour of the magnetic model. E.g. in the middle cut–line the magnetic model with a constant permeability has a better ratio then the PE model, but the PE model has a better the temperature on a thin layer of the sample.
In order to avoid many useless discussions on this thesis that does not provide conclusive evidences it is better to plot the 2Dplot of the absolute error.
The data are plotted in a regular grid of 5000x1000 points that included an area equal to the height of the disc for 10[mm] of depth.

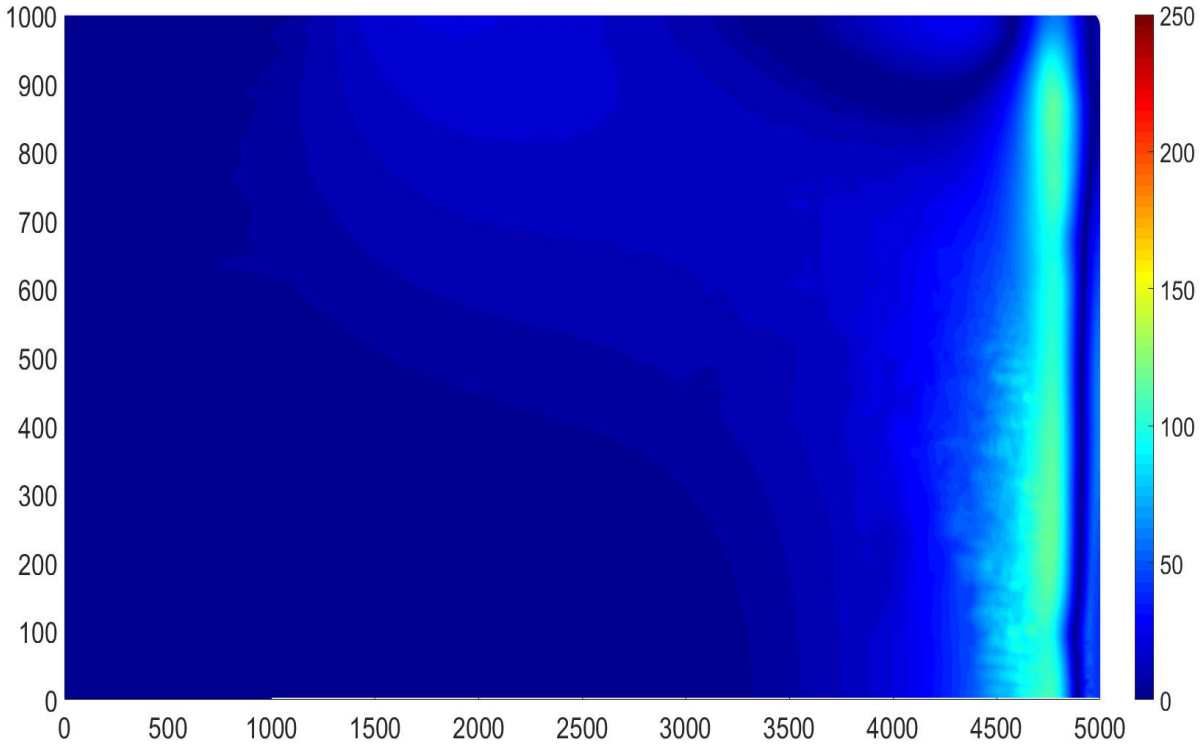

Figure 7.13 Absolute error of temperature [° C] between the reference and the **PE model**.

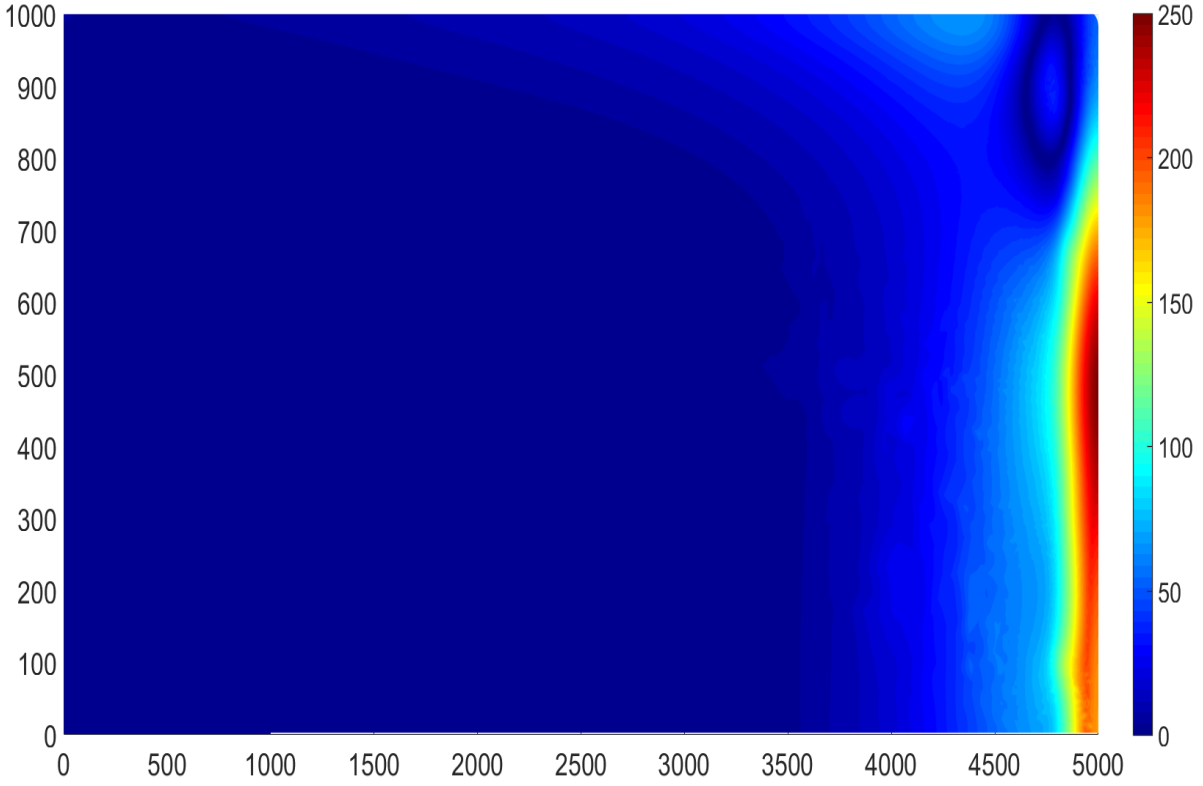

Figure 7.14 Absolute error of temperature [° C] between the reference and the **constant magnetic permeability** model.

For convenience, the final distribution of temperatures found in the reference time domain simulation are replotted here below.

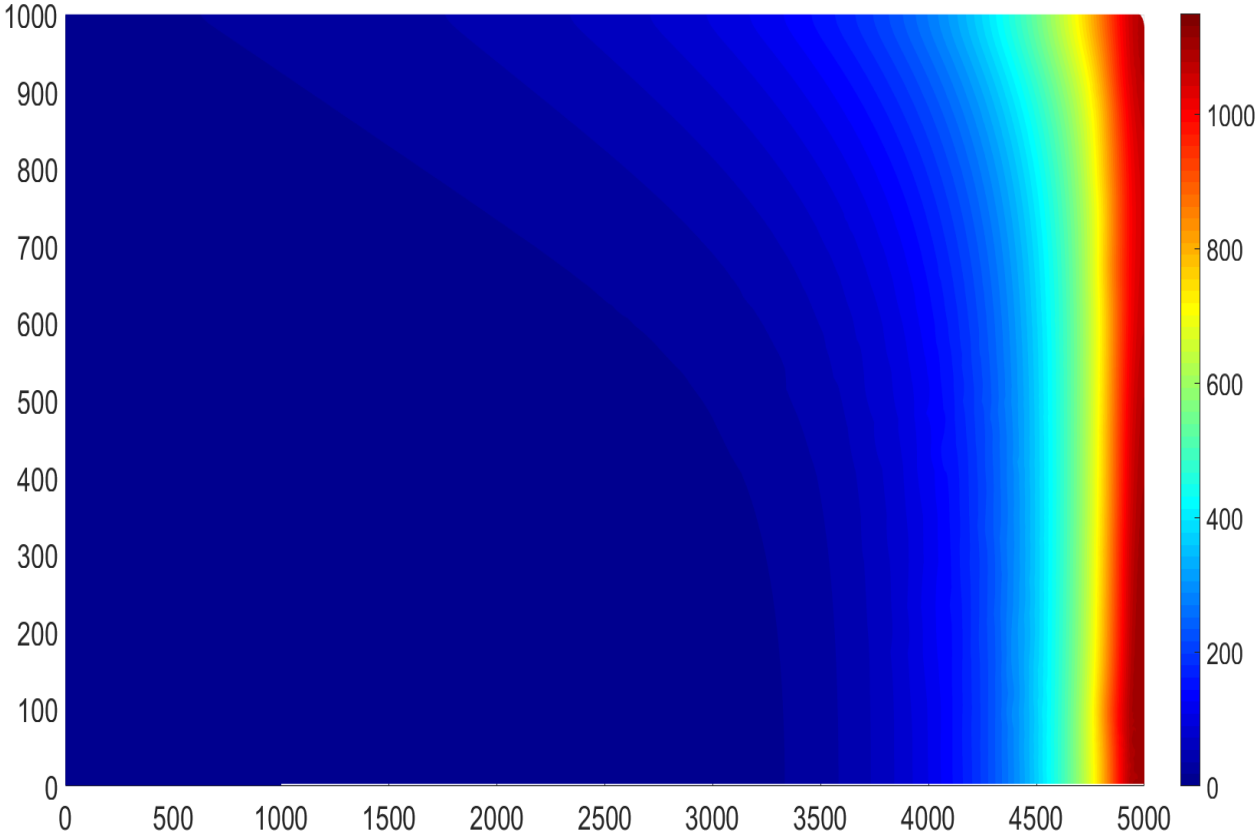

Figure 7.8 **c)** Final temperature distribution[° C] in the time simulation.

From the temperature distribution, it is notable that the temperature has a straight and uniform distribution on the eternal surface and drops down rapidly going close to the core of the disc. Near the corner there is a hotspot that modifies the distribution on the surface of the disc too. As previously mentioned this is due to the proximity effect with the inductor. The temperature distribution of the PE model and constant μ are not plotted because using the same temperature scale the differences of temperature cannot be easily recognized: the absolute error figures are more useful. The absolute error of the PE model is restrained and has a good approximation of the superficial temperature. The equivalent model overestimates the temperature in an inner region, that corresponds to the area where the induced magnetic field decreases, and drifts apart from the value used in the calibration problem. The absolute error of the second model shows a better approximation deep in the sample, however this is a region of relatively low interest, while on the external surface the error rises reaching unacceptable values. The constant magnetic permeability model underestimates the temperature profile of over two hundred degrees.

Chapter 8

Further Simulations

Starting from the simulations run and the results analysed until now, it is possible to study in detail some other aspects of the Power Equivalent model.
In particular, the analysis of the imaginary component of the magnetic permeability, neglected until now, are considered interesting. Moreover, the experimental data, collected by an induction hardened sample, are compared with the results of the PE model simulation. Lastly the new PE model is confronted with another model that proposes a different modification of the BHcurve to approximate the distribution of the power lost.

8.1 Hysteresis losses with the PE model

As mentioned in the chapter {3} the magnetic permeability is a complex physical characteristic. The imaginary component describes the hysteresis loop and the delay that the magnetization field has in correlation to the external and exciting magnetic field. Hence the imaginary magnetic permeability has negative amplitude.
As operated in the other chapters, the analysis starts from the 1D infinite slab geometry of the calibration problem. This is the simplest simulation to build in order to analyse the contribution of hysteresis losses.
The model is built starting from the experimental data of the hysteresis loop in steel AISI−4340. Then it is applied Fujiwara relaxation scheme combined with the time adaptive scheme in ***DarylMaxwell*** (*Polytechnique de Montréal* "homemade" software that uses an H−formulation). In this way, it is possible to follow the branches of the loop and calculate, through the formulation expressed in the Chapter {4}, the equivalent magnetic permeability in function of the magnetic field and consequently the equivalent model.
In the figure below are plotted the hysteresis loop and the real and imaginary components of the equivalent BHcurve adopted by the PE model.
The image is centred on the first quadrant of the Cartesian plane of *Figure 3.9* : that is the reason why the black lines of the magnetization curve, that describes the hysteresis loop, are only partial.
It is possible to notice that the imaginary part has a low value and asymptotically tends to zero. As a matter of fact, the branches of the loop are detached for small value of magnetic field and for high saturation level they usually are almost superimposed.

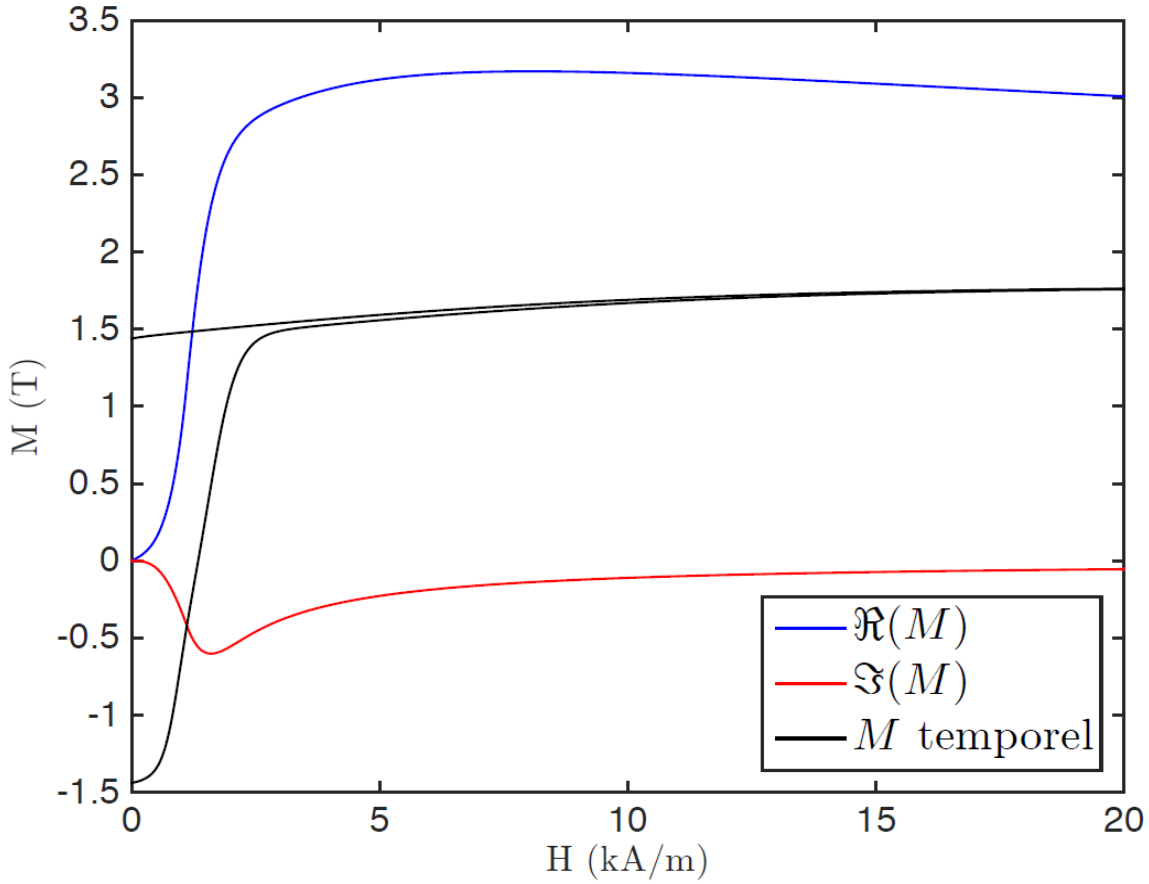

Figure 8.1 First quadrant of the Cartesian plane where is plotted in black the hysteresis loop described by the experimental data in function of time. Then are plotted the real and imaginary components of the equivalent BHcurves for the PE model.

Successively is compared specific absorption rate of eddy currents losses with the hysteresis one. Essentially is run the time domain simulation with the complex magnetic permeability to see the contribution due to hysteresis losses.
As mentioned before, it is used the geometry of the calibration problem presented in the Chapter {5} with the parameters described in the *Table 5.1.* The frequency of the magnetic field is raised up to 190 [kHz] to analyse the specific case of induction hardening process. The deformations of hysteresis losses are neglected, so the experimental data collected in a quasi−static condition are considered valid in this range.
The losses are plotted in function of the space along the infinite slab: to evidence the behaviour of the phenomenon the length is limited to 0.25 [mm].

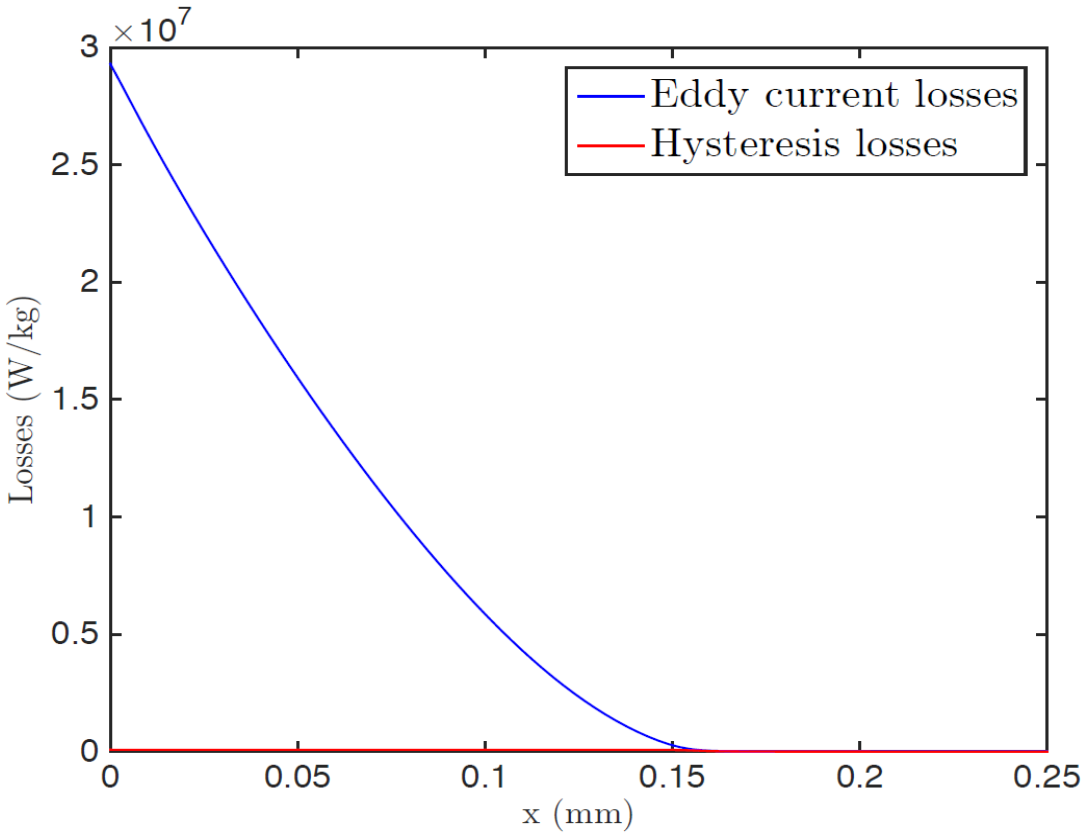

Figure 8.2 Specific absorption rate [W/kg] of eddy current and hysteresis in the 1D calibration problem simulated in a time dependent domain.

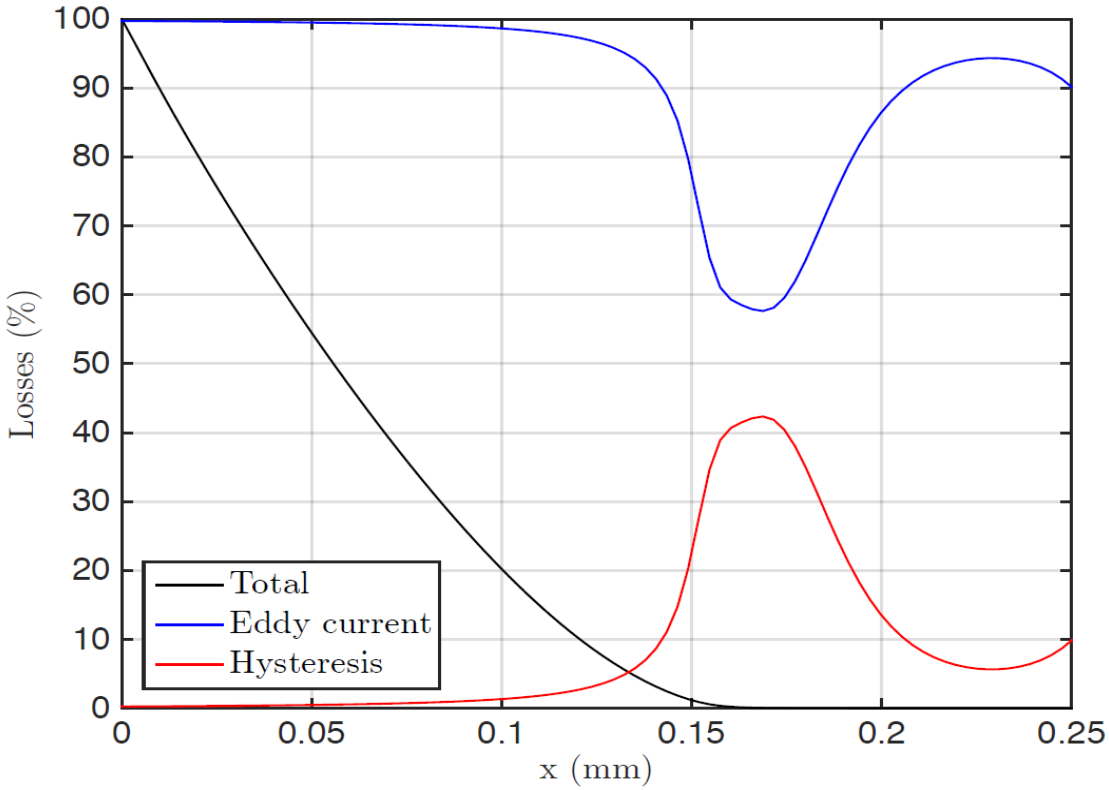

Figure 8.3 Relative contribution of eddy current and hysteresis losses in the 1D calibration problem.

As emerges from the *Figure 8.2* and *8.3*, the contribution of hysteresis losses is completely negligible. On the first image emerges that the hysteresis losses are several orders of magnitude lower than eddy current losses. In the practical aspect of surface induction hardening they do not improve the accuracy of the model.
In the image where are plotted the relative contributions appears that the hysteresis losses have a weight of the 40% only when is considered a deep portion of the sample. Here the eddy current losses are dropping down to a null value, but the low magnetic field induced in the sample is enough to generate a hysteresis in the medium.
These results find a reproof in literature because, according to Steinmetz's equation, the eddy current losses are proportional to the square of the frequency while hysteresis losses are directly proportional to frequency. Therefore, in the range of frequency examined hysteresis can be omitted.

Nevertheless, it is important to underline the potential of this Power Equivalent model because it can consider hysteresis losses in a frequency domain simulation.
This aspect, useless in induction hardening, might obtain a remarkable relevance in the study of core heating (where the frequency is in the range of mains frequency ~50−60 [Hz]). Moreover, the study of hysteresis is preponderant in other electrical subjects: principally in the characterization of magnetic sheet steel, where the chemical composition, and the reduced dimension prevents eddy currents flowing.

8.2 Comparison with experimental results

Verified that the hysteresis losses can be neglected and confirmed the accuracy of the new PE model, a mandatory comparison is between experimental results and a simulated process.
In this paragraph, the experimental high−speed measurement of surface temperature is compared to the simulated process of induction hardening. It is realized using the data collected at **ÈTS** concerning an induction heating process realized with power control. The process of quenching is not simulated and compared with experimental data, not only because the acquisition of accurate data is not easy during this stage of the treatment, but also because the aim of the thesis is related to the validation of new PE model that is based on the electromagnetic simulation (quenching simulation concerns only thermal simulation).

The model built, is almost equivalent to the numerical simulation introduced in the chapter {7}. As a matter of fact, not only the geometry of the steel AISI−4340 disc is the same, but also the thermal and electrical properties are identic. In addition, the mesh structure, and the multiphysics coupling are similar (this is the reason why neither a table or a figure is reported: the last chapter is taken as benchmark).

The main differences of this comparison with experimental data is related to the control of the inductor. In this case, the active power flowing in the coil must be restrained to such a small range that can be assumed constant during the whole duration of the treatment. The final time of the heating process is 0,5 [s]: five time longer than the current control simulation.

Parameter	Value	Unit
Time	Range(0, 0.1)	[s]
Power (user interface)	90	[kW]
Simulation Power	50.8 hypothized η =56,7%	[kW]
Frequency	190	[kHz]

Table 8.1 Parameters of the power control simulation of induction heating

The power control of the inductor is realized through the coupling between COMSOL with MATLAB. When the electromagnetic simulation is solved, the active power's surface average is sampled in the coil. Then, it is integrated along the total length of the inductor to obtain the value of power flowing in the terminals. Successively, it is imported in MATLAB and thanks to a regulation code is verified that it falls back into the range of P_{target}±0.5%. Consecutively, the root mean square of the required current is obtained and this value will be used as input data in the following electromagnetic simulation. Because the electromagnetic simulation has a restrained computational time (thanks to the PE model in harmonic domain), this process is iterated until convergence. When are found the correct values of power and current, the process proceeds with the coupled thermal simulation. This method is efficient because, combined with the code for the maximal temperature jump, subdivides the process in tiny time steps so it is required at maximum one iteration to find acceptable values.

Moreover, in order to achieve the best accuracy possible another modification is introduced: the PE model is built using the normalized magnetization curve from the experimental data collected at *Polytechnique de Montréal*. This curve refers to expression (3.10) and *Figure 3.13*.

The following results are obtained from the calibration problem of chapter {5} with an amplitude of the applied magnetic field equal to 200[kA/m].

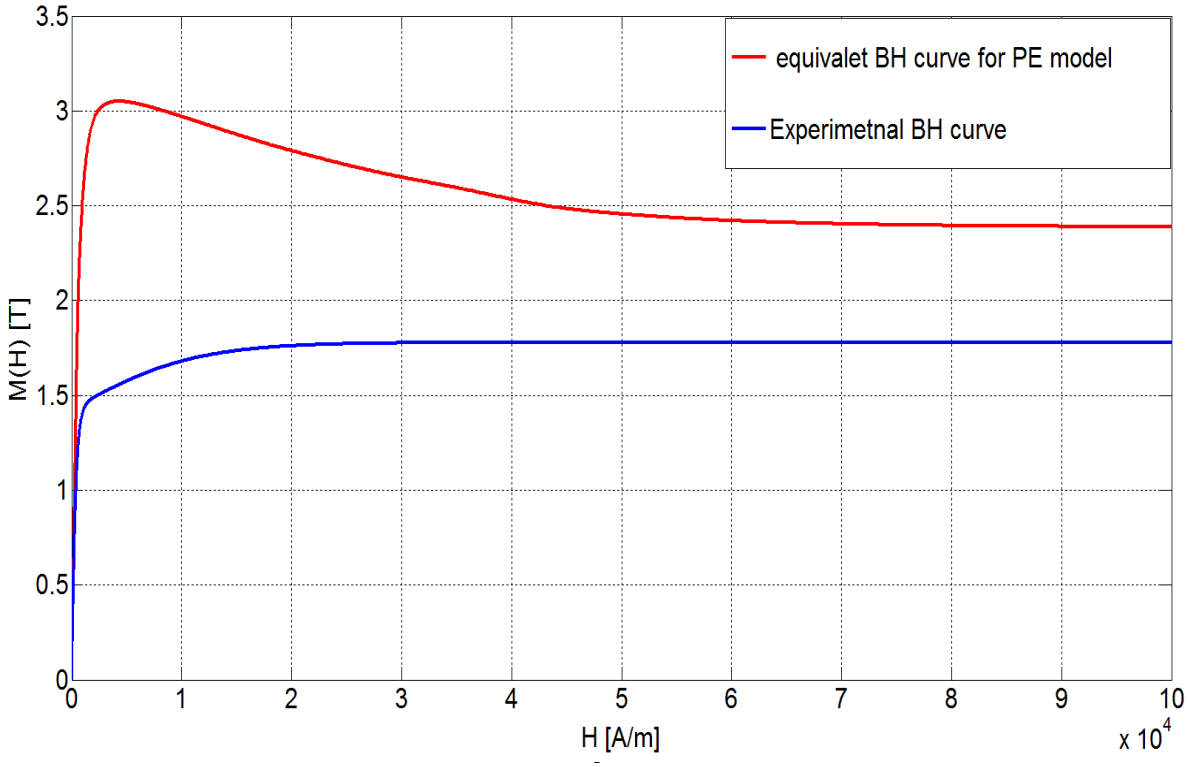

Figure 8.4 PE equivalent BHcurve (red line) built from experimental magnetization curve (blue curve), using the calibration problem with H_0 =200 [kA/m].

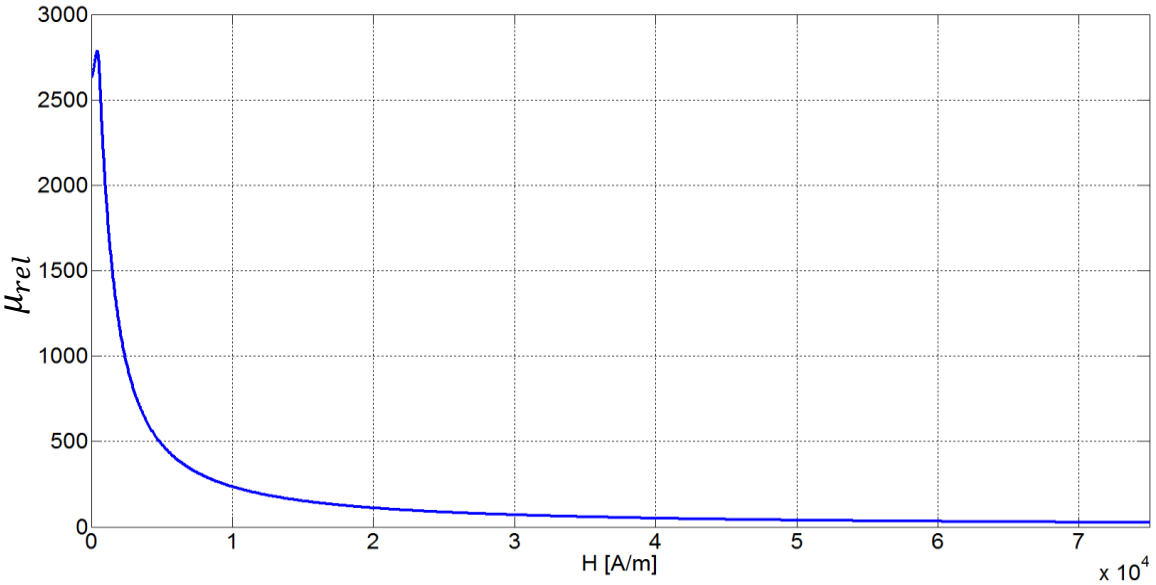

Figure 8.5 Relative magnetic permeability of experimental data plotted in function of the applied magnetic field H [A/m].

The contactless, optical method of high-speed imaging system evaluates specific superficial isotherms as temperature rises. Therefore, in the figure below is

presented the comparison of isotherm profiles. Every temperature is indicated with a colour: the experimental data tracks a continuous line while the simulated values are plotted in a dashed−line.
It is possible to see that the simulated data provides inconclusive data regarding the time evolution of temperatures. The simulation overestimates the power lost and consequently it anticipates the time while the curves raise.
The disappointing discrepancy can find an explanation in the wrong selection of some parameters. Probably indeed, the hypothesized efficiency of the power supply for the induction hardening machine is incorrect, or even more, there is a deeper problem in the nature of power control simulation. As a matter of fact, to operate a constant power control process, it is mandatory to change the value of the currents. The transition from ferromagnetic into paramagnetic medium, alters the equivalent reluctance seen from the terminals of the coil and consequently the reactive and apparent power absorbed.
The modifications in function of time of the current are directly proportional to the modifications of the applied magnetic field. Therefore, for every time step a new calibration problem should have been run.

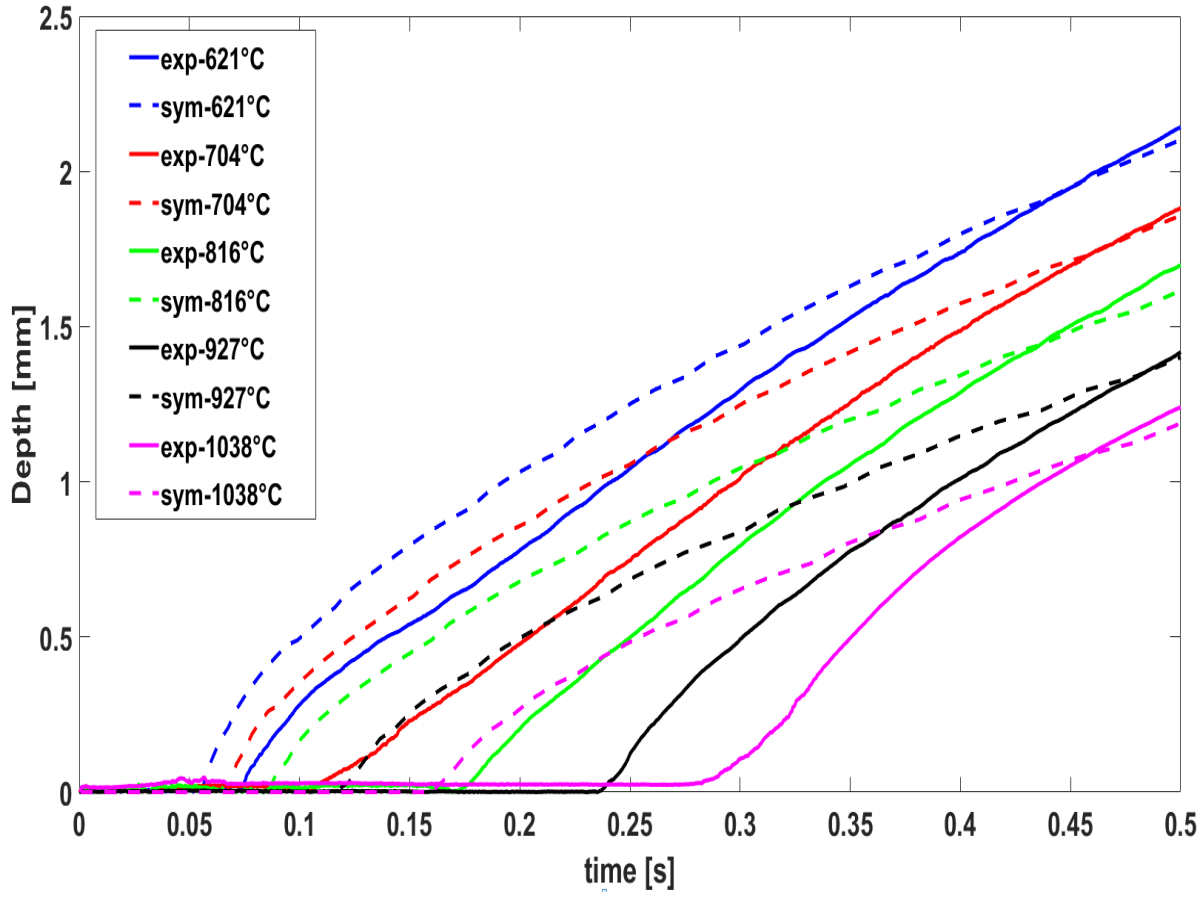

Figure 8.6 Evolution of the isotherms obtained by simulation and experiment in the upper surface of steel disc.

As the previous simulation in induction heating, it must be take into account the fact that the distribution of magnetic field is spatially dependent because of the non-uniform distribution of temperatures.
Moreover, the PE model is built from the mono-dimensional diffusion equation, so it might not consider properly the rotational behaviour of magnetic fields.

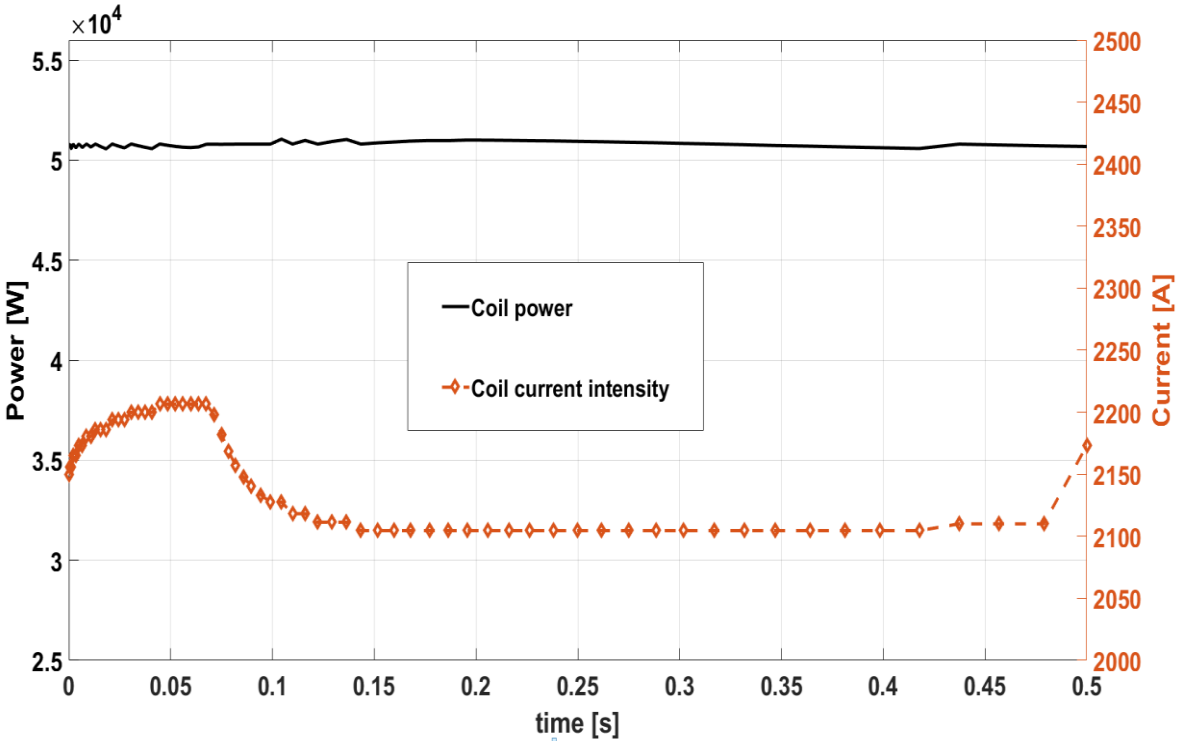

Figure 8.7 Evolution in time of apparent power and current, both in function of time. While the power in constant, the currents changes evidently.

8.3 Enhanced Coenergy model

In the last paragraph of this thesis, it is analysed the comparison of the new PE model with other equivalent model that approximates the non-linear behaviour of steel with an equivalent curve to use in frequency domain simulations. One of the most interesting model uses the *Enhanced Coenergy*.
The concept of coenergy is widely used to transform the nonlinear anhysteretic curve into an equivalent permeability $\mu_{eq}(H)$ that is compatible with harmonic domain simulations. However, the coenergy, which represents the area under a given B-H path, and which has units of energy [J], is not a meaningful physical quantity. Despite that, it has been shown that certain simulation models based on coenergy lead to a reasonably good estimation of the losses.
In the time domain, there are many different definitions of the coenergy leading to

different equivalent magnetic permeabilities. These definitions are summarized in *Table 8.2* and illustrated in *Figure 8.8*.
It is relevant to highlight the distinction between the anhysteretic curve (normalized magnetization curve) and the curve of first magnetization, i.e. the path followed when starting the magnetization process from a completely demagnetized state.

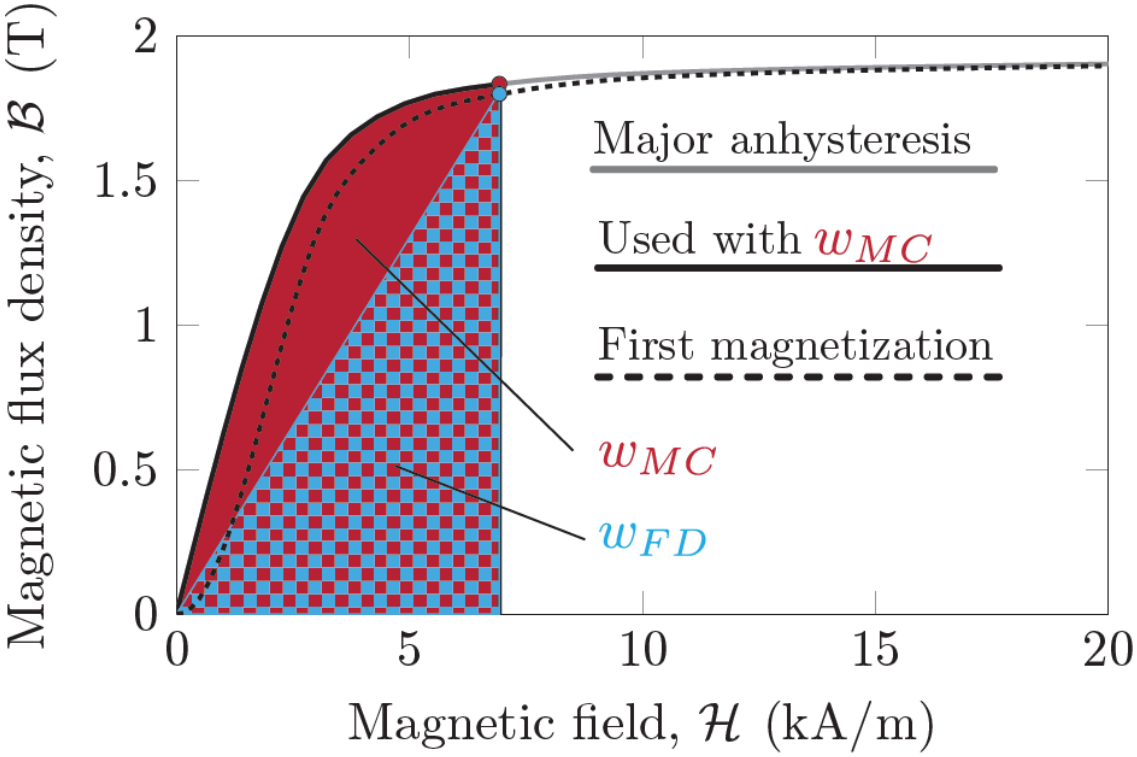

Figure 8.8 Reference normalized magnetization curve with two coenergy definitions.

Model	Symbol	Definition
Flux density coenergy	$W_{FD}(\mathrm{H})$	$\frac{\boldsymbol{B(H)} * \boldsymbol{H}}{\mathbf{2}}$
Magnetic coenergy	$W_{MC}(\mathrm{H})$	$\int_0^{\boldsymbol{H}} \boldsymbol{B(H)dH}$
Enhanced coenergy	$W_{EC}(\mathrm{H})$	$\frac{\boldsymbol{W_{FD}}(\mathbf{H}) + \boldsymbol{W_{MC}}(\mathbf{H})}{\mathbf{2}}$

Table 8.2 Definitions of the coenergy models.

The process that has been simulated is the same of chapter {7}: induction heating of a steel AISI−4340 disc, in a current control process. The geometry, mesh structure, material properties and the coupling between thermal and electromagnetic are not reported here. For every reference, the last chapter can be consulted as benchmark.

To compare the equivalent models, the modified BHcurves are plotted in *Figure 8.9;* to build the PE model, the analytic expression (3.5) was used in the calibration problem with an applied field of 200 [kA/m].
In the image, it is possible to see the blue line that describes the anhysteretic curve of reference in the time domain simulation, with a light blue area calculated to define the coenergy. At second instance, there is the red curve of the PE model with the peak for low magnetic fields and finally the green line for the enhanced coenergy.

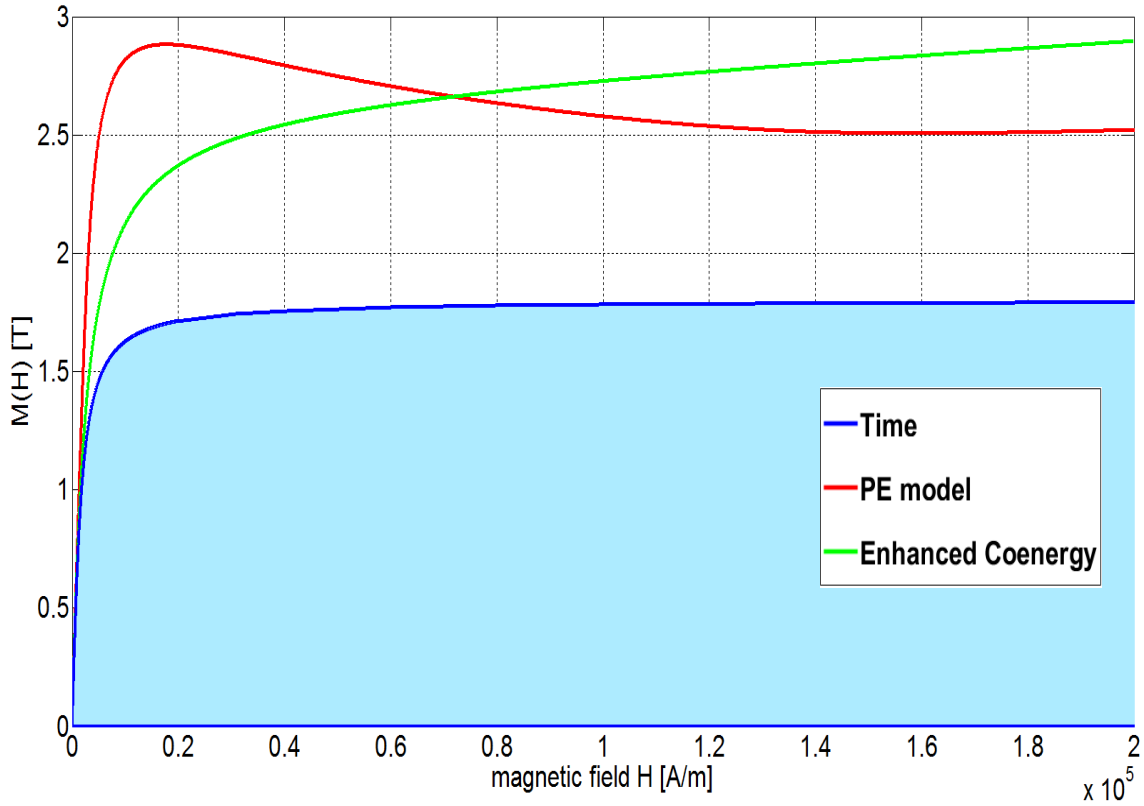

Figure 8.9 Normalized magnetization curve in the time domain, with the equivalent BHcurve given by the PE model and the Enhanced Coenergy.

To compare the results, the final profiles of temperature are plotted along the two cut-lines that characterized the disc geometry. The first one is on the top surface of the disc, while the second one is in the middle of the sample (i.e. on the bottom surface of the simulated geometry).
In the middle cutline the profile of the enhanced coenergy has the same maximal temperature of the PE model, but it overestimates the losses moving towards the centre of the disc. The discrepancy in this portion becomes unacceptable.
On the surface of the disc the approximation of the equivalent models improves because all the models have the same trend compared with the time domain results. However, the maximal temperature on the edge of the corner is lower for the enhanced coenergy.

Results on the cut−line in the **middle** of the steel disc.

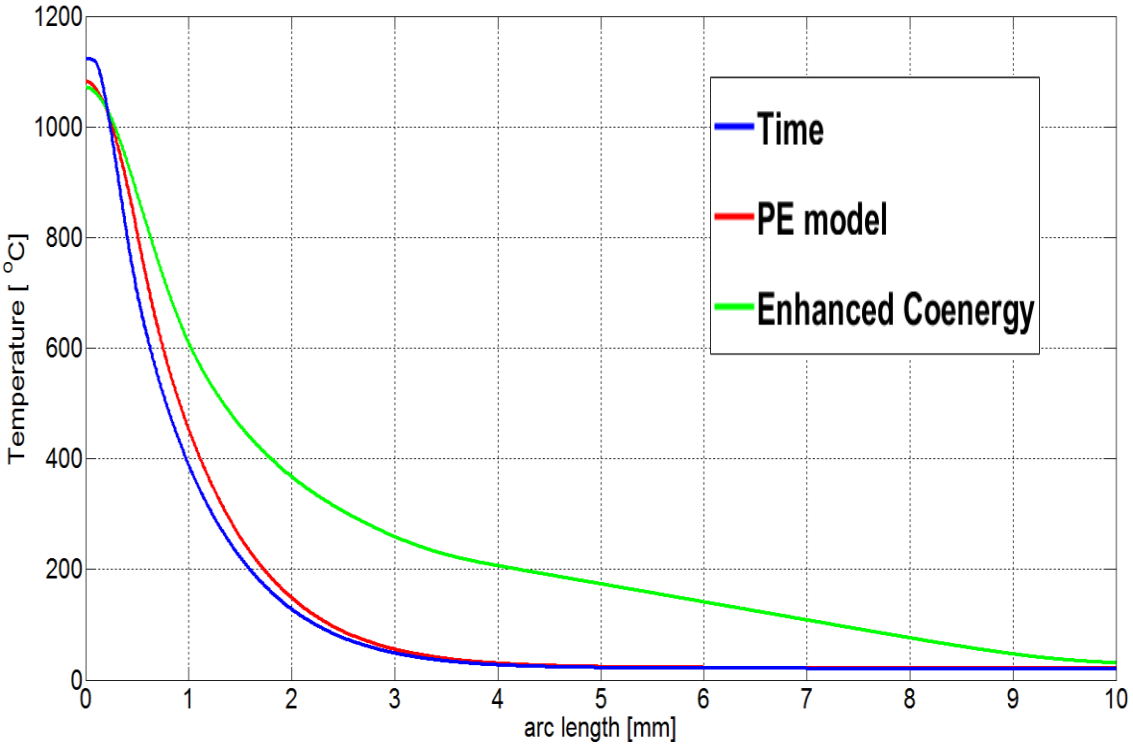

Figure 8.10 Final profiles of temperatures in the **middle** cut−line.

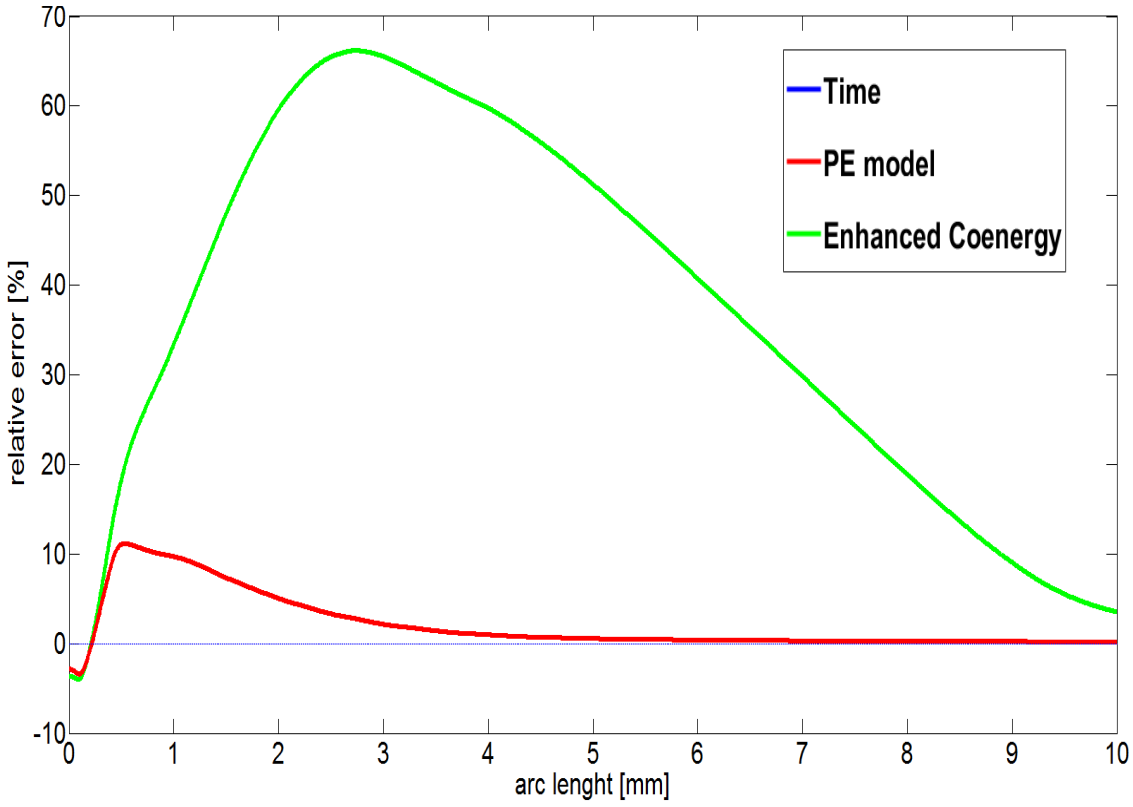

Figure 8.11 Relative error of equivalent models in the **middle** cut−line.

Results on the cut−line on the **surface** of the steel disc.

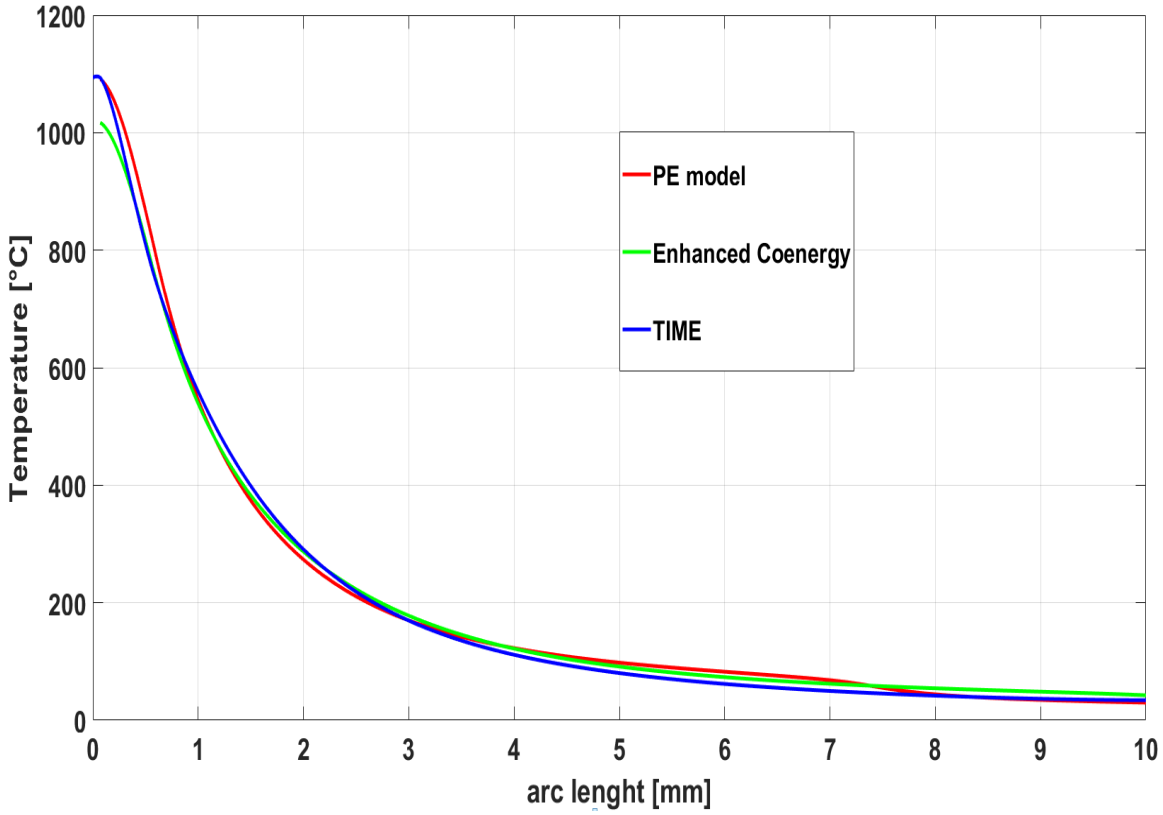

Figure 8.12 Final profiles of temperatures on the **surface** cut−line.

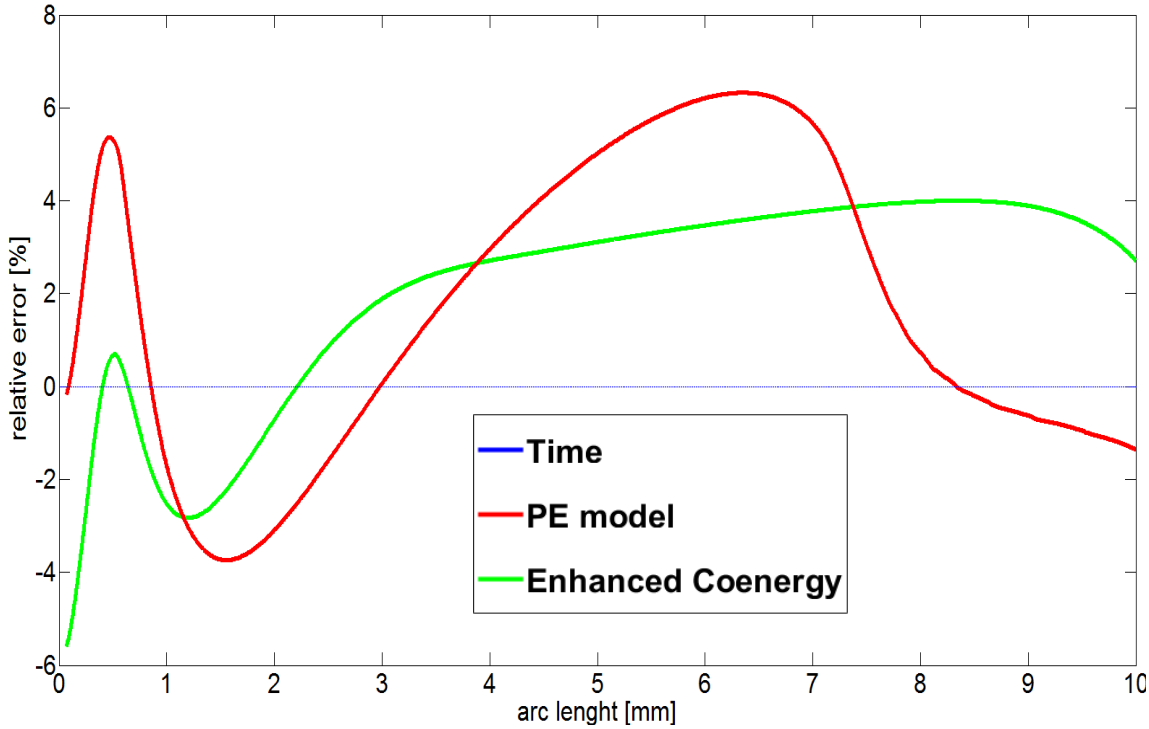

Figure 8.13 Relative error of equivalent models on the **surface** cut−line.

The values of the parameter *ratio* are given according to the expression (6.1), As it is expected, the value of the enhanced coenergy reached the highest level in the middle cut−line. A more exhaustive description of the equivalent model can be provided by a 2D plot of the absolute error of temperature between the final distribution in time domain simulation and enhanced coenergy.

Model	Middle cutline	Surface cutline
Enhanced Coenergy	37.19%	2.82%
Power Equivalent	2.21%	2.93%

Table 8.2 Comparison of the "*ratio*" parameter.

The final distribution of temperatures and the absolute error are plotted in a regular grid of 5000x1000 points. As the *Figure 8.14* evidences, there is a slight error on the thin layer close to the external surface and the corner. However, inside the sample the error remarkably raises and reaches a difference of more than 200 degrees in portions of the disc that are still sensible for the hardening process.
A reason of this behaviour might be found in the approximation of the equivalent curve. In fact, for strong saturation (i.e. high value of magnetic field) the equivalent BHcurve gradually grows because of the contribution of the coenergy.

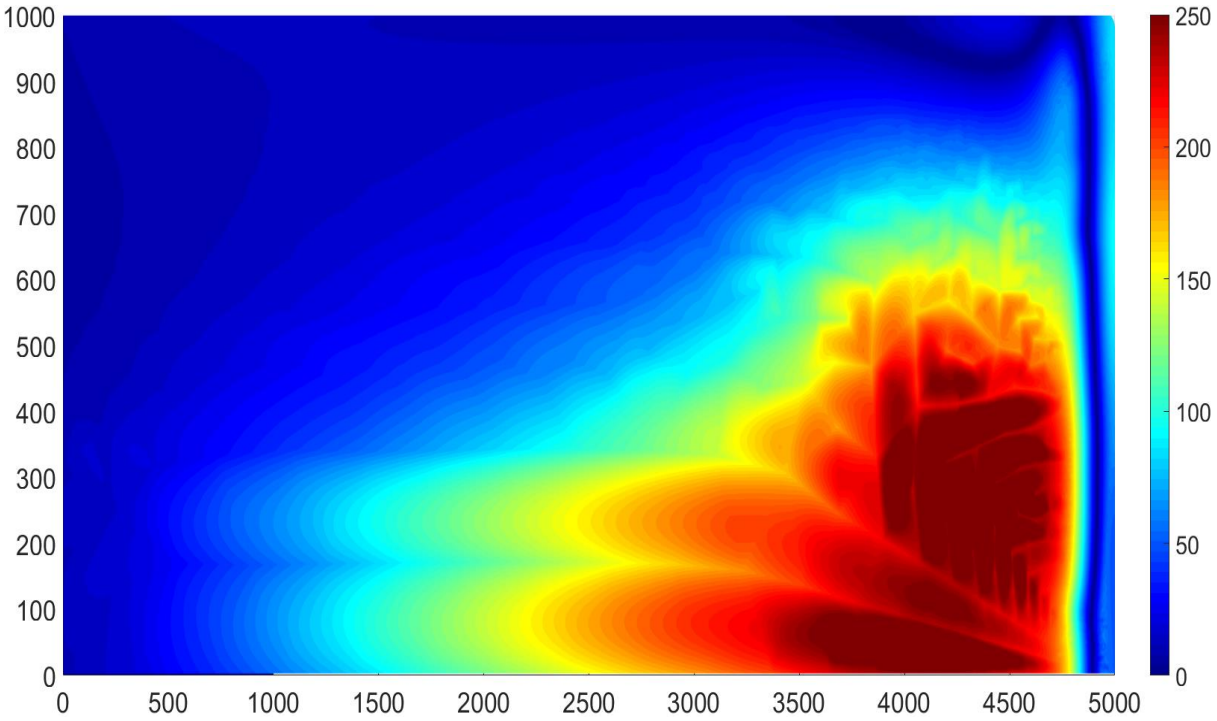

Figure 8.14 Absolute error of temperature [°C] between the time reference and the Enhanced Coenergy model.

In conclusion, the PE model can be preferred to the Enhanced Coenergy, because it provides the best approximation of electromagnetic losses.
Moreover, thanks to his minimal computational cost, it can be utilized in 3D simulation characterized by complex geometry. In the *Figure 8.15* is plotted the specific power lost for eddy currents in a quarter of gear's tooth, to provide a qualitative idea of the potential of this model (further comparisons are not yet analysed in 3D geometries). Even if the PE model is tied to the calibration problem and the simplifications made in the mono-dimensional space, it has a reasonable potential.

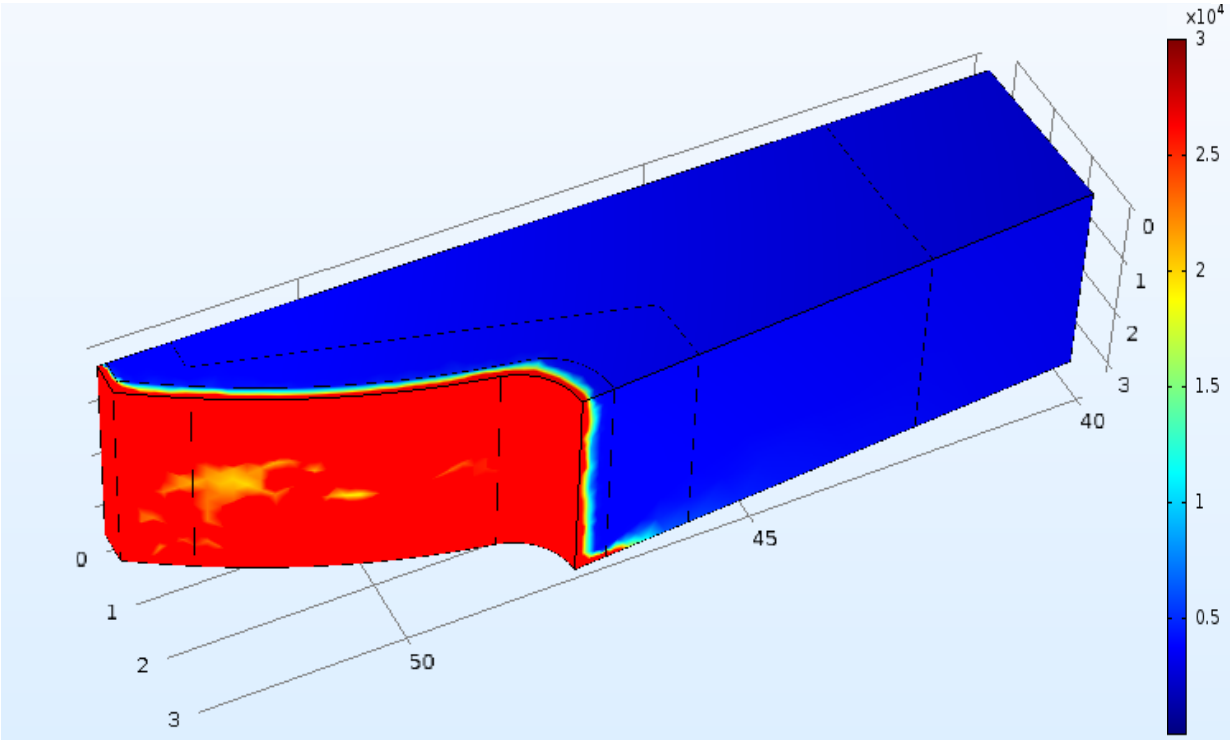

Figure 8.15 Specific losses [W/m^3] in a portion of a tooth of a gear in a process of surface induction heating.

References

[1] Bocher Philippe, Mingardi D., Larregain B., Bridier F., Dughiero F., Spezzapria M., "Simulation of fast induction surface heating and comparison with experimental full-field surface temeprature measurements"; HES-13 *Heating by Electromagnetic Sources, Università degli Studi di Padova (2013)*

[2] Candeo Alessandro, Ducassy Christophe, Bocher Philippe, Dughiero Fabrizio; "Multiphysics Modeling of Induction Hardening of Ring Gears for the Aerospace Industry"; IEEE *Transactions on Magnetics (May 2011)*

[3] Candeo Alessandro,Bariani P., Martinelli G., Dughiero F., "Induction hardening of components for the aerospace industry"; *PhD Thesis, Università degli studi di Padova (2012)*

[4] Ciccarone Lorenzo, "Models and tests of induction contour hardening process"; *Master thesis, Università degli Studi di Padova (2014)*

[5] Ducassy Christophe, " Prédiction de la dureté et de la profonderu de la zone de surrevenu lors d'une chauffe rapide par induction d'un acier 4340 temprè revenue"; *Master Thesis, École de Technologie Supérieure (2010)*

[6] Gür Cemil Hakan, Pan Jiansheng, "Handbook of Thermal process modelling of steels"; *IFTSE, CRC Press (2009)*

[7] Jin Jianming, "The finite element method in electromagnetics"; *Wiley&Sons (1993)*

[8] Lupi Sergio, "Appunti di Elettrotermia"; *Università degli studi di Padova (2005)*

[9] Lupi Sergio,Dughiero Fabrizio, Forzan Michele," Modelling Single and Double- Frequency Induction Hardening of Gear-Wheels"; *The 5th International Symposium on Electromagnetic Processing of Materials (2006)*

[10] Lupi Sergio,Forzan Michele, Aliferov Aleksandr, " Induction and Direct Resistance Heating, theory and numerical modeling", *Springer (2015)*

[11] Marconi Antonio, "FE analysis in time domain of Simultaneous Double Frequency induction hardening"; *Master Thesis, Università degli Studi di Padova (2015)*

[12] Metaxas A.C., "Foundations of Electroheat: a Unified Approach"; *University of Cambridge, Wiley &Sons (1996)*

[13] McMeekin Kevin, Sirois Frédéric, Tousignant Maxime*; "*Improving the accuracy of time-harmonic FE simulations in induction heating applications Towards better ferromagnetic material models"*; The international journal for computation and mathematics in electrical and electronic engineering Vol. 36 No. 2, (2017 pp. 526-534)*

[14] Rudnev V, Loveless D., Cook C., Black M., " Handbook of induction Heating"; *Marcel Dekker, New York (2003)*

[15] Senhaji Achraf, Larregain Benjamin, Vanderesse Nicolas, Bocher Philippe; "Temperature history Modelling and Validation of fast induction hardening process"; *HES-16 Heating by Electromagnetic Sources, Università degli Studi di Padova (2016)*

[16] Spezzapria M., "simulazione numerica del processo di tempra ad induzione di ruote dentate per l'industria areonautica"; *Master thesis, Università degli Studi di Padova (2011)*

[17] Totten George E.,"Steel Heat Treatment: metallurgy and technologies"; *Taylor & Francis (2006)*

[18] Vanderesse Nicolas, B. Larregain, F. Bridier, Bocher Philippe; "High-speed surface temperature measurement using heat-sensitive lacquers applied to induction heating"; *LOPFA, Department of Mechanical Engineering, ETS (2016)*

[19] ASM Handbook. 2000. Heat Treating. Volume 4

Ringraziamenti

Ai miei genitori, che sostenendomi sempre ed incoraggiandomi in tutte le decisioni prese, hanno reso possibile questo percorso.

A tutta la mia famiglia e alle persone che di fatto sono diventate membri di essa, un ringraziamento per essere stati punti di riferimento e fonte d'ispirazione.

Ai miei amici Marco, Carlo ed Erik: fedeli compagni d'avventura da una vita.

A tutti gli amici che hanno saputo regalarmi un sorriso ed un briciolo della loro attenzione, con i quali sono cresciuto ed ho fatto strada insieme.

A Michele, Fabio e Matteo perché più che compagni di studi, sono stati amici sinceri e confidenti leali con cui affrontare le difficoltà della vita universitaria.

A tutti le persone che hanno reso indimenticabile il mio soggiorno a Montréal: senza la loro compagnia ed allegria sarebbe stato molto più arduo superare il freddo inverno canadese.

A tutti i professori e colleghi che mi hanno seguito in questi anni e mi hanno trasmesso l'amore per l'ingegneria; un grazie particolare al professor Bocher per avermi seguito e stimolato a superare i miei limiti.

Infine, esprimo la mia gratitudine all'intera comunità del Collegio Gregorianum per avermi accolto ed accompagnato nella mia vita accademica diventando così la mia famiglia patavina.

Queste poche righe ricambiano solo parzialmente la profonda riconoscenza che provo verso tutte le persone che mi sono state vicine, anche solo per un breve momento.

Condividere con loro pensieri, sentimenti ed emozioni mi ha reso la persona che sono, ma soprattutto mi ha donato, nell'arco della vita, una continua gioia.